The Influence of Ozone Changes on the Stratospheric Dynamics in 4xCO_2 Climate Simulations

Master's Thesis
at the Faculty of Physics,
Ludwig-Maximilians-University Munich

Leonhard Hufnagl

March 3rd 2022

Examiner
Prof. Dr. Hella Garny

Supervisor
Prof. Dr. Hella Garny
Dr. Roland Eichinger

Der Einfluss von Ozonänderungen auf die stratosphärische Dynamik in 4xCO_2-Klimasimulationen

Masterarbeit
an der Fakultät für Physik,
Ludwig-Maximilians-Universität München

Leonhard Hufnagl

3. März 2022

Prüfer
Prof. Dr. Hella Garny

Betreuer
Prof. Dr. Hella Garny
Dr. Roland Eichinger

Abstract

Ozone modifies the temperature in the stratosphere and thus it is important to quantify the climate impacts exerted by stratospheric ozone in climate models. This could yield new insights into the role of the ozone layer in the climate system. An increase in the CO_2 concentrations in this system changes the temperatures and dynamics of the troposphere and stratosphere and thereby also the ozone concentrations. Since ozone absorbs longwave and shortwave radiation, the altered ozone distribution, in turn, affects temperatures and thus also modifies the CO_2-induced changes in stratospheric dynamics. The stratospheric dynamics influence the transport of trace gases like ozone and water vapor and can also impact the tropospheric dynamics. This motivates to study these in detail. Therefore, model simulations were performed using a climate-chemistry model in which CO_2 concentrations were quadrupled compared to pre-industrial times. For the $4xCO_2$ simulation, this was done once by prescribing an unchanged (pre-industrial) ozone distribution and once a changed ozone distribution from a previous $4xCO_2$ simulation. The change in ozone leads to a significant strengthening of the stratospheric easterly winds in summer, as well as a systematic weakening of the polar vortex in both hemispheres. In addition, the duration of the polar vortex period is shorter due to the CO_2-induced change in the ozone field. Furthermore, the Brewer-Dobson circulation (BDC) changes as diagnosed by the mass streamfunction. This diagnostic shows that the CO_2-induced acceleration of the residual circulation is systematically damped. But the damping is only significant in the summer shallow branch. Another way to analyze the change in the full transport circulation, the BDC, is the diagnostic of the age of air (AoA). Due to ozone changes an AoA increase can be analyzed in the entire stratosphere, although there are no significant changes in the mass streamfunction in the most regions. The ozone induced changes in the stratosphere also affect the troposphere. The tropospheric polar front jet in the Southern Hemisphere (SH) experiences a systematically weaker shift toward the pole due to a changed ozone distribution. These results make clear that CO_2-induced ozone changes in the stratosphere have a discernible impact on temperature and dynamics there and in the troposphere. This underline the relevance of realistic representations of ozone distributions in climate models.

Contents

Acronyms

AoA	**Age of the (Stratospheric) Air**
BDC	**Brewer-Dobson Circulation**
CFCs	**Chlorofluorocarbons**
CMIP-6	**Coupled Model Intercomparison Project of the 6th Phase**
DJF	**December, January, February**
ECHAM	**European Centre for Medium-Range Weather Forecast Hamburg**
EDJ	**Eddy Driven Jet**
EMAC	**ECHAM MESSy Atmospheric Chemistry**
EPFD	**EP (Eliassen-Palm) Flux Divergence**
GWD	**Gravity Wave Drag**
i.e.	**'Id est' (Latin), means 'that is to say'**
JJA	**June, July, August**
MESSy	**Modular Earth Submodel System**
NH	**Northern Hemisphere**
NOGWD	**Non-Orographic Gravity Wave Drag**
OGWD	**Orographic Gravity Wave Drag**
PSCs	**Polar Stratospheric Clouds**
RMOC	**Residual Meridional Overturning Circulation**
SH	**Southern Hemisphere**
SIC	**Sea Ice Coverage**
SST	**Sea Surface Temperature**
SSW	**Sudden Stratospheric Warming**

STJ	**Subtropical Jet**
TEM	**Transformed Eulerian Mean**
UV	**Ultraviolet**

1 Motivation and Science Questions

1.1 Motivation

Ozone is necessary for life on Earth, because it absorbs/emits high-energetic UV radiation in the stratosphere (Häckel, 2021). Ozone is also an important greenhouse gas. The absorption/emission of shortwave and longwave radiation modifies the temperature especially in the stratosphere. A change in the stratospheric ozone distribution would therefore have an influence on the temperatures in the stratosphere and thus on the dynamics there. This could indicate a relevance of realistic representations of ozone fields in climate models, which has already been investigated in some studies (i.e. Nowack et al., 2018, Chiodo and Polvani, 2019, DallaSanta et al., 2021).

The ongoing climate change is a result of an increase of atmospheric greenhouse gas concentrations. The effect of this is warming of the troposphere and cooling of the stratosphere, which affects the zonal winds. For example, the subtropical jet (STJ) is strengthened and shifted upward, which is caused by a local stronger heating in the upper tropical troposphere (Chiodo and Polvani, 2019). Moreover, the Eddy driven jet (EDJ) is moved poleward in the SH. There are also dynamical effects in the regions above. According to McLandress and Shepherd (2009) and Li et al. (2007), higher concentrations of greenhouse gases in the atmosphere accelerate the Brewer-Dobson circulation (BDC). This enhanced meridional overturning circulation transports trace gases like ozone from the tropical to the extra-tropical stratosphere. As a result, there is a decrease of ozone concentrations in the tropical lower stratosphere and an increase in the extra-tropical stratosphere. Moreover, the cooling in the stratosphere through an increase of the concentrations of atmospheric greenhouse gases weakens the catalytic reaction in the chapman cycle, especially in the upper stratosphere (Nowack et al., 2018). Therefore, a higher net production of ozone exists in this region.

The changed ozone field influences the temperature structure, because ozone absorbs and emits shortwave radiation. Nowack et al. (2018) found out that these ozone changes decrease the temperature in the lower tropical stratosphere through lower ozone concentrations. This in turn leads to a weakening of the water vapor intrusion into the stratosphere (Dietmüller et al., 2014). Furthermore, the temperature in the lower extra-tropical stratosphere increases through higher ozone concentrations (Nowack et al., 2018). The change in the temperature field leads to a weakening of the meridional temperature gradient in the lower extra-tropical stratosphere, which affects the thermal wind balance. Chiodo and Polvani (2019) assert that this modified thermal wind balance is the cause for a negative wind anomaly in the extra-tropical stratosphere. Moreover, they analyzed a downward extension of this anomaly to the troposphere in the SH. As

a result, the CO_2-induced poleward shift of the EDJ in the SH is damped. Moreover, the study from DallaSanta et al. (2021) points out that the ozone changes weaken the tropical upwelling.

1.2 Science Questions

These briefly described studies show examples for thermal and dynamical effects of changes in the ozone field in 4xCO_2-experiments. They illustrate how the temperatures and zonal winds are affected in the troposphere as well as in the stratosphere.
However, a number of the dynamical effects of the ozone changes have not yet been analyzed in detail, in particular the impact on the polar vortices and the BDC. The polar vortex is a dominant stratospheric circumpolar wind in winter. In this study the modification of the strength and the period due to CO_2-induced ozone changes will be analyzed. Beyond that, the influence of ozone on the date of the polar vortex breakdown (final warming) as well as the duration and number of sudden stratospheric warmings (SSWs) will be investigated. The analyses should answer the question, what the impact of ozone changes on polar vortex feature, like strength, period, SSWs and final warmings is. This raises the first science question that is

- *How do the polar vorticies change due to 4xCO_2-induced ozone changes?*

The final warming and SSWs are the result of disturbances of the polar vortex by breaking atmospheric waves. The behavior of these waves (excitation, propagation, dissipation/breaking) is dependent on the meridional temperature structure and on the zonal winds, which are modified by ozone changes. This opens following question:

- *Which impact do 4xCO_2-induced ozone changes have on the wave properties?*

Breaking waves drive a meridional circulation called Brewer-Dobson Circulation (BDC). Thus, a potential modification of the wave breaking due to ozone changes would have an impact on the BDC. The BDC itself is important, because it transports trace gases like water vapor and ozone through the stratosphere. Water vapor, for example, follows the shallow branch and has a thermal radiative impact. Thus, the resulting question is

- *How do 4xCO_2-induced ozone changes affect the BDC and the stratospheric transport?*

The already mentioned SSWs and final warmings as anomalies of the polar vortices can influence the tropospheric dynamics by downward coupling from the stratosphere. Moreover, the downward influence can affect the zonal winds in the troposphere i.e. the EDJ. This leads to another question:

- *How does the tropospheric dynamics react on the 4xCO_2-induced ozone changes?*

In the frame of this thesis, simulations with the ECHAM MESSy Atmospheric Chemistry (EMAC, Jöckel et al., 2005, 2010, 2016) model were set up to answer these questions. The results of these analyses will be shown in chapter 4, the theoretical background with the more detailed formulated state-of-the arts will be provided in chapter 2 and the data and methods will be described in chapter 3. At the end, the results will be discussed in chapter 5 and a summary and conclusion remarks are provided in chapter 6.

2 Theoretical Background and State of the Art

2.1 The Stratosphere

The stratosphere extends from the tropopause at about 10 to 15 km to the stratopause at about 50 km altitude and is stably stratified vertically. This can be seen by a temperature increase from −70 °C at the tropopause to 0 °C at the stratopause. The cause of the positive vertical temperature gradient is largely due to absorption of solar radiation by ozone between 20 and 50 km (Labitzke, 1998). The chemical properties as well as the radiative characteristics are therefore explained in more detail in the following chapters. The temperature dependence of the solar radiation leads to a meridional temperature gradient with seasonal variation. This can be seen in Figure 2.1.

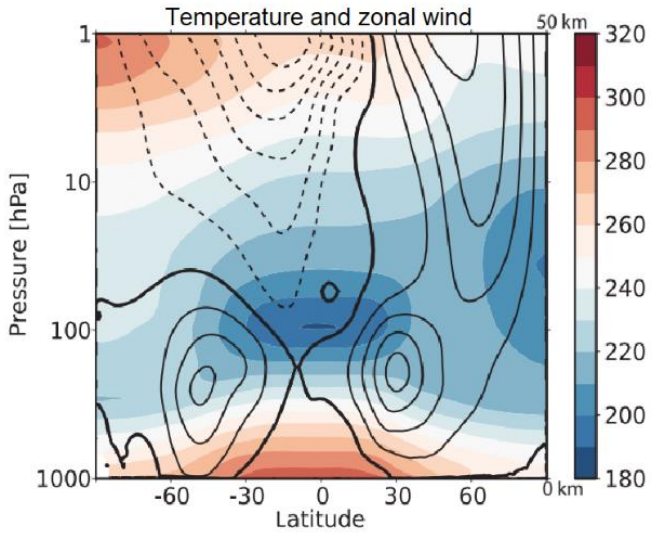

Figure 2.1 (from Vallis, 2017)**:** Temperature (color shading) and zonal wind (contours) for January. Contour interval in 10 m/s and negative values are dashed.

In winter the insolation in the high latitudes is quite weak and the temperature decreases from the equator to the pole. Thermal wind balance then leads to a positive vertical wind shear with strong westerlies. This is also known as the polar vortex (see chapter 2.4.3). In summer a high amount of solar radiation reaches the high latitudes, where it is absorbed by ozone. As a result, the meridional temperature gradient is reversed in comparison to the winter stratosphere. Hence, here the pole is warmer than the tropics and the zonal wind is negative (westwards) in the summer stratosphere. All in all, the temperature gradient is further away from radiative equilibrium in winter. This is caused by a stratospheric meridional overturning circulation that is stronger in the wintertime. This circulation is called Brewer-Dobson circulation (BDC), after its explorer A. W. Brewer and by G. M. B. Dobson, who recognized the lower branch of the circulation during

measurements of water vapor and ozone in the lower stratosphere (Brewer, 1949 and Dobson, 1956). Therefore, the BDC should be discussed in detail in chapter 2.4.4.

2.2 Radiation in the Stratosphere

2.2.1 General Radiation Laws

To understand the behavior of molecules during interaction with radiation, Planck's law (see Equation 2.1) is shortly introduced.

$$B_\lambda\,(\lambda, T)\; = \frac{2hc^2}{\lambda^5}\frac{1}{exp\left(\frac{hc}{kT\lambda}\right) - 1} \tag{2.1}$$

with

- λ= wavelength of the radiation,
- T = temperature of the radiant body,
- h = Planck's quantum of action = $6.62612 \cdot 10^{-34}\,Js$,
- c = speed of light = $2.99792 \cdot 10^{8}\ \frac{m}{s}$,
- k = Boltzmann's constant = $1.38065 \cdot 10^{-23}\,\frac{J}{K}$

This law defines the emission of unpolarized radiation in perpendicular direction from a body, that absorbs the radiation completely. It is dependent on the wavelength of the radiation and the temperature of the body (Kraus, 2004). The unit in Planck's law is the radiative energy per time, wavelength, solid angle area and unit area. This is known as spectral radiance. According to this law, the spectral radiance increases with higher temperature of the black body and shorter wavelength of the radiation. However, for many processes in the atmosphere the total radiance is of interest. The latter is calculated by integration of the spectral radiance over all wavelength and the half space. Then the radiance in the half space is left (Equation 2.2).

$$\pi B_\lambda = \sigma T^4 \tag{2.2}$$

This is the Stefan-Boltzmann law, which states that the total radiance from a black body is proportional to the fourth power of the body's temperature (Kraus, 2004). The constant (Stefan-Boltzmann constant) is calculated to $\sigma = 5.670280 \cdot 10^{-8} \frac{W}{m^2 K^4}$. For a black body the wavelength with the maximum radiance λ_{max} is dependent on the body's temperature. This relationship is described by the Wien's displacement law.

$$\lambda_{max} T = 2.8978 \cdot 10^{-3}\, mK \tag{2.3}$$

Now there is the problem that the Earth's atmosphere is not a real black body. Therefore, the absorptivity $\varepsilon(\lambda) < 1$ should be introduced that quantifies the fraction of outgoing radiation as

$$\varepsilon(\lambda) = \frac{E_\lambda(\lambda,T)}{B_\lambda(\lambda,T)} \tag{2.4}$$

with the emission $E_\lambda(\lambda, T)$. This relation is valid for solid bodies, liquids and gases and shows that they absorb radiation in every wavelength, in which they emit (Kirchhoff´s law: absorptivity = emissivity, according to Kraus, 2004). After this short introduction on radiation, the radiative properties of CO_2 and ozone are discussed next.

2.2.2 Radiative Properties of Atmospheric Gases

Gases, like CO_2 or ozone, absorb radiation in different wavelength intervals. These intervals are also known as 'bands'. Radiation can generally have three sources: The ground of the Earth, the Earth's atmosphere and the sun (Häckel, 2021). The radiation interacts with the molecules by absorption, scattering or reflection.

Radiative Effects of CO_2

For this study, absorption of CO_2 and ozone is of particular interest. For that reason, the emission spectrum of the Earth is shown next (Figure 2.2).

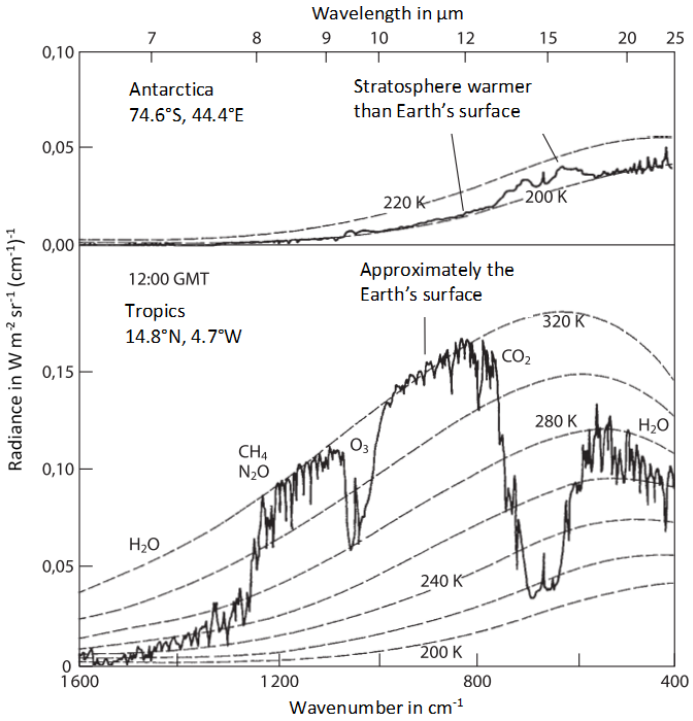

Figure 2.2 (from Kraus, 2004)**:** From the satellite observed emission spectrum in radiance of the Earth over the tropics (bottom) and over the Antarctic (top) shown as a solid line. The dashed curve shows the Planck spectrum for different temperatures. The upper x-axis shows the wavelength μm the lower x-axis shows the wavenumber in cm^{-1}.

If the Earth would not have an atmosphere, the spectrum would be the dashed curve in the lower plot in Figure 2.2 with 320 K. However, an atmosphere, which consist of various gases, partly absorbs radiation emitted from the ground. CO_2 for example, absorbs terrestrial radiation, which causes the local minimum in the longwave spectrum. By the Stefan-Boltzmann law (Equation 2.2), the received terrestrial radiation causes heating in the troposphere. The absorbed radiation is, after Kirchhoff's law, emitted towards the stratosphere and the surface. A higher amount of CO_2 in the atmosphere, leads to a more effective absorption of terrestrial radiation in the lower troposphere. Therefore, less terrestrial radiation reaches the stratosphere. In summary, it remains to be stated, that CO_2 warms the troposphere and cools the stratosphere.

Radiative Effects of Ozone

After the discussion about the radiative effects of CO_2 on the troposphere and stratosphere, it is important for this study to take a closer look at the radiation properties of stratospheric ozone. For this, Figure 2.3 shows the solar radiation spectrum as spectral irradiance for the top of atmosphere (yellow shading) and at the sea level (red shading). The grey line denotes the blackbody spectrum of the Sun's surface.

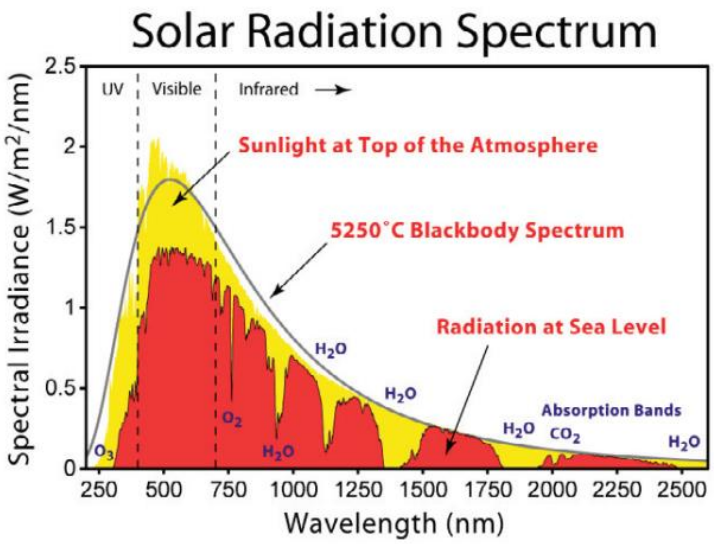

Figure 2.3 (from Wu et al., 2011)**:** Solar spectrum at the top of atmosphere (yellow shading) and at sea level (red shading). The grey line illustrates the blackbody spectrum of the Sun's surface.

On the left side of the Figure 2.3, local minima in the shortwave spectrum can be seen, because ozone absorbs on these wavelengths. The absorption of the radiation happens in different 'bands' (Kraus, 2004), which are called the 'Hartley band' (absorption band between 220 and 290 nm), the 'Huggins band' (absorption band between 300 and 350 nm) and the 'Chappius band' (absorption band between 360 and 760 nm). Within the Hartley band, ozone absorbs the whole solar radiation (Häckel, 2021). This effective absorption is important for the plants and creatures on Earth, because radiation in these bands is high energetic UV radiation, which would destroy the biosphere. In the Huggins band ozone cannot fully absorbs the lower energetic UV radiation (Häckel, 2021).

According to Kirchhoff's law, the absorbed radiation is fully emitted and is proportional to the fourth power of the temperature (Stefan-Boltzmann law, Equation 2.2). This means, that ozone has also a radiative temperature effect. Since the ozone maximum (ozone layer) is located in the stratosphere, the temperature increases with height (Kraus, 2004). The highest stratospheric temperature is above the ozone layer, particularly at the stratopause. This is based on the fact that already above the ozone layer UV radiation is absorbed by a smaller amount of ozone. The amount of ozone in the stratosphere is a result of the photochemical balance that leads to a seasonal and latitudinal dependence of the altitude of the ozone maximum. Therefore, the most important chemical reactions for the formation and decomposition of ozone are treated in the next chapter.

2.3 Ozone chemistry in the Stratosphere

The Chapman Cycle

One important forcing for the chemical ozone formation is the UV radiation, which dissociates molecular oxygen O_2 to atomic oxygen O, like it is described in Equation 2.5 (Kraus, 2004).

$$O_2 + h\nu \rightarrow O + O \tag{2.5}$$

$h\nu$ indicates a radiation quantum, which comprises the absorbed solar radiation by a photon. In case of Equation 2.5 the radiation is below a wavelength of $\lambda \leq 0.24\ \mu m$, Ozone is recombined by the atomic oxygen O (Kraus, 2004). To reach this, molecular oxygen O_2 and a catalyst M, who absorbs energy and momentum, are needed (see Equation 2.6). Common examples for M are di-nitride N_2 or molecular oxygen O_2.

$$2(O + O_2 + M) \rightarrow 2(O_3 + M) \tag{2.6}$$

The net reaction of the Equations 2.5 and 2.6 is $3(O + h\nu) \rightarrow 2O_3$.

In contrast, there are the decomposition reactions of ozone (Equation 2.7 and 2.8), which should balance the total amount of ozone:

$$O + O_3 \rightarrow 2O_2 \tag{2.7}$$

$$O_3 + h\nu \rightarrow O + O_2 \tag{2.8}$$

Equation 2.7 is known as the thermal decomposition. The other decomposition reaction (Equation 2.8) represents the ozone dissociation by absorption in the O_3-bands with wavelengths $\lambda \leq 0.3\ \mu m$. The two decomposition equations combined yield the net reaction $2O_3 + h\nu \rightarrow 3O_2$.

The cycle of formation and decomposition of ozone (Equations 2.5 – 2.8) is called the 'Chapman cycle', which is named by its explorer S. Chapman in the year 1930 (Kraus, 2004).

The Ozone Hole

If a model would only run with the Chapman Cycle, the ozone concentration would be overestimated by a factor of two, because it ignores the catalytic decomposition reactions. Hydroxide radicals *(HO_x)*, nitrogen oxide *(NO_x)* or chlorofluorocarbons (CFCs) are the most common examples for such catalysts (Kraus, 2004). Anthropogenically released gases, like CFCs, have led to stronger ozone losses since the 1970s, especially in the polar region. The most dramatical ozone losses have been observed over the Antarctica. The reasons for these regional strong losses are, that first, the meridional ozone transport (see chapter 2.4.4) for the balance of the losses is weaker in the Southern Hemisphere and second, the stratosphere over the Antarctic is colder than over the Arctic. Due to the lack of solar radiation over the polar caps during winter, the ozone formation is weakened. Another effect of the cooling is the formation of clouds in the stratosphere, the so called Polar Stratospheric Clouds (PSCs). These clouds are observed more often in the lower stratosphere over the Antarctic, than over the Arctic, because the temperature in the Antarctic can easier fall below the threshold for PSC formation. If a PSC is formed, cloud particles with nitrogen oxide NO_x precipitate and by heterogeneous chemistry on its background, di-chlorine molecules Cl_2 are generated. In spring, when the solar radiation comes back, Cl_2 interacts with radiation to a reactive $2Cl$, which again reacts with ozone to molecular oxygen and ClO (Seinfeld and Pandis, 2006). Therefore, the highest ozone losses are measured in early spring. This process is responsible for the ozone hole. The basic knowledge of the chemical as well as the radiative processes in the stratosphere is important to explain the atmospheric temperature and dynamics.

2.4 Dynamics in the Stratosphere

2.4.1 Atmospheric Waves

For the description of stratospheric dynamics, first, some fundamentals of atmospheric waves are explained. Waves are important for the transfer of energy and momentum through the atmosphere (Vallis, 2017), therefore Figure 2.4 shows schematically some fundamental properties of waves.

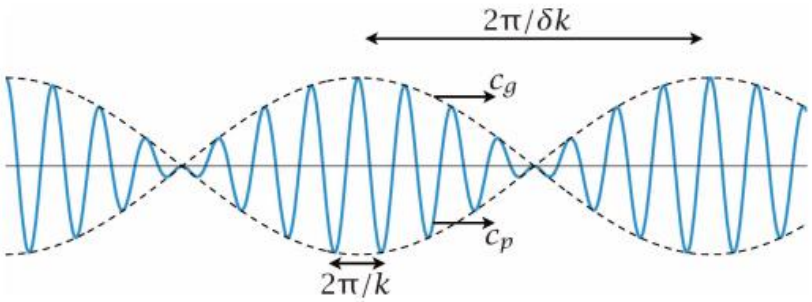

Figure 2.4 (from Vallis, 2017)**:** Superposition of two sinusoidal waves with wavenumber k and k + δk producing a wave (solid line) that is modulated by a slowly changing wave envelope, which is represented by the dashed lines.

The speed of the wave's energy, the group velocity c_g, can be regarded as the velociy of the wave's envelope. The velocity of the wave amplitude, the phase speed c_p is defined as

$$c_p = \frac{\omega}{K} \tag{2.9}$$

with the wave frequency ω and $K^2 = k^2 + l^2 + m^2$, where k, l and m are the horizontal, meridional and vertical wavenumbers. The partial derivative of the phase speed c_p after the wave numbers, which are included in the vector wavenumber (direction of the phase propagation) $\boldsymbol{k} = (k, l, m)$ yield the group velocity c_g.

$$\boldsymbol{c_g} = \left(\frac{\partial\omega}{\partial k}, \frac{\partial\omega}{\partial l}, \frac{\partial\omega}{\partial m}\right) \tag{2.10}$$

Rossby Waves

According to Vallis (2017) one of the most important large-scale waves in the atmosphere are the so called Rossby waves. These waves are created by conservation of potential vorticity q (Equation 2.11), calculated by the sum of the vertical component of the relative vorticity ζ and planetary vorticity $f = 2\Omega sin\varphi$, with the frequency of Earth rotation Ω and latitude φ, divided by the thickness (σ) between to isentropes (lines of constant potential temperature θ).

$$q = \frac{\zeta + f}{\sigma} \tag{2.11}$$

For adiabatic processes the potential vorticity (PV) is conserved, which follows from the conservation of angular momentum. Due to PV conservation, a Rossby wave needs a gradient of potential vorticity to change its relative vorticity by parcel displacement. The relative vorticity itself creates a velocity field, which delocalizes neighboring parcels. A horizontal wavy wind structure is the result of this process. The source of PV gradients on the Earth is the change of the planetary vorticity (tangential rotation of the planet) with latitude, called $\beta = \frac{\partial f}{\partial \varphi}$. Therefore, large-scale Rossby waves are also called planetary waves. On the Earth the PV is higher at the poles than at the equator, which creates a positive meridional PV gradient. Such PV gradients lead to a westerly flow, which can be deflected by topography or synoptic eddies (Holton, 2013). Through PV conservation the flow turns into a Rossby wave. If the flow would be easterly, Rossby waves could not be formed. The zonal phase speed c_p^x relative to the (westerly) mean-flow $\bar{u}$, the intrinsic phase speed of the Rossby waves (Equation 2.12a) is negative (westward propagation) and is defined as

$$c_p^x - \bar{u} = -\frac{\beta}{k^2 + l^2 + m^2 + k_d^2}, \tag{2.12 a}$$

$$c_p^y - \bar{u}\frac{m}{l} = -\frac{\beta k}{l(k^2 + l^2 + m^2 + k_d^2)}, \tag{2.12 b}$$

$$c_p^z - \bar{u}\frac{k}{m} = -\frac{\beta k}{m(k^2 + l^2 + m^2 + k_d^2)} \tag{2.12 c}$$

with the inverse of the internal radius of deformation $k_d^2 = L_d^{-2}$. The radius of deformation represents the length scale over which the flow is in equilibrium between the pressure gradient and the Coriolis force (Holton, 2013). Rossby waves can also propagate vertically. To aim this, the air has to be stably stratified and the mean-flow $\bar{u}$ must be westerly. Moreover, the mean-flow $\bar{u}$ has to be lower than the critical wind U_c. Therefore, the final condition for vertically propagating stationary waves ($c_p^x = 0$) is $0 < c_p^z - \bar{u} < \frac{\beta}{k^2+l^2+\frac{{f_0}^2}{4N^2H^2}} = U_c$, which is called the Charny-Drazin condition. Where *N* represents the buoyancy frequency, f_0 stands for the Coriolis parameter at a constant latitude φ_0 and $\gamma = k_d^2 = L_d^{-2}$. With these three conditions, analyses of the vertical direction of propagation are possible.

To do so, the vertical component of the group velocity c_g^z (Equation 2.13) from Vallis, 2017, must be considered first.

$$c_g^z = \frac{2\beta k m {f_0}^2/N^2}{(k^2+l^2+m^2+{f_0}^2/N^2+\gamma^2)^2} \tag{2.13}$$

According to the definition of the vertical group velocity c_g^z (Equation 2.13), an analysis of the direction of vertical energy propagation is possible. For this purpose, Figure 2.5 should be regarded. The Figure illustrates a vertical westward tilt of phases (solid lines), which can be interpreted as lines of constant pressure.

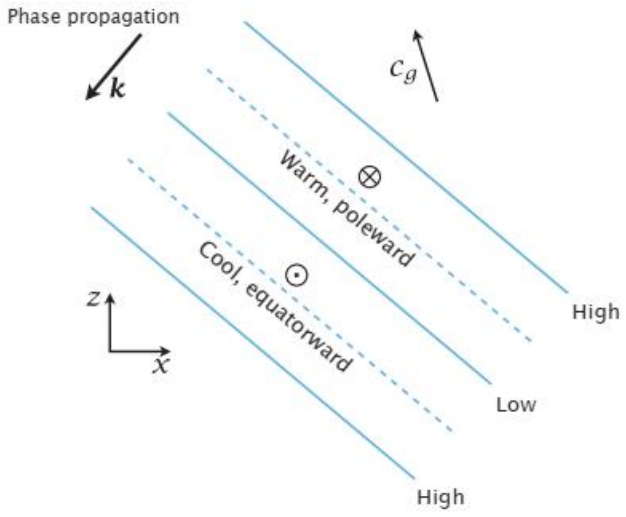

Figure 2.5 (from Vallis, 2017)**:** East-west cross-section of phases. The solid lines denote regions of constant phase. 'High' and 'Low' refer to pressure values. In this case, there is a downward propagation of the phases (represented by the k-vector) and an upward propagation of the group velocity (energy).

Along a constant phase ϕ_0,it applies: $\phi_0 = kx + mz + \omega t$. Neglecting the time *t*, *z* can be expressed as

$$z\,(t=0) = \frac{\phi_0}{m} - \frac{k}{m}x \tag{2.14}$$

If the phase has a westerly vertical tilt (as in Figure 2.7), *k* and *m* have to have the same sign by definition of *z(t=0)* (Equation 2.14). That results, after Equation 2.13, in a positive vertical component of the group velocity c_g^z and consequently to an upward energy transport. For the case of an easterly tilt, it is vice versa.

Gravity Waves

Another form of waves in the atmosphere are gravity waves. They only exist in a stably stratified fluid (Holton, 2013), as for example in the stratosphere. Because the buoyancy is the responsible restoring force, these waves are also called buoyancy waves. Gravity waves can propagate horizontally and vertically. Vertically propagating gravity waves are referred as internal gravity waves and can, like Rossby waves, propagate from the troposphere to the stratosphere (Vallis, 2017) with the three-dimensional phase speed

$$c_p^x = \frac{f^2}{k} - \frac{N^2(k^2+l^2)}{km'^2},\ c_p^y = \frac{f^2}{l} - \frac{N^2(k^2+l^2)}{lm'^2},\ c_p^z = \frac{f^2}{m} - \frac{N^2(k^2+l^2)}{mm'^2} \tag{2.15 a, b, c}$$

where $m' = 1 + \frac{1}{4H^2}$, with a reference height *H*. Normally, $\frac{1}{4H^2}$ is quite small, so that $m' \approx m$. With this approximation and the assumption, that $l \ll k$, the group velocity of the internal gravity wave has the form

$$c_g^x = \frac{N^2 k}{\omega m^2} = \frac{N^2}{\omega m}\cos\vartheta\,, \qquad c_g^z = \frac{N^2(k^2+l^2)m}{\omega m^4} = \frac{-N^2}{\omega m}\cos^2\vartheta \tag{2.16 a, b}$$

with the substitution $cos\,\vartheta = \frac{k^2}{(k^2+m^2)} \approx \frac{k^2}{m^2} \ll 1$. Regarding Equation 2.16 a, b, the direction of the group velocity $\boldsymbol{c_g}$ is dependent on the sign of the vertical wavenumber m. As an illustration for the wave's behaviour, Figure 2.6 depicts schematically a vertical cross-section of lines with constant phases, similar to Figure 2.5.

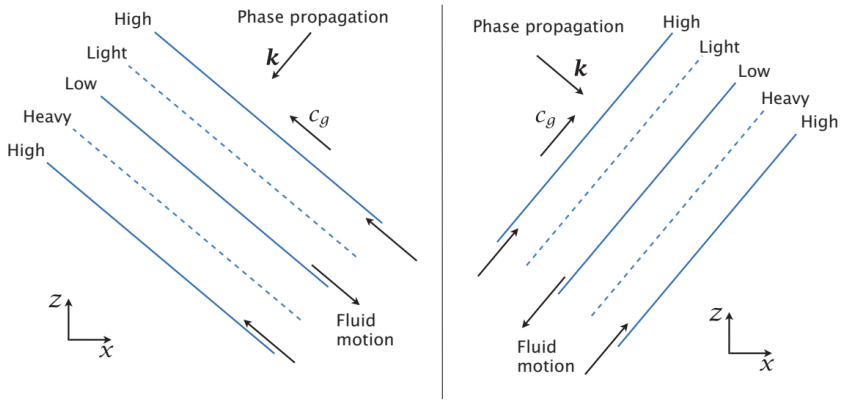

Figure 2.6 (from Vallis, 2017)**:** Like in Figure 2.5, but for internal gravity waves. For westerly and easterly tilt, the phase speed is directed downward and the group velocity is directed upward.

With a negative m, the energy, which is represented by the group velocity goes upward. The direction of the group velocity does not depend on the vertical phase tilt.

One way for the generation of internal gravity waves is flow over a bottom topography. The boundary condition of internal gravity waves, with a mean-flow in x-direction $\bar{u}$ and without variation in y-direction, is $\omega(x, z = 0) = \bar{u}\frac{\partial h}{\partial x}$ with the vertical velocity ω and the height h of the idealized sinusoidal topography (Vallis, 2017). This kind of internal gravity waves are also known as orographic gravity waves. For a vertical propagation of the orographic gravity wave, the frequency of the topography $\bar{u}k$ has to be smaller than the buoyancy frequency N ($\bar{u}k < N$). As the waves are excited on a rotating planet, the frequency has to be higher than the Coriolis parameter f. Therefore, the final condition of the topographical frequency $\bar{u}k$ for a wave propagation is $f < \bar{u}k < N$. In the case, that the frequency is higher than the buoyancy frequency N, the waves are evanescent and are damped exponentially with height, which leads to a trapping near the topography. Internal gravity waves can be generated non-orographically, too and are then called non-orographic gravity waves. These waves have their source for example in the (tropical) convection or in the wind shear (Fritts and Alexander, 2003). However, the excitation of gravity waves cannot be resolved by climate models, because the processes of their sources are not fully

resolved. For that reason, gravity waves are also known as unresolved waves and a more detailed discussion of their mechanisms should not be the focus of this study.

2.4.2 Wave-mean-flow interaction

The Transformed Eulerian Mean

After a general overview of the most important waves in the stratosphere, the Rossby and gravity waves, the interaction between these waves and the mean-flow will be explained. The theory of the wave-mean-flow interaction says, that waves propagates upward from the troposphere and dissipates, which leads to a forcing on the zonal mean-flow, this influences the polar vortex and generates the residual meridional circulation (Vallis, 2017). The latter is also called the residual meridional overturning circulation (RMOC), or the Brewer-Dobson circulation (see chapter 2.4.4). But to describe this mechanism, first, the Eliassen-Palm-Flux (EP flux) is introduced. The EP flux is described as a two-dimensional vector

$$\boldsymbol{\mathcal{F}} = (0, \mathrm{F_y}, F_z) \equiv -\overline{u'v'}\,\boldsymbol{j} + \frac{f_0}{N^2}\overline{v'b'}\,\boldsymbol{k} \tag{2.17}$$

where $\boldsymbol{j}$ and $\boldsymbol{k}$ are standard vectors in the y- and z-direction. u' and v' represent the zonal anomaly of the zonal wind *u* and meridional wind *v* and the zonal mean of the product of them ($\overline{u'v'}$) can be regarded as zonal momentum flux. b' is the zonal anomaly of the buoyancy *b*, which is a temperature-like variable. Therefore, $\overline{v'b'}$ stands for the zonal mean poleward heat flux. This means, that a meridional heat flux is needed for a vertical wave propagation.

As already mentioned, the EP flux describes how the wave activity density $\mathcal{A}$ and the wave dissipation $\mathcal{D}$ behave, which shows the Eliassen-Palm relation (Equation 2.18).

$$\frac{\partial \mathcal{A}}{\partial \mathrm{t}} + \nabla_{\mathrm{x}} \cdot \boldsymbol{\mathcal{F}} = \mathcal{D} \tag{2.18}$$

The relation says that the sum of the EP flux divergence $\nabla_{\mathrm{x}} \cdot \boldsymbol{\mathcal{F}}$ and the change of the wave activity density $\mathcal{A}$ with time is equal to the wave dissipation $\mathcal{D}$. For a Rossby wave, the wave activity density and the EP flux is connected by the group velocity $\boldsymbol{c_g}$ (Equation 2.19).

$$\boldsymbol{\mathcal{F}} = (0, F_y, F_z) = \mathbf{c_g}\mathcal{A} \tag{2.19}$$

Now, there is the open question, what happens, if the wave dissipation interacts with the mean-flow. To answer this problem, a look on the Transformed Eulerian Mean (TEM) equations (Equation 2.20), which are transformations of the equations of motions, are considered. The TEM equations provide a simple separation between adiabatic and diabatic effects and between advective and diffusive fluxes. In these equations, $N^2 = \frac{\partial b_0}{\partial z}$, $\bar{S}$ represents the zonal mean of the diabatic effects, b_0 is the buoyancy in the basic state condition and $\bar{b}$ is regarded as the zonal mean buoyancy (Vallis, 2017).

$$\frac{\partial \bar{u}}{\partial t} - f_0 \bar{v}^* = \nabla_x \cdot \boldsymbol{\mathcal{F}}, \qquad \frac{\partial \bar{b}}{\partial t} + \bar{w}^* N^2 = \bar{S} \tag{2.20 a, b}$$

The y- and z-components of the residual circulation $\bar{v}^*$ and $\bar{w}^*$ are expressed as

$$\bar{v}^* = \bar{v} - \frac{\partial}{\partial z}\left(\frac{1}{N^2}\overline{v'b'}\right), \qquad \bar{w}^* = \bar{w} + \frac{\partial}{\partial y}\left(\frac{1}{N^2}\overline{v'b'}\right) \tag{2.21 a, b}$$

Non-Acceleration Theorem and Downward Control

If the divergence of the EP flux is zero ($\boldsymbol{\nabla_x \cdot \mathcal{F} = 0}$) and the waves are steady ($\frac{\partial \mathcal{A}}{\partial t} = 0$) and dissipationless ($\mathcal{D} = 0$), then according to Equation (2.20 a), there is no wave-induced acceleration of the mean-flow $\bar{u}$. This is known as the 'non-acceleration' result. In reality there is wave-breaking or dissipation and $\nabla_x \cdot \boldsymbol{\mathcal{F}} < 0$. The result is a wave drag, which leads to a deceleration of the flow and/or a poleward residual meridional velocity. An idealized schematic cross-section of a such wave-driven circulation, with an upward movement over the tropics and a downward movement over the extra-tropics is shown in Figure 2.7 from Holton and Hakim (2013). There, a

latitude-height cross-section of the stratospheric residual flow (solid arrows) and the wave-driven 'pump' (shaded area) is sketched.

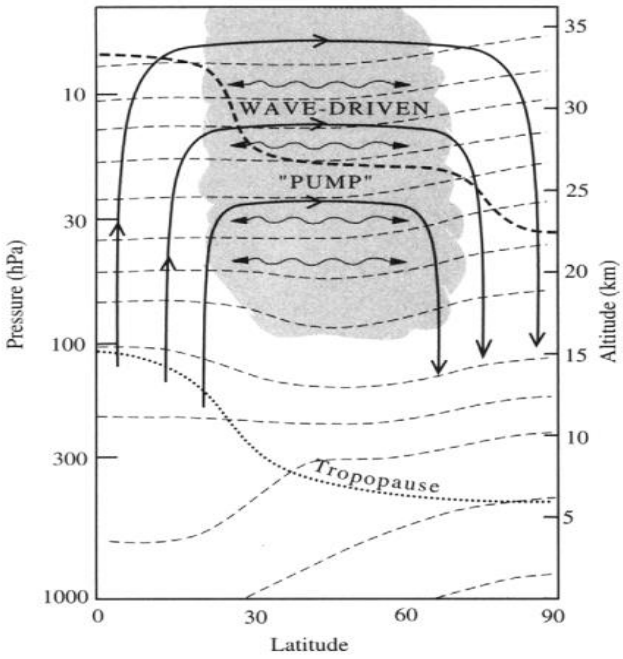

Figure 2.7 (from Holton and Hakim, 2013): Schematic latitude-height cross-section of the wave-driven circulation in the middle atmosphere. Thin lines represent isentropes (surface of constant potential temperature). The dotted line is the tropopause. Solid lines are the TEM meridional circulation, which is driven by the waves. Also known as wave-driven "pump" (shaded region). The wavy arrows denote the meridional transport and the mixing by eddies. The heavy dashed line shows a line of constant mixing ration for a long-lived tracer.

For the steady state without momentum forcing, the vertical velocity at the height *z* is generated by the wave forcing above that height (Holton and Hakim, 2013). The process is acting after the so called 'downward control' principle. A mathematical expression of the mechanism was derived by Haynes et al. (1991) in form of the streamfunction Ψ for a given height *z* and latitude φ (Equation 2.22).

$$\Psi(\varphi, z) = \int_z^{\infty} \left\{ \frac{\rho_0 a^2 \bar{F} \cos^2\varphi}{\bar{m}_\varphi} \right\}_{\varphi=\varphi(z')} dz' \tag{2.22}$$

The streamfunction is linked to the vertical residual velocity $\bar{w}^* = \frac{1}{a\rho_0 \cos\varphi} \frac{\partial}{\partial\varphi}\{\Psi(\varphi, z)\}$, where ρ_0 is the basic state density, a represents the Earth's radius, $\bar{F}$ stands for the zonal wave drag and

$\bar{m}_\varphi$ is the angular momentum. With the hydrostatic balance ($\frac{\partial p}{\partial z} = -\rho_0 g$), where g is the gravitational acceleration and p is the pressure, Equation 2.22 can be transformed to pressure coordinates by substitution to (according to Okamoto et al., 2011)

$$\Psi(\varphi, p) = \frac{\cos\varphi}{g} \int_p^0 \frac{\bar{F}}{\hat{f}} dp'. \tag{2.23}$$

Where $\hat{f}$ is defined as

$$\hat{f} = f - \frac{1}{r_0 \cos\varphi}\left(\frac{\partial(\bar{u}\cos\varphi)}{\partial\varphi}\right) = 2\Omega\sin\varphi - \frac{1}{r_0}\frac{\partial\bar{u}}{\partial\varphi} + \frac{\bar{u}\sin\varphi}{r_0\cos\varphi}. \tag{2.24}$$

The resulting circulation that is called the residual circultation is important for the net mass transport of trace gases, like ozone, in the stratosphere. The tracer transport happens also through isentropic mixing and eddy motions (motions by low-pressure-systems in the mid-latitudes). The residual circulation in the stratosphere will be discussed in more detail in chapter 2.4.4.

2.4.3 The Polar Vortex and Sudden Stratospheric Warmings (SSWs)

Now, the focus is directed on dynamical processes in the stratosphere. As explained in chapter 2.1, the stratosphere reacts sensible on solar radiation, which has an effect on the meridional temperature gradient $\frac{\partial T}{\partial y}$ and, following the thermal wind balance for the x-component (Equation 2.25), also on the zonal vertical wind shear $\frac{\partial \bar{u}}{\partial ln(p)}$ (Holton, 2013). The constant R in the thermal wind balance is the gas constant.

$$\frac{\partial \bar{u}}{\partial ln(p)} = \frac{R}{f}\left(\frac{\partial T}{\partial y}\right)_p \tag{2.25}$$

In winter, less solar radiation reaches the polar stratosphere and its air cools. The result is a negative meridional temperature gradient. According to Equation (2.25), a negative meridional

temperature gradient increases the zonal vertical wind shear (Vallis, 2017). The zonal wind over the temperature gradient accelerates with height. At the end, a strong circum-polar westerly flow in the stratosphere, the polar vortex, is formed. The strong wind of the vortex isolates the cold air inside and therefore prevents the mixing of chemical species, like ozone catalysts with the air of lower latitudes. The location of the polar vortex depends on the location of the strongest equator-to-pole temperature gradient. Therefore, the polar vortex is located over the mid-latitudes. In Figure 2.1, the polar vortex is shown as the solid contours in the stratosphere of the NH (right side). There is also a strong negative temperature gradient in the lower stratosphere, which is consistent with the thermal wind balance.

The polar vortex can also be disturbed by vertically propagating planetary waves (see chapter 2.4.2), whose tropospheric forcing is strongest in winter. However, only larger-scale waves can reach the polar vortex, which is known as Charney-Drazin filtering. If there is an interaction of these waves with the polar vortex by wave-breaking, then, with the condition that $\frac{\partial \mathcal{A}}{\partial t}$ is positive and dissipation $\mathcal{D}$ is small, $\nabla_x \cdot \boldsymbol{\mathcal{F}}$ turns negative (see Equation 2.18). According the zonal momentum Equation in the TEM form (Equation 2.20 a) for a steady-state, the wave induces a deceleration of the polar vortex and/or a poleward meridional flow. A weaker zonal mean flow favors that more planetary waves to propagate up to the stratosphere until the zonal mean flow is smaller than the intrinsic phase speed $\bar{u} - c_p^z$, as it is described in chapter 2.4.1.
If the process continues, the zonal mean zonal wind may flip to zonal mean easterly wind ($\bar{u} < 0$) and the propagation of planetary waves is interrupted. The result is a weaker or reversed zonal vertical wind shear, which leads (by thermal wind balance, Equation 2.25) in the extreme case to a negative meridional temperature gradient and the polar winter stratosphere warms. Sometimes such an event is strong enough to even split or at least displace the polar vortex horizontally (Vallis, 2017). Then the event is known as sudden stratospheric warming (SSW).

To summarise the wave-mean-flow dynamics of a stratospheric warming, Figure 2.8 from Vallis (2017) is presented. On the left side (Figure 2.8 a) upward propagating planetary waves break in the stratosphere. The wave activity, here it is called $\mathcal{P}$, vanishes and the EP flux divergence is negative ($\nabla_x \cdot \boldsymbol{\mathcal{F}} < 0$). That leads to a deceleration of the mean flow ($\frac{\partial \bar{u}}{\partial t} < 0$). The right side (Figure 2.8 b) shows the resulting temperature change. With the assumption, there is no acceleration of the zonal winds far away from the wave-breaking, the lower polar stratosphere warms due to thermal wind balance. In Figure 2.8 b the response of the residual circulation (black arrows) can also be seen. The residual circulation in the stratosphere is a part of the BDC, whose mechanism is explained in more detail in the next chapter.

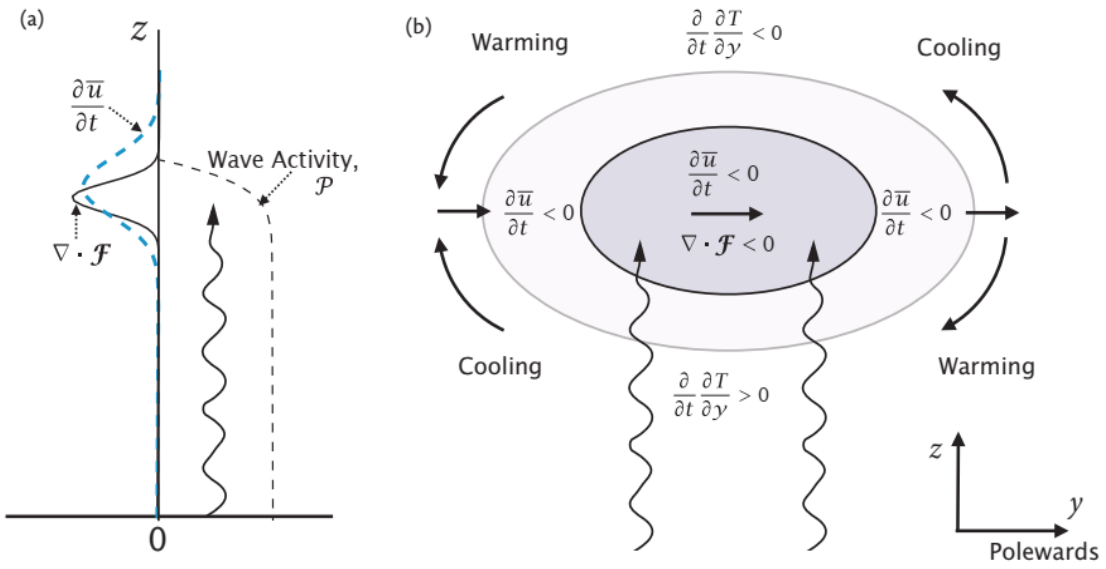

Figure 2.8 (from Vallis, 2017)**:** The wave-mean-flow dynamics of a sudden stratospheric warming. **a)** Wavy arrows represent upward propagating Rossby waves and the dashed line is the wave activity. The EP flux divergence due to wave-breaking is shown by a solid line. This induces a negative response on the acceleration of the mean flow (dashed blue line). **b)** The circulation and temperature response induced. The EP flux convergence, which induces a westward forcing on the mean flow, is shaded dark. The westward forcing on the broader region is marked with a light shading. The arrows show the induced residual circulation.

2.4.4 The Brewer-Dobson Circulation and Ozone Transport

Residual Circulation and Brewer-Dobson Circulation (BDC)

The BDC was explored by A. Brewer (1949) and G. Dobson (1956), when they analyzed observation of water vapor and ozone transport. The residual circulation in the stratosphere is a part of the BDC. Therefore, Figure 2.9 illustrates the residual circulation in a form of a latitude-height cross-section of the troposphere, stratosphere and mesosphere. The arrows depict the circulation.

First, the focus will be on the BDC, whose branches schematically illustrated by the arrows in the stratosphere (see Figure 2.9). The whole BDC is characterized by an upwelling part over the tropics, which is called ‘tropical upwelling’, movement from the equator to the poles and a descending part over the mid and high latitudes. In the lower stratosphere, there are two circulation cells, called the shallow branches. Moreover, there is a bigger branch in the winter hemisphere, which reaches up to the upper stratosphere, called the deep branch. In the lower tropical stratosphere low ozone air enters from the troposphere. Furthermore, the BDC has an effect on the temperature. The upwelling in the tropics cool the air by adiabatic expansion. The downwelling in the extra-tropics, on the other hand, compresses the air adiabatically and the

temperature increases (Holton, 2013). The formation of the BDC is based on the theory of wave-mean-flow interaction, which was discussed in chapter 2.4.2. The wave-breaking in the stratosphere causes a residual circulation based on the 'downward-control' principle. The two BDC branches are driven by breaking waves on different scales (Bönisch et al., 2011). The deep branch, which extends until the stratopause, is generated by wave-mean-flow interaction of the polar vortex, which mainly happens by breaking large-scale Rossby waves (wavenumber 1,2 and 3) as it is described in chapter 2.4.3. Therefore, the deep branch exists only in the winter hemisphere. The breaking of smaller-scale waves at the STJ, a strong zonal wind at the subtropical tropopause, is responsible for the shallow branch.

Another important property of the BDC is the dependence of the circulation strength with the season. The stronger activity in vertical wave propagation in winter accelerates the BDC and thus the tracer transport. Furthermore, it is notable, that the forcing of the Rossby wave has even an effect on the strength and expansion of the tropical tropospheric circulation, named the Hadley cell (Plumb et al., 2002).

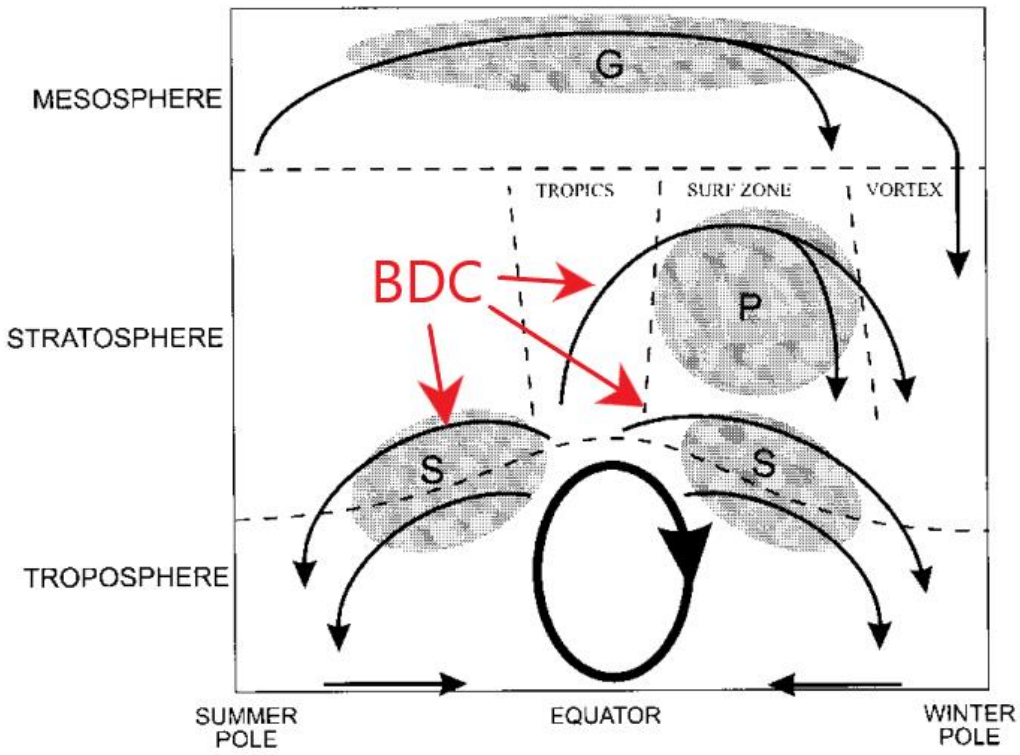

Figure 2.9 (from Plumb, 2002): Schematic of the BDC as combined effect of residual circulation in the atmosphere. Black arrows depict the TEM mass streamfunction, that should represent the residual circulation. The BDC branches, as a part of the residual circulation in the stratosphere, are directed by the red arrows. The thick ellipse represents the Hadley circulation. The shaded fields mark the regions of breaking waves. The labels 'S', 'P' and 'G' indicates the type of the breaking waves (S=synoptic-scale wave, P=planetary-scale wave, G=gravity wave). The dashed lines are the stratospheric transport barriers.

For completeness, the mesospheric residual circulation will be explained as well. The circulation in the mesosphere is characterized by a one-cell global circulation from the summer to the winter pole (see top of Figure 2.11). The driver for this circulation is mostly the breaking of inertial gravity waves, which can propagate up to the mesosphere, where they break. Altogether, there is a net transport from the summer to the winter pole, because the upwelling part of the Brewer-Dobson circulation is located on the summer side. The upwelling part has to be in the summer hemisphere, because then the angular momentum is conserved.

Mean Age of Air (AoA)

The strength of the BDC influences the transport processes in the stratosphere. A diagnostic of tracer transport is the age of an air parcel moving through the stratosphere that is called the mean age of the air (AoA). According to Kida (1983), the age of an air parcel is defined as the time elapsed since its entry therein. Kida (1983) first applied the concept of finding the AoA in a General Circulation Model (GCM) by investigating the general circulation of air parcels and transport. This study showed that the polar stratosphere consists of long-term residing air, while "younger" air parcels from tropospheric origin can be found in the tropical stratosphere. This was done by Hall and Plumb (1994), which will be shown in the methods chapter (see chapter 3.2.4). Today, the AoA diagnostic is widely used in analysis of stratospheric transport in climate models and observations, e.g. Birner and Bönisch (2011), Garny et al. (2014), Stiller et al. (2017), Eichinger et al. (2019). Moreover, for analysis the BDC strength can be derived by using AoA (Waugh and Hall, 2002).

The Ozone Transport

It was already mentioned that the BDC transports ozone in the stratosphere. Figure 2.10 depicts the resulting stratospheric annual mean ozone field in a latitude-height cross-section.

Globally, the highest ozone production is in the tropical middle and upper stratosphere, because the high solar radiance causes a quite effective photo-chemical ozone production (see chapter 2.3). From there, the ozone is moved first poleward and then, over the poles, downward by the BDC (Holton, 2013). With the climate change and the accompanying CO_2-increase, the temperature fields as well as the dynamics in the atmosphere changes. These effects will be discussed next.

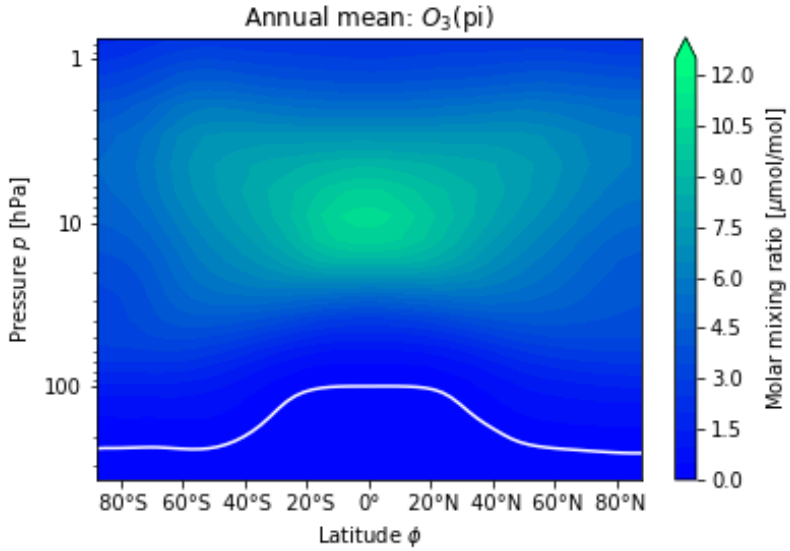

Figure 2.10: Latitude-height cross-section of the annual-mean zonal-mean ozone field for pre-industrial (pi) CO_2-conditions in µmol/mol. The solid white line represents the tropopause.

2.5 Influence of a CO_2-increase on Stratospheric Dynamics

2.5.1 Impact of CO_2-increase on Zonal Winds

As discussed in chapter 2.2.2, an increase of the CO_2 concentration leads to a heating in the troposphere and a cooling in the stratosphere. Therefore, in this sub-chapter the effects of a quadrupled CO_2-concentration on temperature and dynamics are shown. Here, it will be depicted and analyzed only impacts of CO_2 which have been already explained in some studies (i.e. Li et al., 2008, McLandress and Shepherd, 2009, Chiodo and Polvani, 2019 and Shaw, 2019) and are meanwhile well understood.

Figure 2.11 illustrates the response of 4xCO_2 on the latitude-height zonal mean temperature field (Figure 2.11 a) and zonal wind field (Figure 2.11 b). These Figures are generated with data from the simulations that are used for this study (see chapter 3.1).

However, the temperature changes are not meridionally uniform, as depicted in Figure 2.13 a). In the upper troposphere the strongest warming takes place over the tropics, because with upper tropospheric heating the amount of water vapor in the troposphere increases. Therefore, in the convective tropical troposphere more water vapor condenses and the latent heat release increases (Shaw, 2019), comprising an additional heating effect. The result is a stronger equator-to-pole temperature gradient. By the thermal wind balance, the vertical wind shear is enhanced and the zonal mean zonal wind at the upper flank of the STJ accelerates as well as shifts upwards.

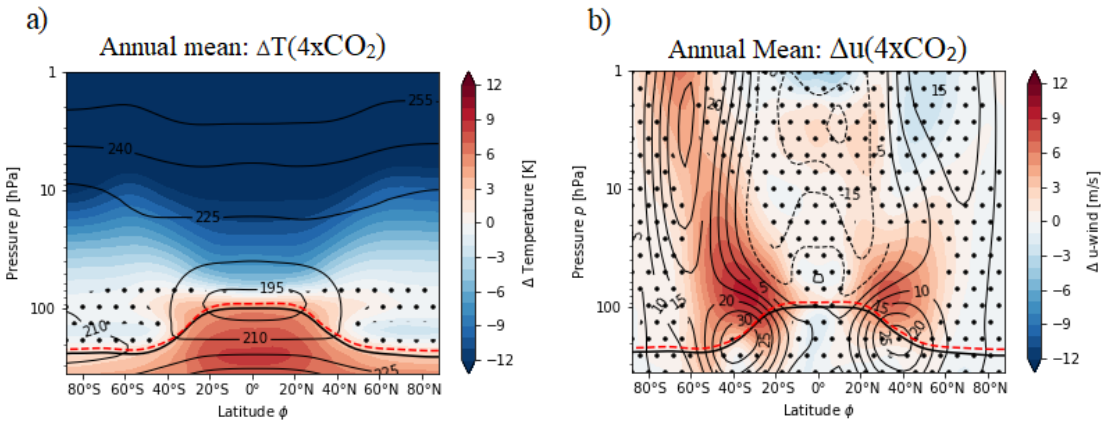

Figure 2.11: Annual mean climatology of the zonal mean **a)** temperature effects and **b)** zonal wind due to 4xCO_2 with respect to pre-industrial (pi) CO_2 concentrations in the stratosphere and upper troposphere. The thin black lines represent the climatological pi-conditions of the temperature (in Kelvin) or of the wind (in m/s). The thick line depicts the pi-tropopause and the dashed red line shows the 4xCO_2-tropopause. Dots mark regions, where the significance is below of the 95-%-confidence interval.

2.5.2 Impact of CO_2 increase on the Polar Vortex

Another prominent signal due to CO_2-increase is a strengthening of the Antarctic (SH) polar vortex, which is shown in the study of Chiodo and Polvani (2019). This can be even seen in the annual mean zonal wind (see Figure 2.11 b). The strengthening of the SH polar vortex is a result of increased greenhouse gases and ozone depletion, which leads to stratospheric cooling (Thompson et al., 2002, Marshall, 2003, Eyring et al., 2013 and Son et al., 2018). Furthermore, the enhancement of the SH polar vortex is linked to a longer season with a later final warming (Ayarzagüena et al., 2020).

The simulated ozone recovery in the SH during the twenty-first century causes a counteracting effect, especially in spring when more solar radiation is absorbed by a higher amount of Antarctic stratospheric ozone. However, the exact rate and extent of ozone recovery and accompanied reversal in the polar vortex changes differ across several climate models (Screen et al., 2018).

According Garfinkel et al. (2017), Seviour (2017) and Kretschmer (2018), the Arctic (NH) polar vortex has become weaker over the last three or four decades. The reason for this observed decrease of the NH polar vortex strength has not be fully explained. Kim et al. (2014) speculate that the asymmetric NH sea ice loss results in an increased vertical wave propagation. This causes an enhanced wave breaking with a deceleration of the polar vortex in the stratosphere. Additionally, the season gets longer through an earlier vortex build up and a later final warming (Ayarzagüena et al, 2020).

Future simulations contain a wide spread of solutions within the internal atmospheric variability. For example, there are uncertainties if the number of SSWs increased or decreased in the NH.

The reason for this intermodel spread of the NH polar vortex response due to climate change could not be comprehended with common theories until today (Wu et al., 2019).

2.5.3 Impact of CO_2 increase on the Brewer-Dobson Circulation (BDC)

The impact of a CO_2 increase on the BDC are well understood. For this reason, Figure 2.12 depicts the change due to $4xCO_2$ on the mass streamfunction, which describes the circulation, for the mean over June, July and August (JJA, Figure 2.12 a) and for the mean over December, January and February (DJF, Figure 2.12 b).

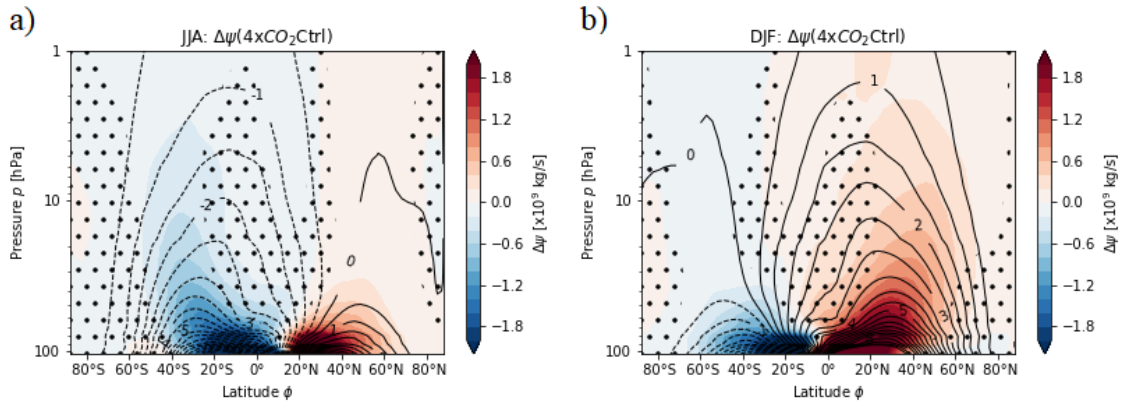

Figure 2.12: Latitude-height cross-section for the response of the mass streamfunction on $4xCO_2$ for the mean over **a)** JJA and **b)** DJF. Black contours depict the pi-climatology of the mass streamfunction in intervals of $5x10^8$ kg/s. Dashed lines are negative values, solid lines are positive values. The dotted regions, which lie outside the 95-%-confidence interval.

The CO_2 increase enhances significantly the BDC in both hemispheres for the winter and summer time. According to McLandress and Shepherd (2009) this forcing has its source in a stronger easterly forcing due to enhanced wave-breaking at the STJ. The stronger wave-breaking is a result of the upward shift and strengthening of the STJ as a response to tropical upper tropospheric heating. According the Charney-Drazin condition (see chapter 2.4.1) the stronger and higher located STJ leads to an enhanced wave forcing on a certain level. Following the 'downward control' principle (Equation 2.24) the residual circulation at and below this level strengthens and the BDC accelerates.

2.6 Ozone Effects on Dynamics in Climate Simulations

2.6.1 Ozone Changes due to 4xCO_2

As already mentioned, a higher CO_2-concentration strengthens the BDC and therefore also the ozone transport. Figure 2.13 depicts the changes in zonal mean ozone in units of number density, if the amount of CO_2 in the atmosphere is quadrupled.

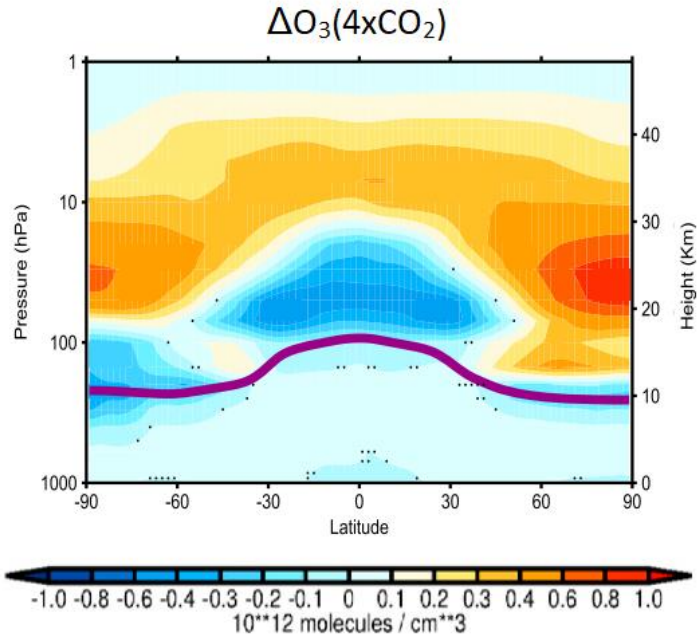

Figure 2.13 (from Chiodo and Polvani, 2019): Latitude-height cross-section of the annual mean ozone response on 4xCO_2 in units of number density (10^{12} molecules/cm^3). The purple line illustrates the tropopause for pre-industrial CO_2-conditions. Non-significant responses at the 95 % confidence level are stippled.

In the lower tropical stratosphere, the ozone concentration decreases, because the stronger upwelling enhances the intrusion of more tropospheric air with low ozone amount into the lower tropical stratosphere. On the other hand, more ozone is observed in the upper tropical stratosphere. There, the CO_2-induced stratospheric cooling weakens the catalytic destruction of the Chapman cycle. The BDC transports the air from this region to the extra-tropics (Chiodo and Polvani, 2019).

2.6.2 Impact of Ozone Changes on Temperatures

Due to radiation properties of ozone, a change in the amount of ozone modifies the temperature field. Therefore Figure 2.14 illustrates the temperature response in the troposphere and lower stratosphere on the ozone changes.

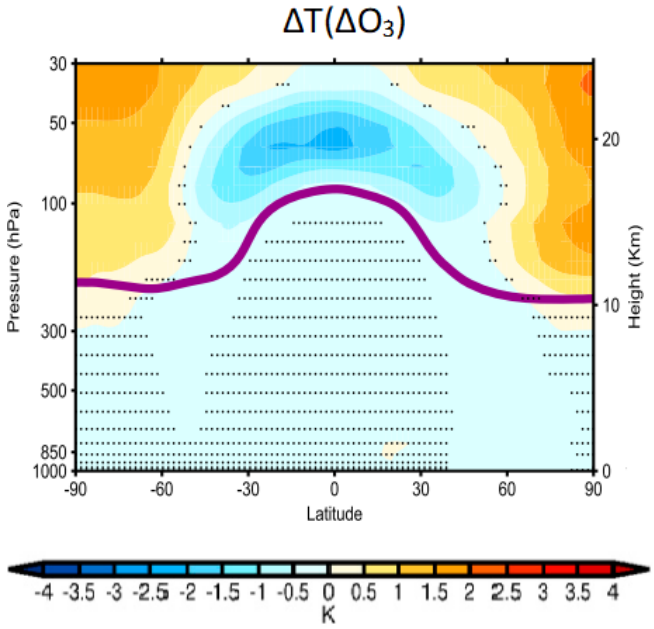

Figure 2.14 (from Chiodo and Polvani, 2019): Latitude-height cross-section of the annual mean temperature response on ozone changes due to 4xCO_2. The purple line illustrates the tropopause wind for pre-industrial CO_2-conditions. Non-significant responses at the 95 % confidence level are stippled.

A decrease of ozone in the lower tropical stratosphere (see Figure 2.14) reduces the absorption of radiation there. The result is a cooling in this region. In the rest of the lower stratosphere, the temperatures increase by an increase of ozone. According Nowack et al. (2018) the ozone changes in the stratosphere affect even the surface temperatures. They conclude that neglecting ozone changes in climate simulations would lead to an overestimation of the global surface warming by around 20 %. In some regions, like in the Barent Sea, the surface temperature effect is even larger. Nevertheless, in other studies (i.e. Dietmüller et al., 2014 and Marsh et al., 2016) the effect on the surface temperatures due to stratospheric ozone changes is different. For example, Marsh et al. (2016) did not find impacts of stratospheric ozone on the surface temperature. This arises that effect of stratospheric ozone on the surface temperature are model-dependent.

2.6.3 Impact of Ozone Changes on Zonal Winds

The ozone-caused temperature changes modify the meridional temperature gradient in the mid-latitudes of the lower stratosphere, which influences the zonal winds. Therefore, the effect of ozone on zonal wind in a 4xCO_2-experiment is shown in Figure 2.15.

The temperature response to ozone changes leads to a reduction of the meridional temperature gradient in the extra-tropical lower stratosphere (Chiodo and Polvani, 2019). This implies zonal

wind anomalies in the stratosphere that have the opposite sign of the anomalies caused by 4xCO_2. In the SH this weakening even extends down to the troposphere. In contrast, the zonal wind strengthens over the subtropical lower stratosphere, which also has an impact on the troposphere. According Chiodo and Polvani (2019), there is a damping of the CO_2-induced poleward shift of the EDJ through the ozone changes by 20 %.

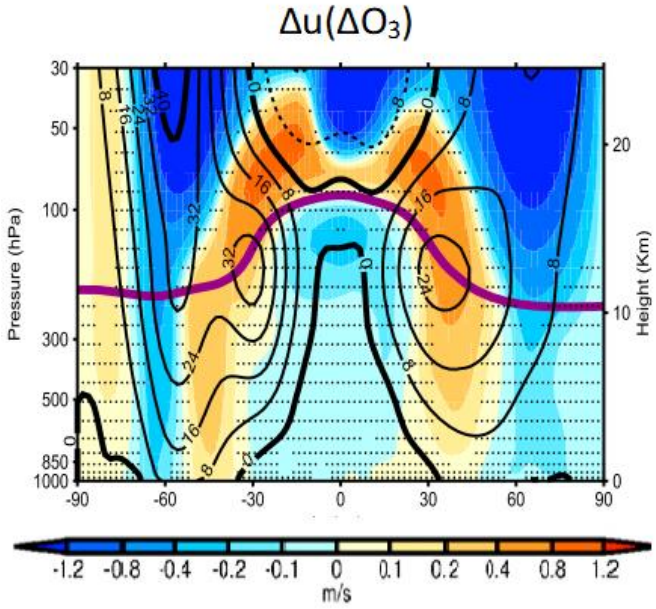

Figure 2.15 (from Chiodo and Polvani, 2019): Like Figure2.14, but for annual-mean zonal-mean zonal wind. Black contour lines depict the climatological zonal-mean zonal wind for pre-industrial conditions.

In the southern mid-latitudes the zonal wind changes are significant even at the surface. That indicates changes in the surface winds resulting in a reducing of the poleward shift of the surface westerlies. To see the impact of the surface wind change on the ocean dynamics, Figure 2.16 a) from Chiodo and Polvani (2017) represents the eastward surface wind stress response on 4xCO_2-simulation with a prescribed unchanged (preindustrial) ozone field (Figure 2.16 a) and the change in the 4xCO_2-simulation due to interactive ozone (Figure 2.16 b).

Figure 2.16 a illustrates a zonal symmetric dipole structure with increasing values south and decreasing values north of around 60°S, which means, the surface westerlies are shifted polewards by 4xCO_2. Figure 2.16 b, on the other side, shows an inverse pattern. This leads to the conclusion, that interactive ozone damps even the shift of the zonal wind stress at the surface by a magnitude of 0.003 – 0.005 Pa That impact on the surface wind stress could even influence the carbon uptake over the Southern Ocean (Marshall and Speer, 2012).

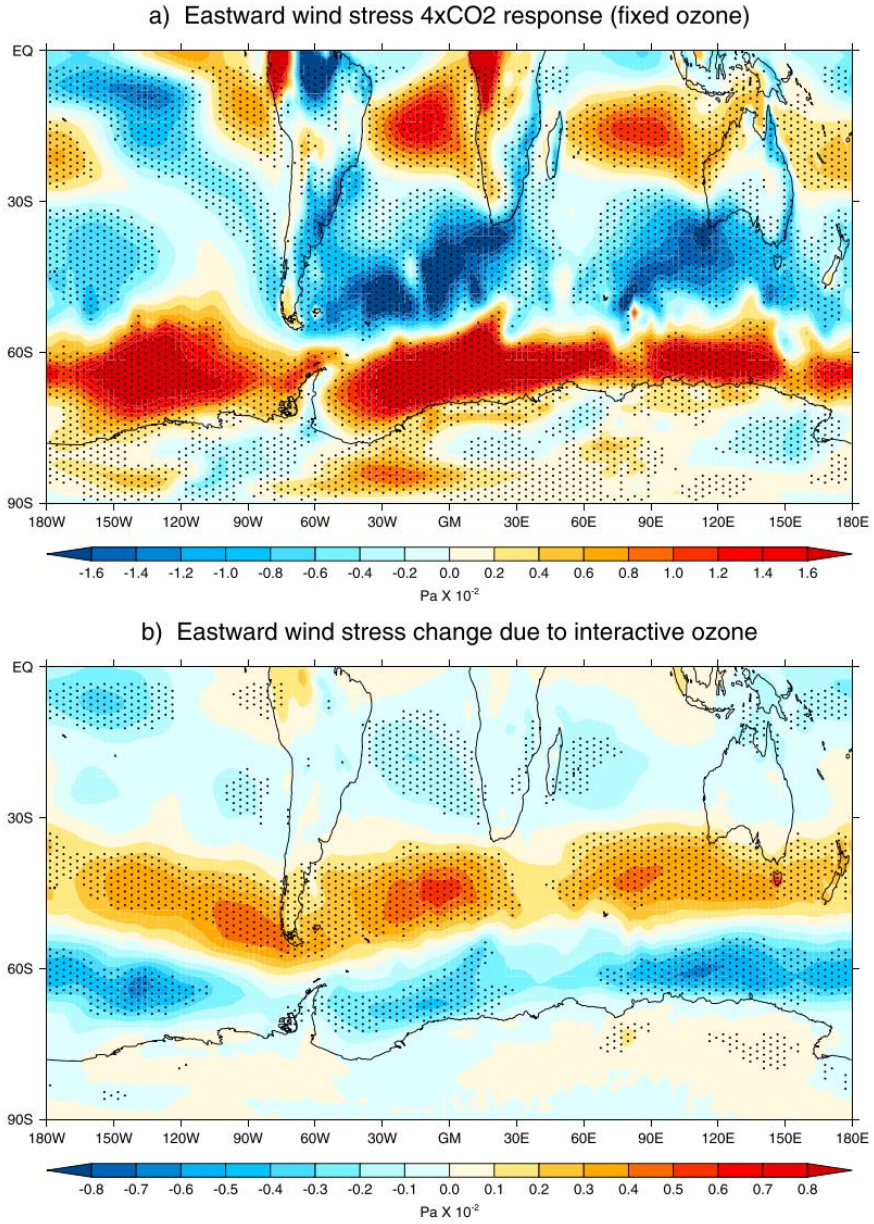

Figure 2.16 (from Chiodo and Polvani, 2017)**:** Annual mean eastward surface wind stress response to **a)** 4xCO_2 in integrations with fixed (climatological) ozone and of the **b)** change in eastward surface wind stress due to interactive ozone in 4xCO_2 integrations. Dotted areas identify the significant changes at the 99% confidence level. Units in Pa (x10^2).

3 Data und Methods

3.1 Model and Simulations

3.1.1 The ECHAM MESSy Atmospheric Chemistry (EMAC) Model

For the analyses output data of the ECHAM Modular Earth Submodel System (MESSy) Atmospheric Chemistry, v2.54.0.3 (EMAC, Jöckel et al. 2010, 2016) model in a T42L47MA are used. T42L47MA stands for a horizontal resolution of ~ 2.8° x 2.8° and 47 model layers in the vertical. The uppermost layer is located around 0.01 hPa and the middle atmospheric dynamics (MA) are resolved. The basic submodels for dynamics, clouds and diagnostics (namely, AEROPT, CLOUD, CLOUDOPT, CONVECT, CVTRANS, E5VDIFF, GWAVE, ORBIT, OROGW, PTRAC, QBO, SURFACE, TNUDGE, TROPOP, VAXTRA, see Jöckel et al., 2005, 2010, 2016 for more information on these submodels) are applied for this study. For radiation the FUBRAD scheme is used. This is a parametrization of high-resolution short-wave heating rate for solar variability studies. It replaces the default RAD radiation at wavelength most sensitive to solar radiation in the UV and visible spectrum between the model top and 70 hPa (Nissen et al., 2007; Dietmüller et al., 2016). Oxidation of methane by OH, $O(^1D)$, Cl and photolysis, the submodel CH4 is applied. Oxidation of methane is important for correctly simulating the specific humidity. It takes place mainly in the stratosphere (see Eichinger et al., 2015; Frank et al., 2018). The coefficients of the photolysis rate are calculated by the submodel JVAL, which uses cloud water content and cloudiness as well as prescribed ozone and aerosols (Sander et al., 2014). On the other hand, no (interactive) chemistry is activated in the simulations (see chapter 3.1.2 for more details). All submodels use the default EMAC settings (see Jöckel et al., 2005, 2010, 2016). The time step for the model runs was set to 720 s and the time interval for output data to 6 h.

Figure 3.1 from the official MESSy webpage (The Modular Earth Submodel System (MESSy) (messy-interface.org)), depicts schematically how the submodel layers interact with the base model layers. There are 4 layers in total which are displayed as colored crossbars.

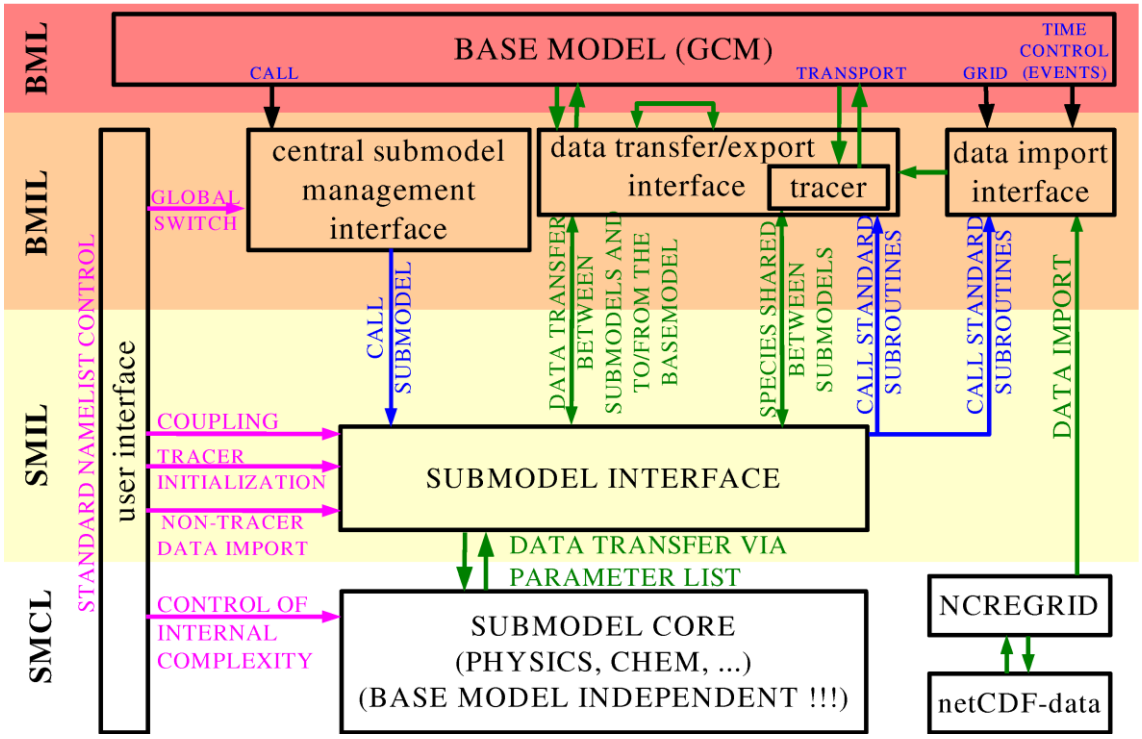

Figure 3.1 (from The Modular Earth Submodel System (MESSy) (messy-interface.org): Schematic illustration of the MESSy interface structure consisting of 4 layers (listed from top to bottom): The Base Model Layer (BML), the Base Model Interface Layer (BMIL), the Submodel Interfac Layer (SMIL) and the Submodel Core Layer (SMCL).

1. The Base Model Layer (BML) is at the top of Figure 3.1. It contains only a central time integration management as well as a control facility for the processes involved. In this work the base model ECHAM is used.

2. In the layer below the Base Model Interface Layer (BMIL) is located. It has three functionalities:

- The central submodel interface gives the base model the possibility to control the submodels.
- The data transfer/export interface is responsible for data transfer between the submodels and the base model and between different submodels. Moreover, this interface exports the results. There is a classification of the data to their use, e.g., as physical constant, as time varying physical fields, and as tracers (i.e. chemical compounds).
- The data import interface is needed for flexible (i.e. grid independent) import of gridded initial and time dependent boundary conditions.

The 2 layers at the bottom are the submodel interfaces which are compromised by the BMIL.

3. The Submodel Interface Layer (SMIL) is a submodel-specific interface, which collects relevant information/data from the BMIL, transfer them via parameter lists to the Submodel Core Layer (SMCL), calls the SMCL routines and distributes the calculated results from the

parameter lists back to the BMIL. In this layer the coupling/feedback between the submodels happens.

4. The Submodel Core Layer (SMCL) has self-consistent core routines of a submodel (e.g., chemical integration, physics, parametrizations, diagnostic calculations, etc.). These routines are completely independent of the implementation of the base model. The data transfer with the submodel interface is performed via parameter lists of the subroutines and the output data are completely dependent on the input data.

3.1.2 Simulations and Analysis Method

Simulations

With the above described EMAC model three different simulations were done which are listed in Table 3.1.

Simulation name	**CO_2**	**SSTs and SICs**	**O_3**
piCtrl	pi	Prescribed from CMIP6-piCtrl	Prescribed from CMIP6-piCtrl
4xCO_2Ctrl	4xCO_2	Prescribed from CMIP6-4xCO_2	Prescribed from CMIP6-4xCO_2
4xCO_2piO_3	4xCO_2	Prescribed from CMIP6-4xCO_2	Prescribed from CMIP6-piCtrl
CMIP6-piCtrl	pi	Interactive	Interactive
CMIP6-4xCO_2	4xCO_2	Interactive	Interactive

Table 3.1: Overview of the simulation setups for the pre-industrial control run (piCtrl), the 4-times CO_2 control run (4xCO_2Ctrl) and a 4-times CO_2 run with pre-industrial ozone concentrations (4xCO_2piO_3). The sea surface temperatures SSTs, sea ice concentrations SICs and the ozone concentrations (O_3) are prescribed by the EMAC pi-control and 4xCO_2Ctrl simulations, which were performed for the CMIP-6 project. These simulations are described in the last 2 rows.

It depicts 3 free-running time slice simulations, which are a pre-industrial control run (piCtrl), a 4-times CO_2 control run ($4xCO_2$Ctrl) and a 4-times CO_2 run with pre-industrial ozone concentrations ($4xCO_2piO_3$).

These prescribed ozone fields in units of molar mixing ratio for pre-industrial (pi) CO_2 conditions and for quadrupled CO_2 conditions are depicted in Figures 3.2 a and 3.2 b. Below, in Figure 3.2 c, the relative change of the ozone molar mixing ratio between the $4xCO_2$ und pi-condition is shown.

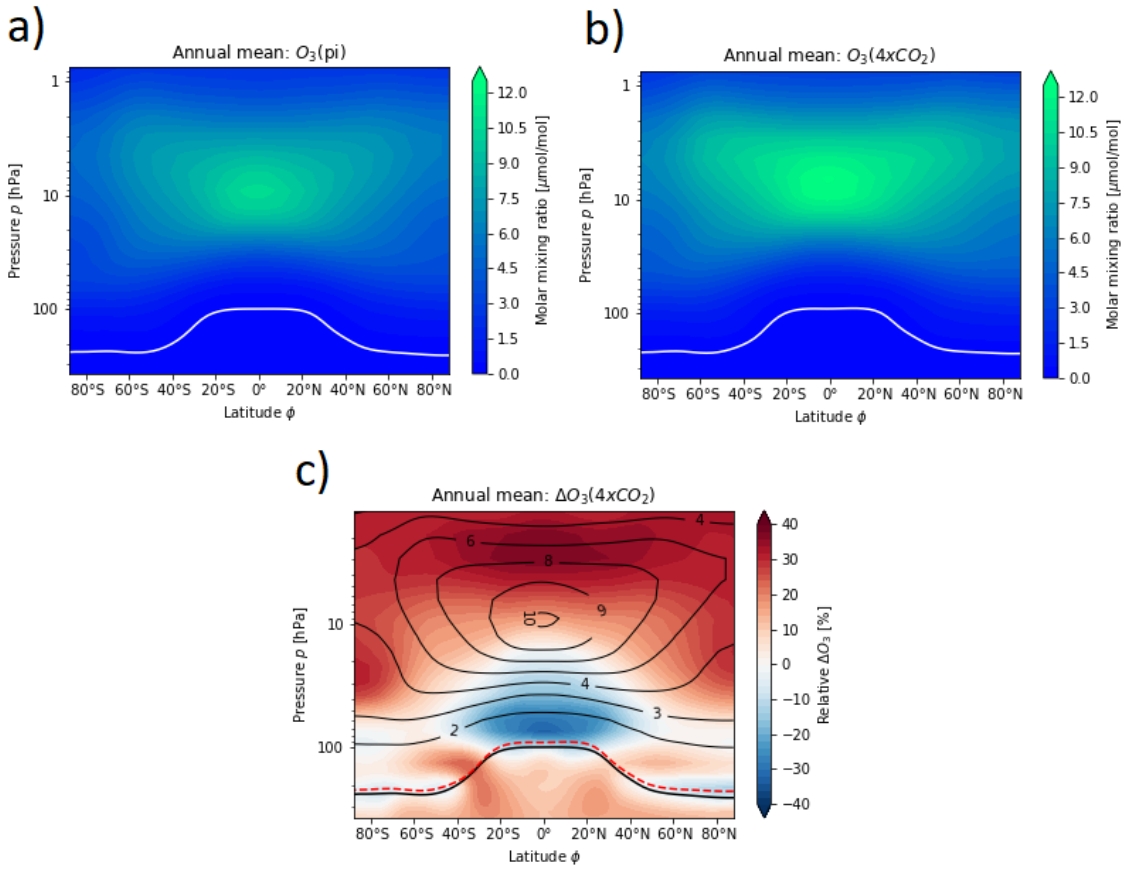

Figure 3.2: a) and **b)**: Prescribed ozone field used in this study for pre-industrial (pi) CO_2 conditions and for $4xCO_2$ conditions ($4xCO_2$). The white contour illustrates the tropopause for the specific condition.
c): Relative difference between **b)** and **a)** showing the relative response of $4xCO_2$ on the ozone field. Solid contours depict the molar mixing ratio of ozone for pi-conditions (colours). Black contour is the pi-tropopause and the red dashed contour is the $4xCO_2$-tropopause.

The highest molar mixing ratio of ozone is located in the tropical middle stratosphere (see Figures 3.2 a and b). Due to $4xCO_2$ the amount of ozone decreases in the lower tropical stratosphere and increase in the extra-tropical stratosphere and in the upper stratosphere, which is illustrated in Figure 3.2 c. This is in line with the studies by Dietmüller et al., 2014, Nowack et al., 2018 and Chiodo et al. 2016, 2018 and 2019. The reason for the change of the ozone field through $4xCO_2$ is explained in chapter 2.6.1.

The sea surface temperatures (SSTs) and sea ice concentrations (SICs) are prescribed by 30-year SST and SIC climatologies of the EMAC pi-control and 4xCO_2Ctrl simulations, which were performed for the CMIP-6 project. Ozone (O_3), N_2O and CFC fields are also prescribed by these simulations of the CMIP-6 project as zonal means in the radiation scheme. The OH, Cl and O(^{1}D) fields are prescribed to simulate methane oxidation in the CH4 submodel. CO_2 and methane (CH_4) are treated as tracers in the simulations, whose lower boundary conditions are prescribed with year 1850 conditions from the data sets that were also used in the historical CMIP-6 simulations. For the 4xCO_2 simulations, the CO_2 concentration of the lower boundary condition is quadrupled. The submodel QBO was taken in order to nudge the tropical zonal winds. For this purpose, the nudging field amplitude of $0.2 \cdot 10^{-6}$ was used, that leads to a nudging time of 60 days. The simulations were running over 60 years, whereas the first 10 years are considered as spin-up. Thus, the output data of the 50 years after the spin-up time were analyzed in this study.

Analysis Method

The results of these simulations are analyzed to investigate the impact of ozone changes, which are described in Figure 3.3.

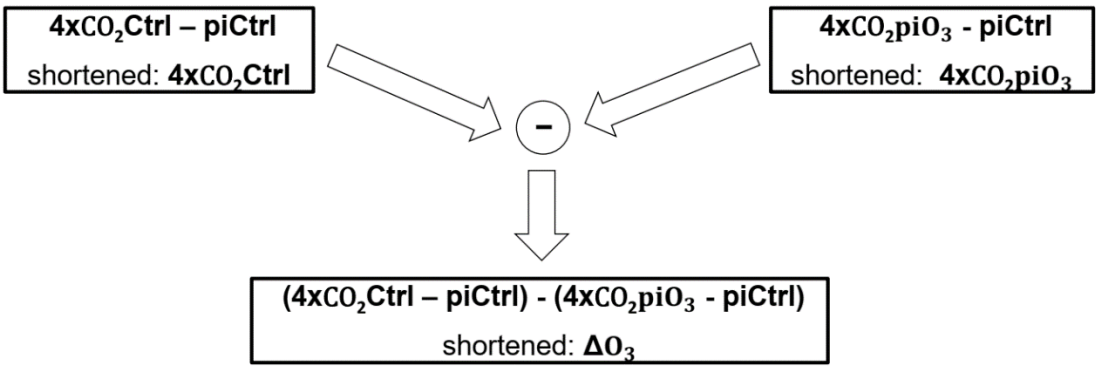

Figure 3.3: Schematic description of the analysis method: The difference between 4xCO_2Ctrl/4xCO_2piO_3 and piCtrl at the top shows the change due to 4xCO_2 with a prescribed ozone field from the 4xCO_2/pre-industrial CMIP-6 simulation. The difference of these 4xCO_2 differences ((4xCO_2Ctrl − piCtrl) − (4xCO_2piO_3 − piCtrl)) at the bottom state the effect due to CO_2-induced ozone changes.

The difference between the 4xCO_2Ctrl and the piCtrl simulation (Figure 3.3; upper left) gives the change due to 4xCO_2 with a prescribed ozone field from a 4xCO_2 CMIP-6 simulation. The change due to 4xCO_2 with a prescribed ozone field from a pre-industrial CO_2 simulation can be calculated by the difference between 4xCO_2piO_3 and piCtrl (Figure 3.3; upper right). The effect of the ozone

changes due to 4xCO_2 is calculated by the difference between the CO_2-simulations ((4xCO_2Ctrl − piCtrl) − (4xCO_2piO_3 − piCtrl); see bottom of Figure 3.3). This difference is used for all analyses, which regards the response on CO_2-induced ozone changes.

3.1.3 Comparison with CMIP-6 Simulations

In this study, experiments based on simulations with a prescribed ozone field are conducted. As a first test, if our simulations with prescribed ozone are consistent with results from a simulation with interactive chemistry, Figure 3.4 is shown. On the left side, the response of the zonal wind on 4xCO_2 is illustrated in the simulation with prescribed ozone field from a 4xCO_2-simulation for the mean over DJF (Figure 3.4 a) and for the mean over JJA (Figure 3.4 c). On the right side, the same analysis is depicted, but from the simulation with interactive chemistry and an interactively coupled ocean from CMIP6-simulations (see last row in table 3.1).

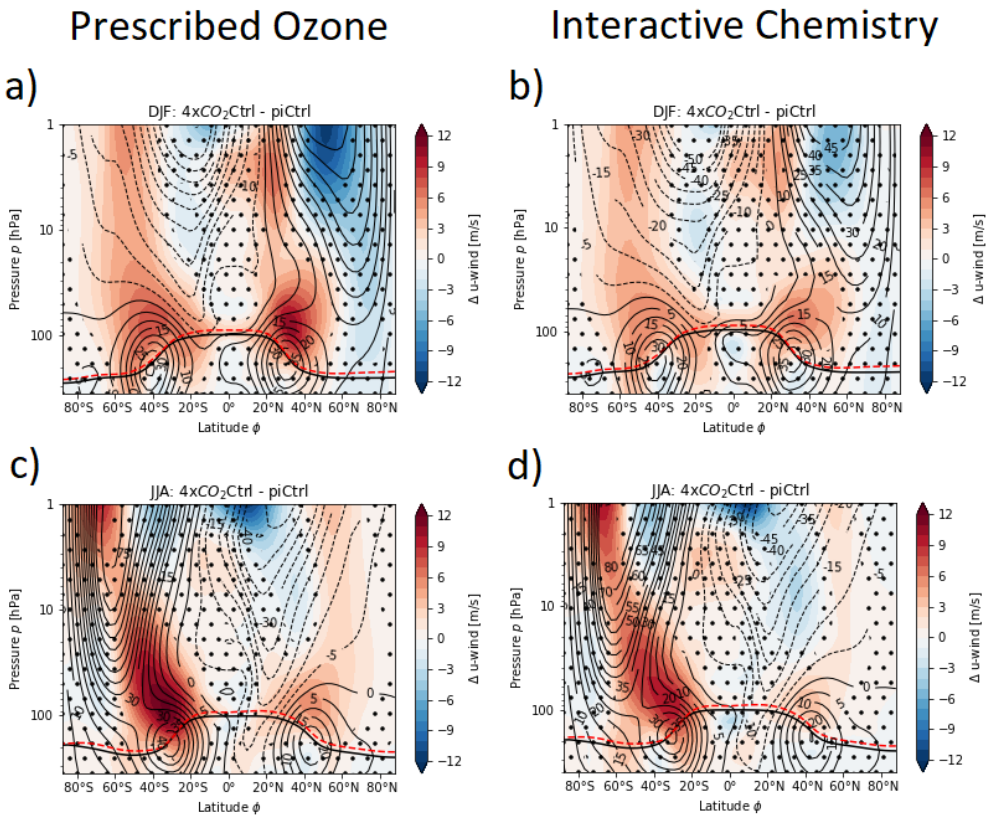

Figure 3.4: Left: Zonal mean zonal wind response on 4xCO_2 of a simulation with a prescribed ozone field for the mean over **a)** DJF and **c)** JJA.

Right: Zonal mean zonal wind response on 4xCO_2 of the CMIP-6 simulation with interactive chemistry for the mean over **b)** DJF and **d)** JJA.

The contours illustrate the zonal wind and the thick line the tropopause for pre-industrial (pi) CO_2 conditions. The dashed red line depicts the tropopause for 4xCO_2 conditions. Regions where the differences are outside of the 95 % confidence interval are stippled.

The comparison between the two simulations shows that the STJ is intensified and shifted upward due to the CO_2 increase in both simulations. Moreover, there is a displacement of the Antarctic polar vortex in the simulation with prescribed ozone as well as in the simulation with interactive chemistry. Nevertheless, in the simulation with interactive chemistry the weakening of the Arctic polar vortex is not significant in contrast to the simulation with prescribed ozone. This qualitative difference should be kept in mind in the analysis in chapter 4. Moreover, this difference cannot be interpreted as an effect of interactive ozone chemistry, because the prescribed ozone fields are taken from the CMIP-6 simulations, which use interactive chemistry. The CMIP-6 runs could not be used for our experimental purposes, because the setup cannot run with prescribed ozone. However, overall this first test shows that the simulations with prescribed ozone are well callable of simulating the general patterns of dynamic changes due to a CO_2 quadrupling.

3.2 Methods

3.2.1 Detection of Sudden Stratospheric Warmings (SSWs)

In chapter 2.4.3 the theoretical background of the polar vortex and the SSWs are discussed. There are different ways to identify SSWs or types of SSWs. This study differentiates the SSWs between major and minor events as well as between splitting and displacement events.

Major SSWs

For the identification of major SSWs the method from Charlton and Polvani (2007) is used, which takes the zonal mean zonal wind at 60° N/S and 10 hPa ($u_{zonal}(10hPa, 60°N/S)$) as an indicator. If this zonal mean zonal wind is negative (easterly) between November and March (NDJFM) in the NH, it is called a major SSW. For the SH the time between May and September (MJJAS) is used for the major warming analysis. The described criterion can be written as

$$u_{zonal}(10hPa, 60°N/S) < 0 \tag{3.1}$$

Additional to this condition, Charlton and Polvani (2007) define three more rules for detection of a major SSW:

1. Division in temporally close events:
   Between two major SSWs there have to be at least 20 days with westerly winds.
2. Exclusion of final warming events:
   The zonal mean zonal wind has to be westerly after each SSW for at least 10 days before 30 April.

The minimum duration of a major SSW was set at 10 days.

Minor SSWs

In addition to the major SSWs, the minor SSWs are detected as well. Minor SSWs are a weakened form of the major SSWs. According the WMO definition, a minor SSW happens, if the poleward gradient of the zonal mean temperature T_{zonal} between 60°N/S and 90°N/S is positive (see Equation 3.2).

$$T_{zonal}(10hPa, 90°N/S) - T_{zonal}(10hPa, 60°N/S) > 0 \quad (3.2)$$

However, in contrast to a major SSW, the zonal mean zonal wind at 60°N/S and 10 hPa must not switch from westerly to easterly during a minor SSW. Therefore, the number of major SSWs has to be subtracted of the number that is calculated with Equation 3.2. Moreover, the additional conditions defined by Charlton and Polvani (2007), which are described above, are applied for the detection of the minor SSWs as well.

Split and Displaced SSWs

For the classification of the SSWs, the spatial behavior is analyzed, too. As shortly explained in chapter 2.4.3, during a SSW, the polar vortex can split into two smaller vorticies, which is called a split event or the polar vortex can be displaced equatorward. The latter is named a displacement event. Seviour et al (2013) developed a method to detect these types of SSW events, which is used in this study. Here is a short receipt of the method:

1. The contour of the geopotential height at 10 hPa and 60°N/S is needed for the identification of the vortex region.

2. With this contour and the geopotential height field, the centroid latitude and the aspect ratio can be calculated following the method of Matthewman et al. (2009).
3. The separate detection of the events is done applying a threshold criterion: For a displaced event, there has to be a shift of the centroid latitude equatorward of 66°N/S for at least 7 days. Split events are identified, if the aspect ratio is higher than 2.4 for 7 days or more. Two events are not allowed to occur within 30 days.

In this study the minimum duration of a split or displacement event is changed to 10 days and the minimum time between two events is changed to 20 days. This modification of the thresholds is needed to be consistent with those of the method of major and minor SSW detection by Charlton and Polvani (2007). Moreover, the threshold for the centroid latitude is defined as the 5^{th} percentile of all centroid latitude. The threshold for the aspect ratio is the 95^{th} percentile of all aspect ratios. These variable thresholds are more general. Moreover, they are specified for each data set in comparison to those suggested by Seviour et al. (2013).

Final Warmings

In case of a SSW the zonal mean zonal wind flips from westerly to easterly for at least 10 days (Charlton and Polvani, 2007). In the case that the easterly wind does not recover to a westerly wind during the season, the stratospheric warming is called a final warming. This indicates that the polar vortex breaks down and the summer circulation, the stratospheric easterlies, evolves. In this analysis the final warming was detected similarly to the identification of the major SSWs by the method of Charlton and Polvani (2007). The only difference is that the minimum duration of the zonal mean easterlies ($u_{zonal}\left(10\text{hPa}, 60°\frac{\text{N}}{\text{S}}\right) < 0$) is set to 30 days. This threshold is chosen, because SSWs lasting 30 days or longer have not yet been observed.

3.2.2 EP Flux Scaling

EP fluxes represent the propagation of planetary and synoptic-scale waves as discussed in chapter 2.4.2. Thus, it is important to have a scaling of its components for the illustration of realistic EP flux strength with arrows. For the scaling of these arrows, the method described in Edmon et al. (1981) is applied. The components of the EP fluxes of the output data are given in spherical coordinates F_φ and F_p, where φ is latitude and p the pressure level. For scaling the EP fluxes to arrows, whose horizontal and vertical components are proportional to each other, the formulas

$$\hat{F}_{\varphi} = 2\pi r_0 g^{-1} cos\varphi F_{\varphi} \tag{3.3 a}$$

$$\hat{F}_{p} = 2\pi r_0^2 g^{-1} cos\varphi F_{p} (-80400\ Pa)^{-1} \tag{3.3 b}$$

are used similarly to Equation 3.13 in Edmon et al. (1981). The division through $-80400\ Pa$ in the vertical component is needed to get vertical and horizontal unit arrows with the same length. r_0 is the Earth's radius and g describes the gravitational acceleration. The unit of this quantity after the scaling is m^3.

3.2.3 Mass Streamfunction and Downward Control Principle

Mass Streamfunction

The mass streamfunction $\widehat{\Psi}$ is useful for the representation of the meridional circulation like the BDC (see chapter 2.4.4). The calculation of the mass streamfunction $\widehat{\Psi}$ is

$$\widehat{\Psi} = 2\pi r_0\, cos(\varphi)\, g^{-1} \int_p^0 \bar{v}^*\, dp\,. \tag{3.4}$$

In this Equation $\bar{v}^*$ stands for the zonal mean of the meridional residual velocity, which is calculated by the TEM equations (Equation 2.21 a and 2.21 b).

Downward Control Principle

In chapter 2.4.2, the theory behind the Downward Control principle was introduced. This theory says that the vertical velocity at the height z is generated by the wave forcing above that height (Haynes, 1991). In summary, the wave forcing drives the RMOC, which is expressed by the streamfunction Ψ. Therefore, mathematically the streamfunction Ψ is proportional to the zonal wave forcing $\bar{F}$ described in Equation 2.24 in chapter 2.4.2 from Okamoto et al. (2011). That Equation is used for this study.

However, Equation (2.24) does not yield the mass streamfunction $\hat{\Psi}$. For the transformation, a multiplication of the streamfunction from Equation (2.24) with the factor $2\pi r_0 g^{-1}$ is needed.

3.2.4 Mean Age of Air (AoA)

As mentioned in chapter 2.4.4, the AoA cannot be measured directly. The AoA in units of time has to be derived from tracer measurements. The AoA timescale corresponds to the time lag between the stratospheric concentration and that at the tropical Earth's surface. This was mathematically formulated by Hall and Plumb (1994), who defined an AoA, which is species-independent. They defined a parcel as a mix of air that consist of different species with a range of transit times. The mean of these transit times is the AoA. The time range is a type of Green's function *G* that is a boundary propagator.

The AoA will be derived to show how it is calculated in units of time of a conserved tracer's mixing ratio χ. Thus, the connection of the mixing ratio of χ at time t and point in the stratosphere *r* with *G* is given by

$$\chi(r,t) = \int_{-\infty}^{t} \chi(\Omega,t')G(r,t|\Omega,t')dt', \tag{3.5}$$

where Ω is the boundary source region, which was selected to be the tropical Earth's surface between 10° N and 10° S and t' refers to the time when the tracer last had contact with Ω. Under the assumption that $\chi(\Omega,t)$ is equal to a Dirac delta function $\chi(\Omega,t) = \delta(t-t')$, the mixing ratio χ can be formulated as $\chi(\Omega,t) = G(r,\Omega,t-t')$ with

$$\int_0^{\infty} \mathrm{G(r,\Omega,t)dt} = 1 \tag{3.6}$$

The elapsed time is defined as $\xi = t - t'$ and τ the concentration lag time, which is the elapsed time between the mixing ratio χ at Ω and at *r*. This means that the conserved air parcel has a mixing ratio $\chi(r,t) = \chi(\Omega,t-\tau)$ and a mass fraction $G(r,t|\Omega,t-\xi)$. Under the assumption that a linear tracer is used, substituting $\chi(\Omega,t) \propto t$ into Equation 3.6 and averaging over the transit times yields the first order of the age spectrum, i.e. the AoA Γ (Hall and Plumb, 1994):

$$\Gamma(r) \equiv \tau(r) = \int_0^\infty \xi \cdot G\,(r|\Omega, \xi) d\xi \tag{3.7}$$

3.2.5 Detection of the Eddy-Driven Jet (EDJ) position

Theoretically, the latitude φ with the highest zonal wind speed at 850 hPa ($u_{max,850}$) in the mid-latitudes is the location of the EDJ. At this latitude, the first derivative of the zonal mean zonal wind at 850 hPa ($\frac{\partial u_{850}}{\partial \varphi}$) is equal to zero. Therefore, the latitude of $u_{max,850}$ is detected by an interpolation to the latitude, where $\frac{\partial u_{850}}{\partial \varphi} = 0$.

4 Results

In this chapter, each analysis that shows a latitude-height cross-section is structured as follows. First, the effects produced by a quadrupling of CO_2 concentrations are depicted, including the responses due to the accompanying ozone change. This analysis is called $4xCO_2$Ctrl. After that, the effects that arise only from the CO_2-induced ozone changes are illustrated, which is denoted by ΔO_3. This approach is intended to assess the contributions of the ozone effect in $4xCO_2$ simulations.

4.1 Thermal Influences of Ozone Changes

4.1.1 Radiative Heating Rates

Shortwave Radiative Heating Rates

As discussed in chapter 2.2, ozone absorbs and emits shortwave and longwave radiation, which modifies the temperature structure. Therefore, a change in the ozone field due to CO_2 has an effect on the radiative heating rates. Figure 4.1 depicts the response of the shortwave heating rates on $4xCO_2$Ctrl (see Figures 4.1 a and b) and on ΔO_3 (see Figures 4.1 c and d). Each response is calculated for the climatological mean over JJA (left) and over DJF (right). The contours illustrate the heating rates for pre-industrial CO_2 conditions.

A positive change of the shortwave heating can be seen in the upper tropical stratosphere and extra-tropical stratosphere and mesosphere of the summer hemisphere in the $4xCO_2$Ctrl-Analyses (Figures 4.1 a and b). Moreover, the shortwave heating slightly decreases in the tropical lower stratosphere. In the chapters 2.6 and 3.1, it was shown, that the amount of ozone increases in the upper tropical stratosphere and extra-tropical stratosphere and decreases in the lower tropical stratosphere through $4xCO_2$. In the latitudes, where solar radiation reaches the stratosphere, a higher/lower amount of ozone absorbs more/less solar radiation, which increases/decreases the ozone-induced shortwave heating in these regions. CO_2 does not absorb radiation in the shortwave spectrum. Therefore, the modification of the shortwave heating rates due $4xCO_2$Ctrl are mainly caused by ΔO_3, which explains the similarity between the shortwave heating responses of $4xCO_2$Ctrl (Figures 4.1 a and b) and ΔO_3 (Figures 4.1 c and d).

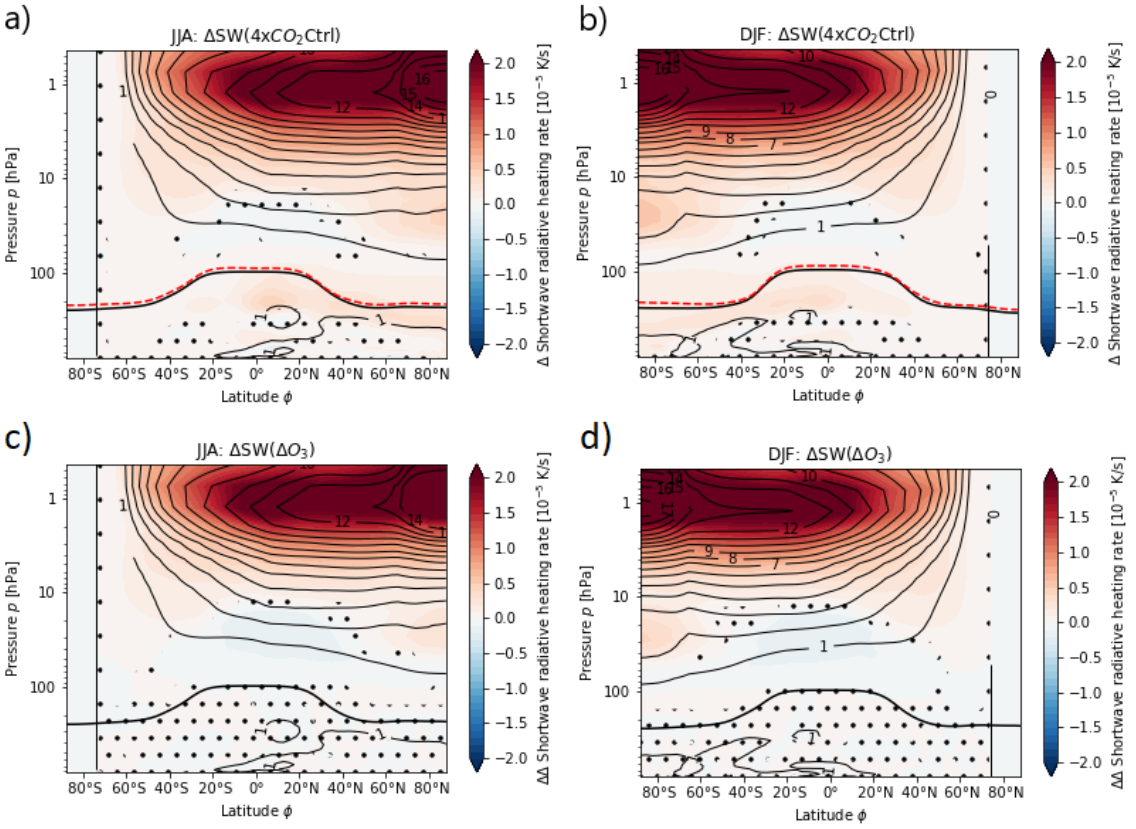

Figure 4.1: Latitude-height cross-section of the zonal-mean shortwave radiative heating response (colours) on 4xCO_2Ctrl (**a** and **b**) and on ΔO_3 (**c** and **d**) for the mean over JJA (**left**) and DJF (**right**). The black thick line illustrates the tropopause and the contours depict the shortwave radiative heating rate in 10^{-5} K/s for pre-industrial CO_2-conditions. The red dashed line is the tropopause for 4xCO_2-conditions. Non-significant responses at the 95 % confidence level are stippled.

Longwave Radiative Heating Rates

Emission of radiation in the atmosphere happens in the longwave spectrum. Therefore, the response of the longwave radiative heating on 4xCO_2Ctrl (Figures 4.2 a and b) and on ΔO_3 (Figures 4.2 c and d) is analyzed for JJA and DJF.

The increasing amount of CO_2 in 4xCO_2Ctrl leads to longwave radiative cooling in most parts of the stratosphere and lower mesosphere. Only in the tropical lower stratosphere and polar lower winter stratosphere longwave radiative heating happens. Nevertheless, the global longwave cooling due to an increase of CO_2 is in line with the theory that an increase of this greenhouse gas decreases the absorption of terrestrial radiation in the stratosphere (see chapter 2.2.2).

The largest longwave cooling response is located in the upper stratospheric and mesospheric tropics and summer hemisphere (for 4xCO_2Ctrl and ΔO_3). This is where also the highest positive shortwave heating differences exist (see Figure 4.1). In the lower tropical stratosphere, longwave heating and shortwave cooling occurs (see Figure

4.1). This is in line with the thermal balance (shortwave heating/cooling ≈ longwave heating/cooling) explained in Häckel (2021). Moreover, the strong longwave heating change in the upper stratosphere and lower mesosphere does not differ much between $4xCO_2Ctrl$ and ΔO_3. This is a hint that the longwave heating in this area is sensitive to ozone changes.

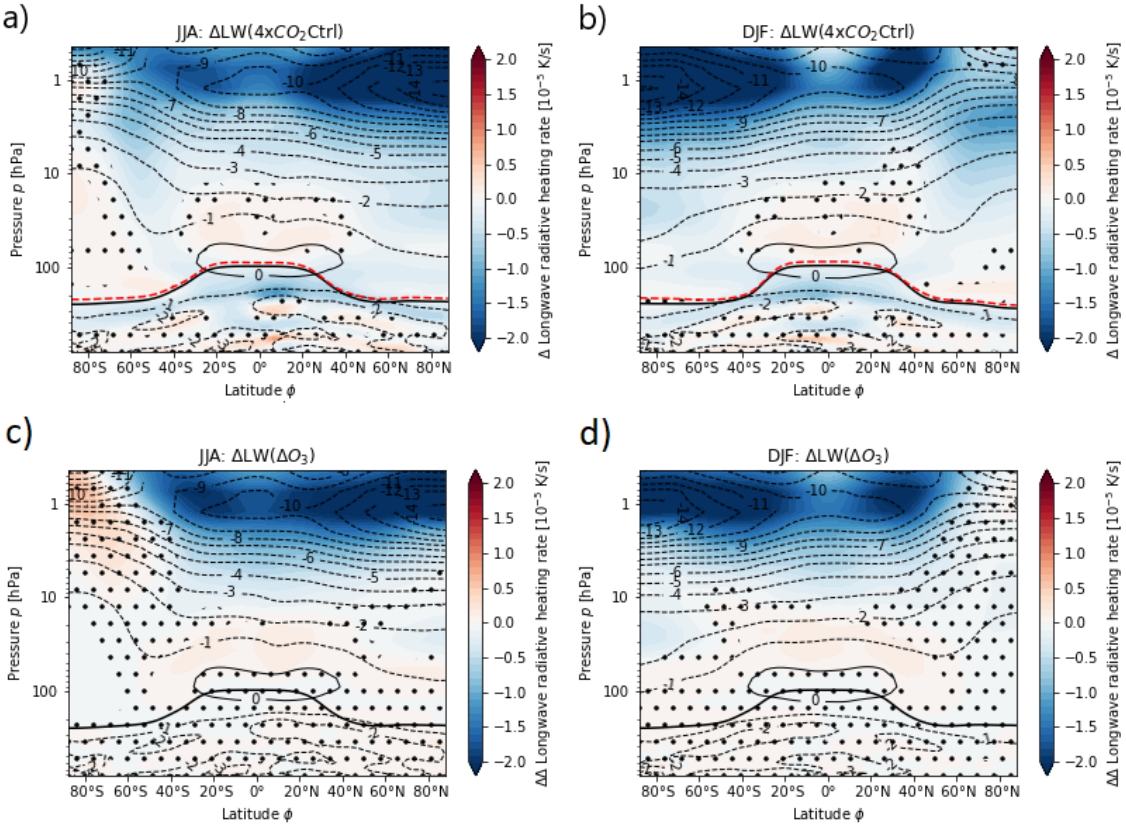

Figure 4.2: Latitude-height cross-section of the zonal-mean longwave radiative heating response (colours) on $4xCO_2Ctrl$ (**a** and **b**) and on ΔO_3 (**c** and **d**) for the mean over JJA (**left**) and DJF, (**right**). The black thick line illustrates the tropopause and the contours depict the longwave radiative heating rate in 10^{-5} K/s for pre-industrial CO_2-conditions. The red dashed line is the tropopause for $4xCO_2$-conditions. Non-significant responses at the 95 % confidence level are stippled.

4.1.2 Temperature

The above shown radiative heating plus some dynamical heating modifies the temperature fields. Figure 4.3 illustrates the resulting temperature response on $4xCO_2Ctrl$ (Figures 4.3 a and b) and on ΔO_3 (Figures 4.3 c and d) as latitude-height cross-section for JJA and DJF. The contours represent the zonal-mean temperatures for pre-industrial CO_2-conditions.

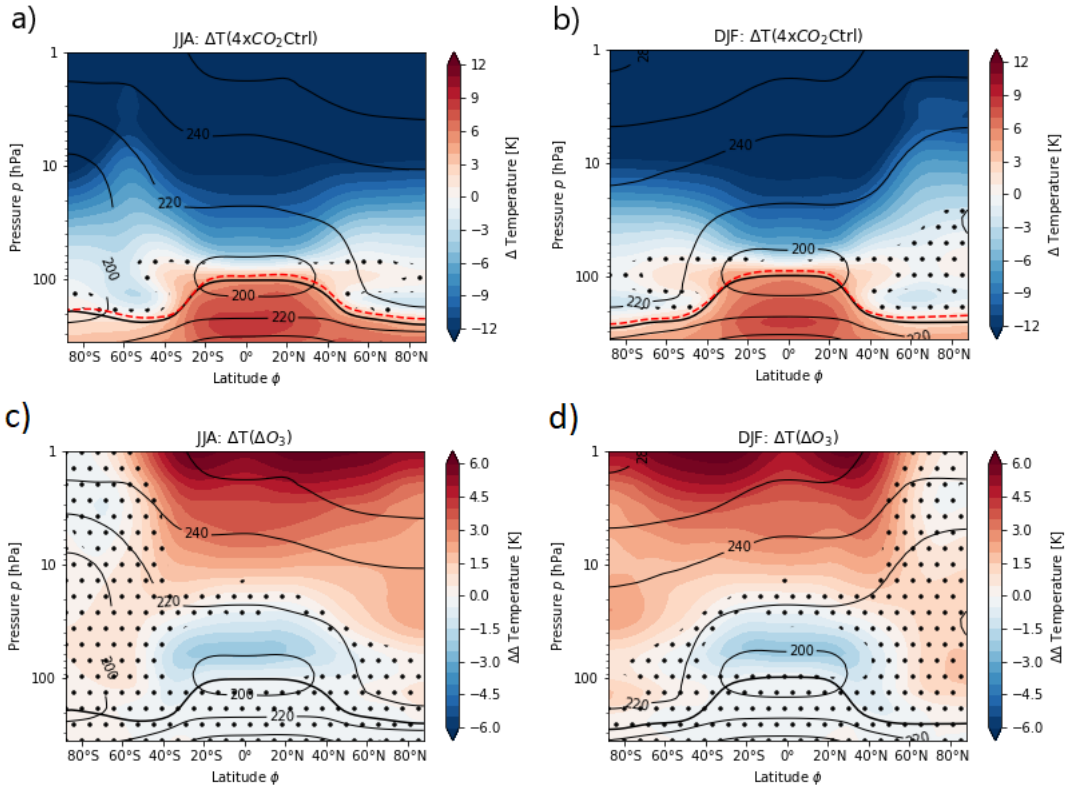

Figure 4.3*:* Latitude-height cross-section of the zonal-mean temperature response (colours) on 4xCO_2Ctrl (**a** and **b**) and on ΔO_3 (**c** and **d**) for the mean over JJA (**left**) and DJF (**right**). The black thick line illustrates the tropopause and the contours depict the temperature for pre-industrial CO_2-conditions. The red dashed line is the tropopause for 4xCO_2-conditions. Non-significant responses at the 95 % confidence level are stippled.

In 4xCO_2Ctrl the troposphere warms and the stratosphere cools. In chapter 2.2.2, it was explained that a higher amount of CO_2 absorbs more terrestrial radiation in the troposphere, which leads to a warming. Due to higher absorption of terrestrial radiation in the troposphere, less of this radiation reaches the stratosphere. Therefore, the stratosphere cools through 4xCO_2Ctrl by more than 12 Kelvin, which is in line with Jonsson et al., 2004, Sigmond et al., 2004; Fomichev et al., 2007.

Now the temperature effect through ΔO_3 (Figures 4.3 c and d) will be analyzed. In the upper stratosphere, the strongest temperature increase of about 3 to 5 Kelvin takes place in the tropics and in the extra-tropical summer hemisphere, which is in line with the shortwave heating response (see Figures 4.1 c and d). There are also robust effects on the temperature in the lower stratosphere. In the tropical lower stratosphere, the temperature decreases by about 2 Kelvin through a decrease of the amount of ozone. However, also stronger upwelling and changes in specific humidity can influence these temperature changes. This will be discussed in the following chapters. In the middle stratosphere over the polar cap the temperatures increase in summer by 2 Kelvin. These temperature changes are similar to those described in the studies by Chiodo and

Polvani (2019) and Nowack et al. (2015). Over the Antarctica the temperature increase in summer is even significant in the lowermost stratosphere.

4.2 Dynamical Influences of Ozone Changes

4.2.1 Zonal Winds

The change of the meridional temperature structure influences the thermal wind balance. Therefore, the influence of 4xCO_2Ctrl and ΔO_3 on the zonal-mean zonal wind will be shown next. Figure 4.4 shows these influences on the zonal wind in the upper troposphere and the whole stratosphere as a latitude-height cross-section for DJF and JJA. The thin contours represent the wind for pre-industrial CO_2-conditions.

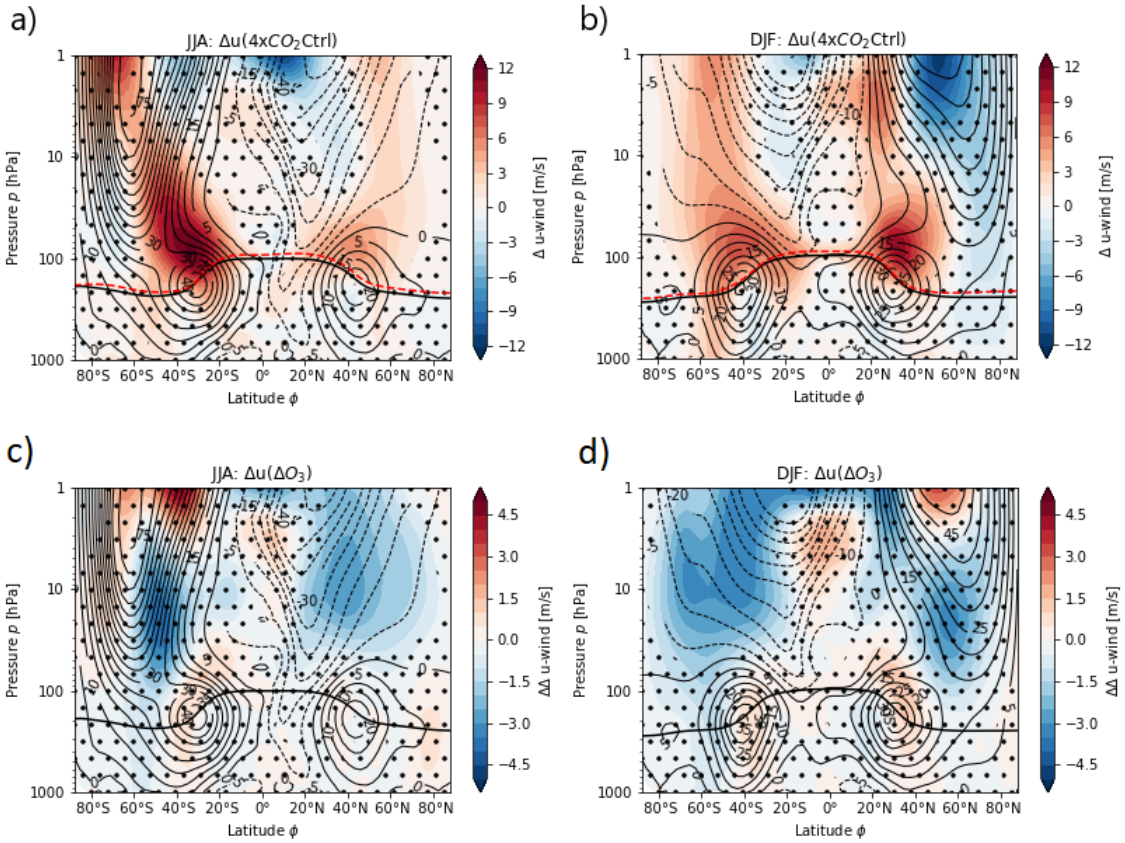

Figure 4.4*:* Latitude-height cross-sections of the zonal-mean zonal wind response (colours) on 4xCO_2Ctrl (**a** and **b**) and on ΔO_3 (**c** and **d**) for the mean over JJA (**left**) and DJF (**right**). The black thick line illustrates the tropopause and the contours depict the temperature for pre-industrial CO_2-conditions. The red dashed line is the tropopause for 4xCO_2-conditions. Non-significant responses at the 95 % confidence level are stippled.

The higher amount of CO_2 strengthens in 4xCO_2Ctrl the STJ by more than 10 m/s and lifts it up (Figures 4.4 a and b), which is consistent with the study of Chiodo and Polvani (2019). The reason

for this is the enhancement of the meridional temperature gradient below. Another statistically significant effect due to 4xCO_2 in the summer stratosphere is that the easterlies are decelerated. This is probably generated by shortwave radiative cooling of the tropical lower stratosphere and warming of the lower extra-tropical stratosphere in summer (see Figure 4.2 a and b), which weakens the stratospheric easterlies by thermal wind balance. However, the temperature response in the 4xCO_2Ctrl does not only show the radiative effect of CO_2 itself. Dynamical heating can also be the cause for this change of the temperature.
The Antarctic polar vortex accelerated through an increase of CO_2, which is in balance with a strengthening of the meridional temperature gradient in the lower stratosphere in the austral winter hemisphere (see Figure 4.3 a). The polar vortex in the Arctic weakens, which is in line with the trends that are described in the study of Garfinkel et al. (2017), Seviour (2017) and Kretschmer (2018). The reason for the slowdown is not yet fully understood.
There are also changes in the troposphere. The austral EDJ is shifted towards the pole, which is in line with the study of Chiodo and Polvani (2019). Especially in summer. This is possibly linked to the positive change of the zonal wind in the stratosphere above, because weakening of the stratospheric easterlies extends down to the troposphere.

The ozone changes through 4xCO_2 (ΔO_3, see Figures 4.4 c and d) influence the zonal wind as well, because it modifies the zonal wind in the stratosphere of the summer hemisphere. There, the easterlies in the middle and upper stratosphere accelerate by a maximum of 3 m/s. The stronger easterlies are the result of the increased meridional temperature gradient in the lower stratosphere in summer due to ozone, which is also consistent with the results of Chiodo and Polvani (2019). This might be a hint for an earlier polar vortex breakdown. The polar vortex itself, i.e. the zonal winds in the respective winter hemisphere shows only a non-significant attenuation. Moreover, the changes of the stratospheric easterlies in the SH extend down to the poleward flank of the EDJ. The negative but not statistically significant change of the zonal wind of the poleward EDJ flank can be a hint for a weakening of the poleward EDJ shift in 4xCO_2Ctrl. Therefore, a diagnostic of the EDJ position is done in chapter 4.2.4.

4.2.2 Polar Vortex

Seasonal cycle

To analyze the vortex strength and breakup date, the climatological zonal mean zonal wind of 60°N/S and at 10 hPa will be diagnosed next. This is a common used method for polar vortex diagnostics (see e.g. Charlton and Polvani, 2007 and Baldwin et al., 2021). Figures 4.5 a) and c) show the climatological mean of the zonal wind for the three simulations (piCtrl, 4xCO_2Ctrl and

$4xCO_2piO_3$) and the standard deviation (blue shading) for the $4xCO_2$Ctrl-simulation. 0 m/s is the threshold for the polar vortex formation or breakdown. If the curve is above this threshold, there is a polar vortex, if it is below a polar vortex does not exist.

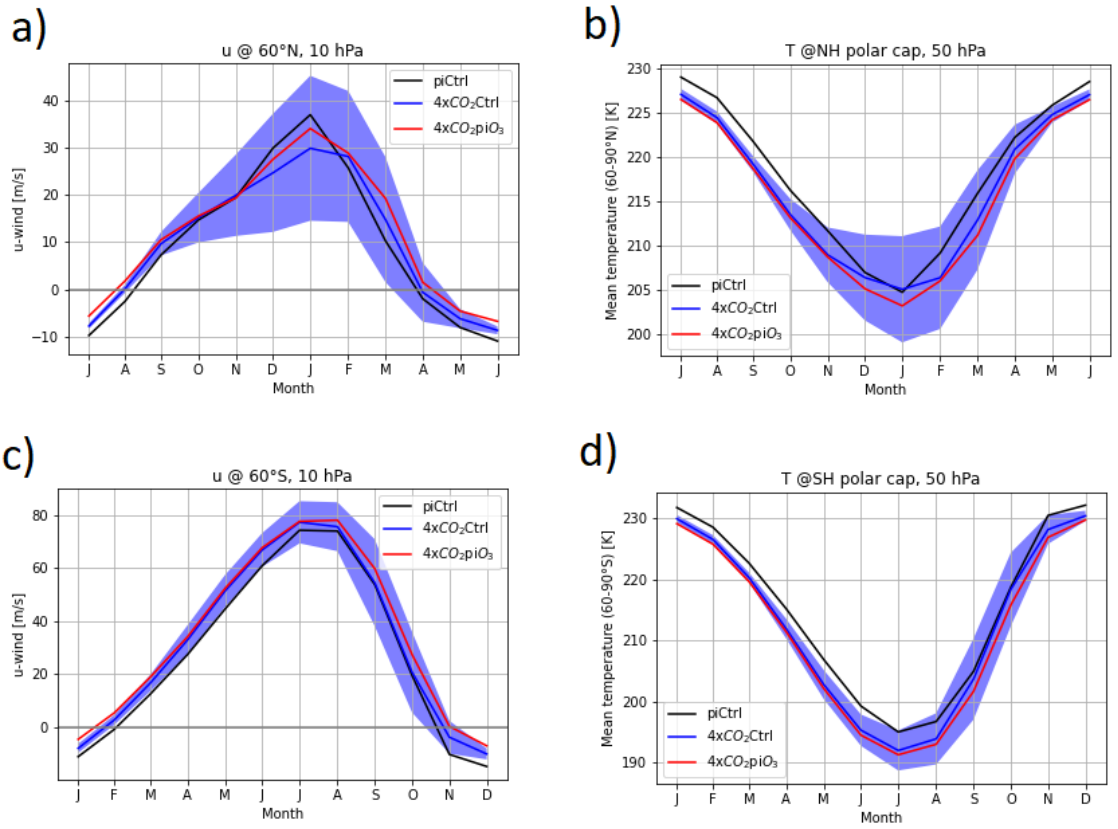

Figure 4.5: **Left**: Climatological zonal mean zonal wind at **a)** 60°N and 10hPa **c)** 60°S and 10hPa for the piCtrl- (black), $4xCO_2$Ctrl- (blue) and $4xCO_2piO_3$-simulations (red) in m/s. **Right**: Climatological mean of the temperature over the **b)** northern polar cap (60° - 90°N) and **d)** southern polar cap (60° - 90°S) at 50 hPa for the piCtrl- (black), $4xCO_2$Ctrl- (blue) and $4xCO_2piO_3$-simulations (red) in Kelvin. The standard deviation of the $4xCO_2$Ctrl-simulation is shown as blue shading.

For pre-industrial conditions (piCtrl) the polar vortex turns westerly early August in the NH and mid of March in the SH. The climatological breakdown takes place end of March in the NH and end of October in the SH. In the $4xCO_2$-simulations ($4xCO_2$Ctrl and $4xCO_2piO_3$) the polar vortex formation is earlier and the breakdown is later, which is in line with the study from Ayarzagüena et al. (2020). This means that the period of the polar vortex is longer due to an increase of CO_2. Moreover, the SH polar vortex is systematically stronger in the $4xCO_2$ simulations. The NH vortex is only systematically enhanced at the beginning and at the end of the period (August until September and February until April).

For the discussion of the ozone effects, $4xCO_2$Ctrl and $4xCO_2piO_3$ will be compared. In the NH the polar vortex is systematically weaker in $4xCO_2$Ctrl (see Figure 4.5a), except for October.

However, the year-to-year variability (blue shading) is larger than the differences between the 4xCO_2-simulations. In the 4xCO_2Ctrl simulation, the polar vortex builds up later and breaks down earlier than in the 4xCO_2piO_3 simulation. During the summer months, the easterlies are stronger due to ΔO_3, which was already shown in Figures 4.5 c) and d). As the vortex build up differences are beyond the variability, this effect can be considered to be robust.

To study the connection of the polar vortex changes to radiative heating, Figure 4.5 b) and d) illustrate the spatially averaged temperatures over the northern (see Figure 4.5 b)) and southern polar cap (see Figure 4.5 c)) at 50 hPa for the three simulations.

The systematic strengthening of the stratospheric easterlies by CO_2-induced ozone changes is in line with a systematic decrease of the polar cap due to shortwave heating in the lower stratosphere during the summer months. In both hemispheres, the weakening of the CO_2-induced zonal wind effects by ozone changes even continue until early winter. This means, that in the SH the ozone-induced shortwave heating of the summer polar stratosphere, weakens the polar vortex in early winter. Moreover, the weakening of the CO_2-induced polar vortex acceleration by ozone is affected by a shortwave cooling of the lower tropical stratosphere (see Figure 4.1 c and d)

Figures 4.5 a and c show that the CO_2-increase leads to a later final warming and the CO_2-induced ozone changes lead to an earlier final warming. To investigate, if these shifts of the final warming dates are robust, the distribution of the final warming dates of each simulation will be compared next.

Distribution of the Final Warming Dates

Figure 4.5 indicates that an increase of CO_2 leads to a later and the ozone changes lead to an earlier vortex breakdown, which is also known as a final warming, marking the end of the vortex season. To have a closer look at the comparison of final warming date between the piCtrl- and the 4xCO_2Ctrl-simulation and between the two 4xCO_2-simulations, a distribution of the final warming dates of all simulation years is conducted. The result of this analysis for the NH and SH is depicted in Figure 4.6. The dashed grey lines indicate the 25^{th} and 75^{th} percentile. The solid grey lines mark the median. The detection of the final warming date was done with the method of Charlton and Polvani (2007), which is described in chapter 3.2.1.

Quadrupling of the CO_2-concentration postpones the climatologically averaged final warming in the NH by 4 days. Figure 4.6 a) illustrates that the final warming date distribution in this hemisphere is shifted to later days, if the amount of CO_2 in the simulation is higher. In the SH, a shift in the final warming to a later date is also evident. Climatologically the final warming takes

place 8 days later in 4xCO_2Ctrl. Moreover, the median of the 4xCO_2Ctrl-distribution is equal to the 75th percentile of the piCtrl-distribution showing a statistical robustness of the delayed vortex breakdown in the SH.

Now the ozone effect on the final warming dates will be discussed. In comparison to the 4xCO_2piO_3-simulation, in the 4xCO_2Ctrl-simulation the distribution is shifted to earlier dates in both hemispheres. In the climatological mean, the final warming is 5 days earlier in the NH and even 7 days earlier in the SH (see Figures 4.6 c and d). In other words, without ozone changes through 4xCO_2, the effect on the final warming dates in a 4xCO_2-simulation would be two times larger.

In the SH, the 75th percentile of the distribution in the simulation with changed ozone (4xCO_2Ctrl) is equal to the median of the distribution in the simulation with unchanged (pre-industrial) ozone (4xCO2piO3, see Figure 4.6 d). This is an indication, that the shift of the final warming dates to an earlier day is robust in the SH.

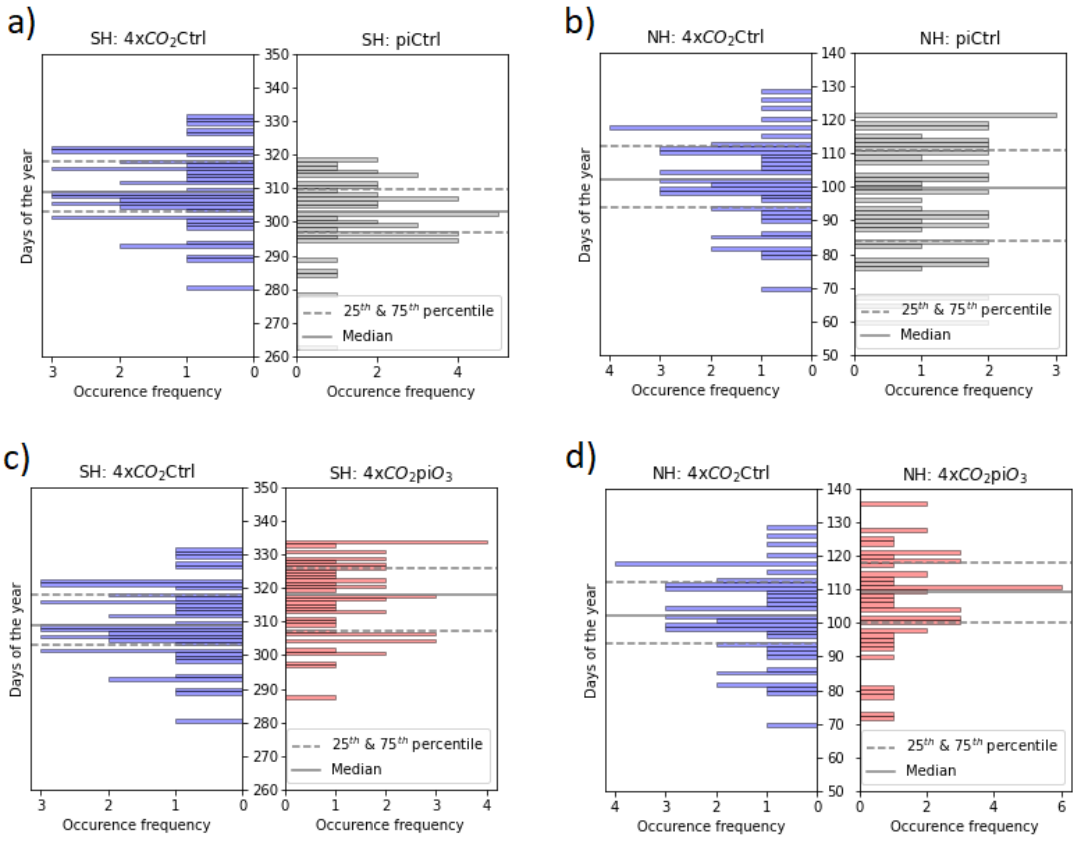

Figure 4.6: Comparison of the distribution of the stratospheric final warming dates between the piCtrl- and 4xCO_2Ctrl-simulation (**a** and **b**) and between the 4xCO_2Ctrl- and 4xCO_2piO_3-simulation (**c** and **d)**. The grey dashed lines depict the 25th and 75th percentile. The grey solid lines denote the median.

Now, it will be investigated if the abruptness of the final warming change as well. Therefore, the response of the geopotential height anomaly relative to the final warming date (Z_{ano}^{fw}) on 4xCO_2Ctrl (see Figures 4.7 a and b) and on ΔO_3 (see Figures 4.7 c and d) will be analyzed next. In Figure 4.7 the contours represent Z_{ano}^{fw} for pre-industrial conditions and coloured shading depicts the responses.

Figure 4.7 a shows that Z_{ano}^{fw} over the southern polar cap increases before the final warmig date and decreases afterwards, if there is a quadrupling of the CO_2 concentration. A comparison with the pre-industrial Z_{ano}^{fw} leads to the assumption that the temporal gradient of Z_{ano}^{fw} is weakened by 4xCO_2Ctrl. However, this result has to carefully regarded, because the changes of Z_{ano}^{fw} due to 4xCO_2 are not significant (Figures 4.7 a and b).

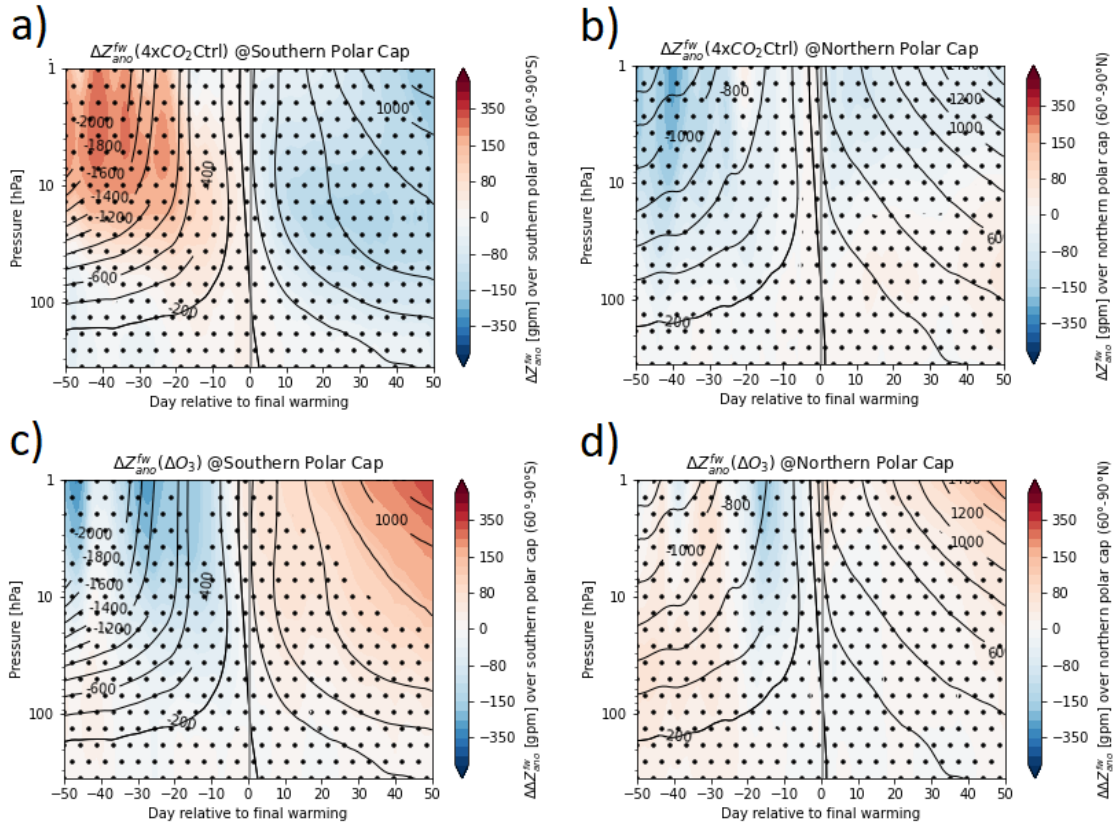

Figure 4.7: Response of the geopotential height anomaly relative to the final warming date (Z_{ano}^{fw}, colours) on 4xCO_2Ctrl (**a** and **b**) and on the ozone changes due to 4xCO_2 (**c** and **d**). The responses are illustrated for the southern polar cap (**left**) and northern polar cap (**right**) as a function of pressure and the day relative to final warming. Black contours depict the anomaly of Z_{ano}^{fw} relative to the final warming date for pre-industrial conditions in meter Non-significant responses at the 95 % confidence level are stippled.

In contrast to this, there is a significant response of Z_{ano}^{fw} on ΔO_3 (Figures 4.7 c and d). Due to CO_2-induced ozone changes, the upper and middle stratosphere heats after the final warming which is consistent with the significant heating of the polar stratosphere in summer due to ΔO_3 analyzed in chapter 4.1.2. In the days before the final warming the change of Z_{ano}^{fw} in the stratosphere is negative in ΔO_3, especially over the southern polar cap. As a result, the cooling before the final warming takes place and the warming afterwards leads to an enhanced temporal Z_{ano}^{fw} gradient in the stratosphere and thus results in a more abrupt final warming.

A diagnostic of Z_{ano}^{fw} for the piCtrl-, 4xCO_2Ctrl- and 4xCO_2piO_3-simulation at 10 hPa for the two polar caps should illustrate this abruptness and strength of the final warming more clearly (Figure 4.8).

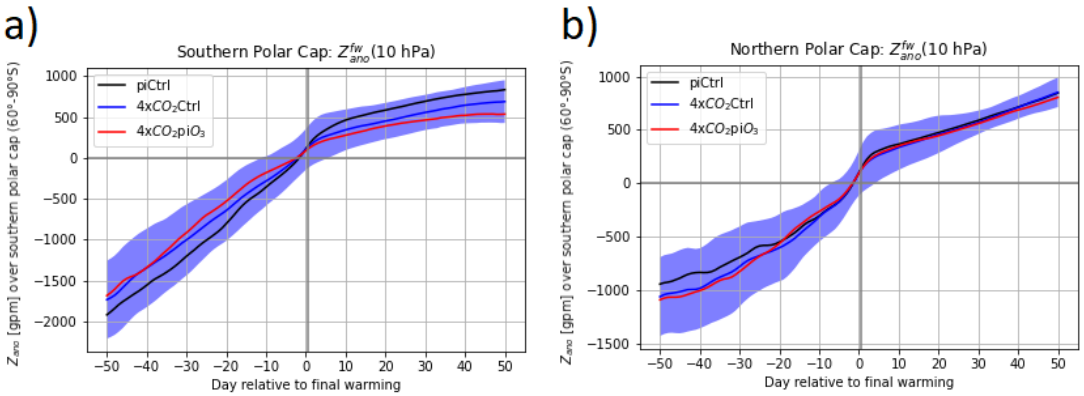

Figure 4.8: Geopotential height anomaly relative to the final warming date (Z_{ano}^{fw}) at 10 hPa for the piCtrl- (black), 4xCO_2Ctrl- (blue) and 4xCO_2piO_3-simulations (red) in m. Z_{ano}^{fw} is a function of day relative to final warming. The standard deviation of the 4xCO_2Ctrl-simulation is shown as blue shading.

In the southern polar cap, the slope of piCtrl is bigger than the slope of the 4xCO_2-simulations, which indicates a weaker final warming due to CO_2 increase (Figure 4.8 a). Z_{ano}^{fw} at 10 hPa is higher before the final warming takes place and lower afterwards. In the northern polar cap there are not visible changes of the slope between all 3 simulations (Figure 4.8 b). Nevertheless, Z_{ano}^{fw} in the 4xCO_2-simulations is smaller than in piCtrl before the final warming happens.

Next, the ozone effect on Z_{ano}^{fw} will be analyzed by comparing the 4xCO_2-simulations. The slope of 4xCO_2Ctrl is greater than the slope of 4xCO_2piO_3 in the southern polar cap that points out a more abrupt and thus stronger final warming through ΔO_3 (Figure 4.8 a). The enhancement of the abruptness in 4xCO_2Ctrl is a result of a compared to 4xCO_2piO_3 lower Z_{ano}^{fw} in the days before

and a higher Z_{ano}^{fw} in the day after the final warming. However, it has to note that piCtrl and $4xCO_2piO_3$ are inside the standard deviation of $4xCO_2$ in both polar caps.

Sudden Stratospheric Warmings (SSWs)

Climatologically, the polar vortex shows a non-significant but mostly systematic weakening by ozone changes (see Figure 4.5 a and c). That might be a link to the assumption of a modification of the number and duration of SSWs by ΔO_3. Therefore, a detection of the number of major and minor SSWs with the method of Charlton and Polvani (2007, see chapter 3.2.1) for all three simulations for the NH are presented in Table 4.1 a).

a)

Northern Hemisphere	**piCtrl**	**$4xCO_2$Ctrl**	**$4xCO_2piO_3$**
Number of major SSWs	16	10	8
Number of minor SSWs	23	27	33

b)

Northern Hemisphere	**piCtrl**	**$4xCO_2$Ctrl**	**$4xCO_2piO_3$**
Splitting			
Number	3	6	4
Mean duration	12 days	13 days	13 days
Displacement			
Number	10	8	8
Mean duration	14 days	14 days	12 days

Table 4.1: **a)** Number of the major and minor SSW events and **b)** number and duration of splitting and displacement SSW events for the piCtrl-, $4xCO_2$Ctrl- and $4xCO_2piO_3$-simulations in the NH.

In the pre-industrial climatology (piCtrl), 16 major SSWs and 23 minor SSWs take place in the NH. In Table 4.1 b), the number and duration of the SSWs, divided in splitting and displacement events according to the method of Seviour et al. (2013) for the NH is provided. The differentiation between splitting and displaced events is important for the specification of surface weather

impacts (Seviour et al. 2013). This method reveals more displaced than splitting SSWs (see Table 4.1 b: 10 displaced events with a mean duration of 14 days and 3 splitting events with a mean duration of 12 days). In the SH only minor SSWs occur in the simulations (see Table 4.2), which are rarer than in the NH.

However, in the southern polar cap the polar vortex is not disturbed as strongly by upward propagating waves as over the northern polar cap, which explains, that there are less SSW events in general.

To analyze the effect of CO_2 increase, the 4xCO_2Ctrl-simulation will be compared with the piCtrl simulation at this place. In the Arctic 6 major SSWs less are detected, but 4 minor SSWs more in the 4xCO_2Ctrl-simulation are found than in the piCtrl-simulation (see Table 4.1 a). Moreover, in the 4xCO_2Ctrl-simulation are 3 splitting events more and 2 displaced events less than in the piCtrl-simulation (see Table 4.1 b). In conclusion, it cannot be identified a direct impact of 4xCO_2 on the SSW frequency, which is consistent with the study by Ayarzagüena et al (2020).

Next, the impact on the numbers of SSW events due to ΔO_3 will be analysed. Therefore, the two 4xCO_2-simulations will be compared. It shows that in both hemispheres the difference between the number of minor SSWs is bigger due to ozone changes than due to CO_2 increase. This means in detail, that in the NH four minor SSWs less happen with a changed ozone field (4xCO_2Ctrl) than with an unchanged field (4xCO_2piO_3). Moreover, there are two major SSWs more in 4xCO_2Ctrl than in 4xCO_2piO_3. However, the difference of the number of minor SSWs between the simulation with pre-industrial condition (piCtrl) and the simulation with 4xCO_2-conditions is even higher. With ΔO_3 there are only two more splitting event than without and the number of displacement events is equal. In summary, significant impacts of ozone on the SSWs cannot be identified.

For completion the results of the number of minor and major SSWs in the SH are shortly discussed, too. Table 4.2 gives an overview of these types of SSWs for all three simulations in the SH. A comparison between the simulations shows that there are one more SSW in 4xCO_2Ctrl than in piCtrl and even three more than in 4xCO_2piO_3. This indicates that the change of the occurrence of SSWs due to ozone changes is larger than due to 4xCO_2 itself. Nevertheless, the fact that the numbers are generally so small leads to the statement that ozone does not have a significant impact on the SSWs in the SH, either.

Southern Hemisphere	piCtrl	4xCO$_2$Ctrl	4xCO$_2$piO$_3$
Number of major SSWs	0	0	0
Number of minor SSWs	4	5	2

Table 4.2: Number of the major and minor SSW events for the piCtrl-, 4xCO$_2$Ctrl- and 4xCO$_2$piO$_3$-simulations in the SH.

4.2.3 Brewer-Dobson Circulation and Water Vapor Transport

Eliassen-Palm Flux (EP Flux)

The polar vortex has been shown to be systematically attenuated by ozone changes. A change of the vortex cannot be only caused by a modification of the meridional temperature gradient below but also wave breaking plays an important role here, which is explained in chapter 2.4. Therefore, the acceleration of the zonal flow by the EP flux divergence (EPFD) will be analyzed next. The EPFD is linked to the planetary and synoptic-scale wave breaking. First, the EPFD for the pre-industrial climatology is shown for the JJA mean (Figure 4.9 a) and for the DJF mean (Figure 4.9 b), then the CO2- and ozone effect will be depicted in Figure 4.10. The contours in Figure 4.9 depict the pre-industrial zonal wind in units of m/s.

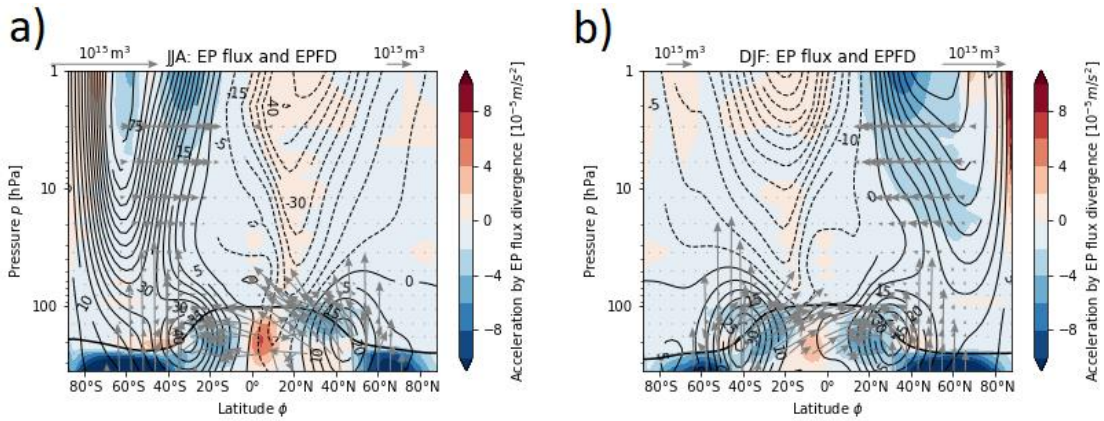

Figure 4.9: Latitude-height cross-sections of the EPFD (colours) and of the EP flux (arrows) pre-industrial climatology for the mean over JJA (**left**) and DJF (**right**). The black thick line illustrates the tropopause and the contours depict the zonal mean zonal wind for pre-industrial CO$_2$-conditions Note, that the arrows in the two hemispheres are scales differently.

Climatologically, the EP flux goes upward over the extra-tropics and then they are deflected towards the equator (see Figure 4.9). If the waves reach the regions of zonal winds, where the critical windspeed U_c (see chapter 2.4.1) is reached, the waves break or dissipate. This happens

at the STJ and polar vortex. The wave breaking leads to a deceleration of these mean flows (see chapter 2.4.2).

Figures 4.10 a and b illustrate the effect of a higher amount of CO_2 ($4xCO_2Ctrl$) on the EPFD (colours) and EP Flux (arrows). The two Figures at the bottom (Figure 4.10 c and d) depict the impact of ΔO_3 on these quantities. The contours depict the pre-industrial EPFD in units of 10^{-5} m/s^2.

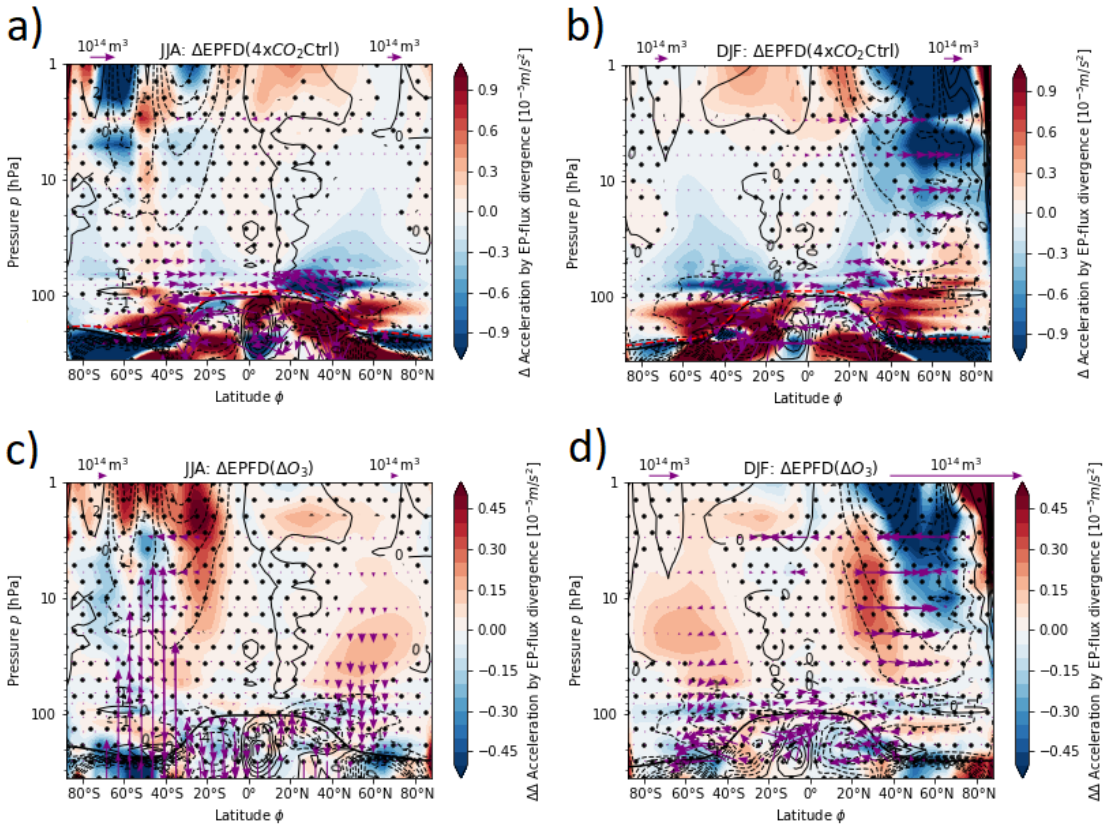

Figure 4.10: Latitude-height cross-sections of the EPFD (colours) and of the EP flux (arrows) response on $4xCO_2Ctrl$ (**a** and **b**) and on ΔO_3 (**c** and **d**). The responses are shown for the mean over JJA (**left**) and DJF (**right**). The black thick line illustrates the tropopause and the contours depict the EPFD for pre-industrial CO_2-conditions. The red dashed line is the tropopause for $4xCO_2$-conditions. Note, that the arrows in the two hemispheres are scales differently. Non-significant responses at the 95 % confidence level are stippled.

In the $4xCO_2Ctrl$-simulations the convergence of the EP flux at the STJ is increased (Figure 4.10 a and b). The enhancement of flux convergence indicates a stronger wave breaking, which is depicted with a decrease in EPFD. In addition to that, there is also a negative change of the EPFD in the vicinity of the Arctic polar vortex (see Figure 4.10 b). This might be linked to a weaker pole-to-equator EP flux in these altitudes. However, in general the changes of the polar vortecies are not yet fully understood. In summary, there is a stronger wave breaking at the STJs and at the

Arctic polar vortex. According to Shepherd and McLandress (2011), the stronger upward wave propagation to the STJs is forced by an upward shift of the STJ and thus of the edge of critical windspeed region (critical wind line), where the waves cannot propagate anymore.

After the influence of $4xCO_2$ on the EP flux was discussed, the impact of ozone changes will be investigated (Figures 4.10 c and d). In the middle stratosphere of the mid-latitudes in the winter hemispheres, where the polar vortex is located, non-significant, predominantly negative changes for the northern and southern winter stratosphere can be seen. However, the upward EP flux to the Antarctic polar vortex increases, which shows that more planetary waves propagate vertically to the Antarctic polar vortex and break there (Figure 4.10 c). This indicates that the systematic weakening of the Antarctic polar vortex is not only caused by ozone-induced modification of the meridional temperature gradient, but also due to stronger planetary wave breaking. In the middle stratosphere of the NH the meridional EP flux from the pole to the equator decreases. On the other hand, in most regions of the summer stratosphere the impact of ozone on the acceleration of the mean flow by the EPFD is significant. There, a positive change of the acceleration by the EPFD can also be observed at the upper flank of the STJ. This acceleration of the STJ is caused by a weakening of the CO_2-induced strengthening of the upward propagation of synoptic-scale waves to the STJ (see Figure 4.10). Therefore, less waves reach the STJ. That in turn might damp the CO_2-induced acceleration of the shallow BDC branch.

Mass Streamfunction

In the previous sub-chapter the shallow BDC branch was suspected to be affected by the EPFD changes. Therefore, Figure 4.11 illustrates the response of the mass streamfunction, as a diagnose of the residual flow on $4xCO_2$ (Figures 4.11 a and b) and on ΔO_3 (Figures 4.11 c and d) for JJA and DJF. The contours depict the mass streamfunction for pre-industrial CO_2-concentration in 10^5 kg/s.

First, the impact of $4xCO_2$ on the BDC is discussed. Higher CO_2 concentrations increase the total values of the mass streamfunction in both hemispheres. In most regions the increase even is statistically significant. These higher values of the mass streamfunction indicate a strengthening of the BDC globally, which is a result of the strong EPFD (see Figures 4.10 a and b) in vicinity of the STJ (Shepherd and McLandress, 2011).

In the next step the influence of ΔO_3 on the mass streamfunction will be analyzed. There are significant changes in the shallow branch of the summer hemisphere (Figures 4.11 c and d). The mass streamfunction decreases in both hemispheres due to ozone changes. Additionally, the mass streamfunction weakens systematically in the northern and southern winter hemisphere. This

counteracts the CO_2-induced acceleration of the BDC is in line with the study by DallaSanta et al. (2021). This study showed that ozone changes by CO_2 increase weakens the tropical upwelling enhancement. Therefore, an analysis of the mean vertical residual velocity $\overline{w}^*$ between the turnaround latitudes at the tropics is done next. $\overline{w}^*$ in the tropics is a widely used diagnostic for the BDC strength (see e.g. Dietmüller et al., 2018, Garcia and Randel, 2008, Eichinger and Šácha, 2020).

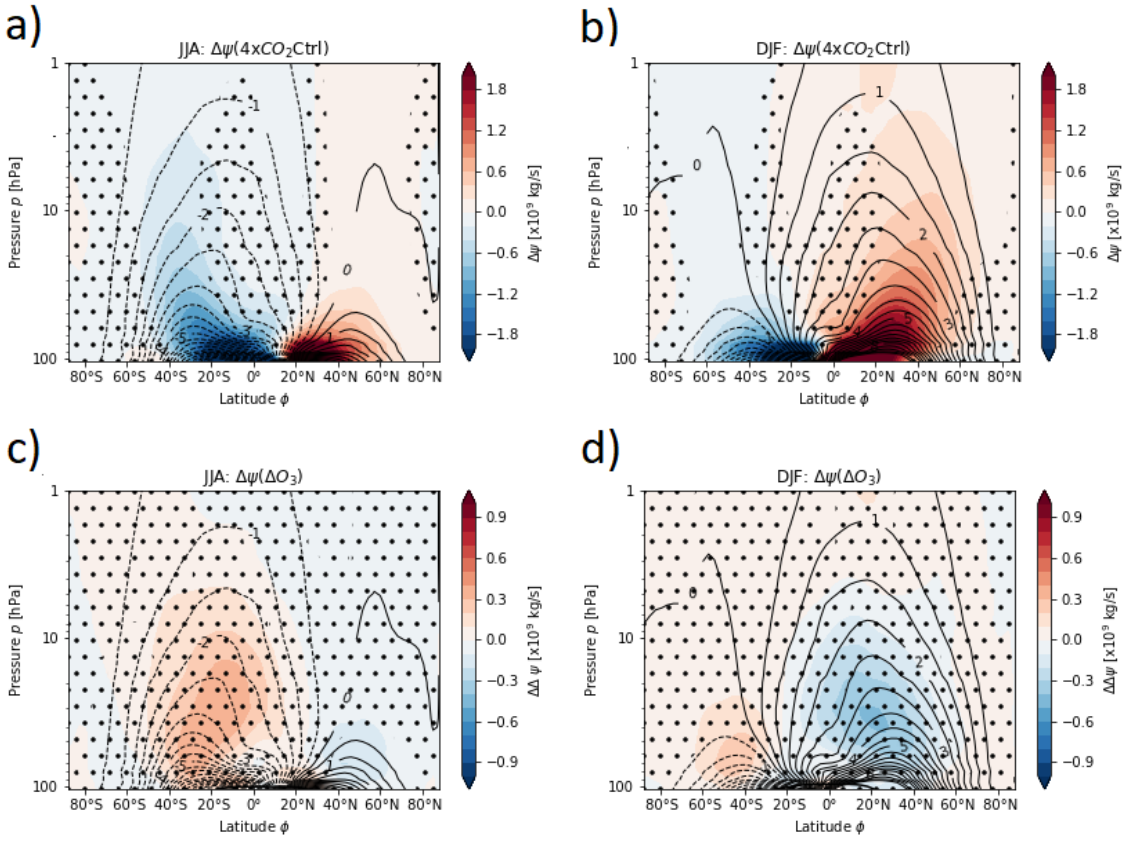

Figure 4.11: Latitude-height cross-sections of the zonal-mean streamfunction ψ on 4xCO_2Ctrl (**a** and **b**) and on ΔO_3 (**c** and **d**) for the mean over JJA (**left**) and DJF (**right**). Contours depict the streamfunction ψ for pre-industrial CO_2-conditions in 10^9 kg/s. Non-significant responses at the 95 % confidence level are stippled.

Tropical Upwelling

Figure 4.12 depicts the response of $\overline{w}^*$ between the turnaround latitudes on 4xCO_2Ctrl and on 4xCO_2piO_3 in JJA as a function of the pressure (Figure 4.12 a) and DJF (Figure 4.12 b). The altitudes where the difference between the 4xCO_2-simulations is statistically significant are marked with a thick blue line at the 4xCO_2Ctrl-simulation showing a significant response of the tropical upwelling due to ozone.

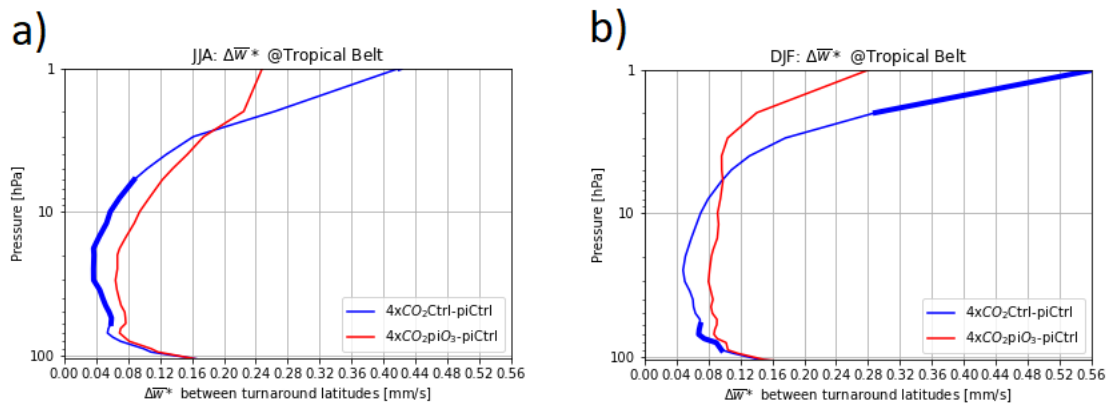

Figure 4.12 Response of the mean residual velocity $\overline{w}^*$ between the turnaround latitudes in the tropics on $4xCO_2$Ctrl ($4xCO_2$Ctrl-piCtrl, blue) and on $4xCO_2piO_3$ ($4xCO_2piO_3$-piCtrl, red). This is shown as function of pressure for **a)** JJA and **b)** DJF. The heights, where the differences between $4xCO_2$Ctrl and $4xCO_2piO_3$ are statistically significant at the 95 % confidence interval are marked with a thick blue line.

Climatologically, the tropical upwelling is weakest in the lower and strongest in the upper stratosphere. $4xCO_2$ enhances the tropical upwelling throughout all altitudes in the stratosphere. This is consistent with the long-term trend caused by increased greenhouse gas concentration discussed in Li et al. (2007) and in Garcia and Randel (2008). The enhancement of the upwelling by $4xCO_2$ is a result of an enhanced wave forcing in the extra-tropical stratosphere due to an upward shifted STJ (see Figure 4.10).

The effect of ozone change due to the CO_2 increase will now be discussed by comparing the two CO_2-simulatons. In JJA the difference of $\overline{w}^*$ between the $4xCO_2$-differences is statistically significant between 60 and 6 hPa, which is located in the middle and lower stratosphere. In DJF the statistically significant changes are only in the lower stratosphere (between 90 and 60 hPa). Nevertheless, in both seasons the response of $\overline{w}^*$ in the tropics on ΔO_3 is significant in the lower parts of the stratosphere where the shallow branch of the BDC is located. Moreover, in the middle and lower stratosphere the response of $\overline{w}^*$ on $4xCO_2$Ctrl is weaker than on $4xCO_2piO_3$ in both seasons. In the upper stratosphere, there is a stronger tropical upwelling due to ozone changes, which is even significant in DJF. This enhanced upwelling is consistent with the systematic acceleration of the residual circulation in the upper stratosphere in winter (see Figure 4.11). Moreover, the strengthening of the upper stratospheric tropical upwelling in northern winter is linked to the systematic stronger wave forcing at the Arctic polar vortex (see Figure 4.10).

In summary, the weakening of the tropical upwelling in the lower stratosphere that is connected with the shallow branch of the BDC is a robust impact on ΔO_3. Furthermore, this weakening is caused by a reduction of ozone concentration in the lower tropical stratosphere, which results in radiative cooling in this region.

Mean Age of Air (AoA)

The BDC is the whole transport circulation in the stratosphere and not only a part of the residual circulation that is diagnosed with the mass streamfunction (Figure 4.11). Therefore, the BDC will be investigated with the AoA, which is a more precise measure for the transport circulation like the BDC. This motivates to analyse the AoA response on the ozone changes. The results are shown in Figure 4.13. The change of the AoA due to 4xCO_2Ctrl (Figures 4.13 a and b) and due to ΔO_3 (Figures 4.13 c and d) is depicted as colored shadings. The contours illustrate the AoA for pre-industrial conditions.

Quadrupling of CO_2 leads to a decrease of the AoA by between 0.5 years in the tropical lower stratosphere and 1.5 years in the extra-tropical stratosphere (Figures 4.13 a and b). This is in line with an enhancement of the BDC strength through higher CO_2 concentrations that accelerates the meridional tracer transport. However, there is no uniform change in the AoA, because also isentropic mixing processes happen, which influence the AoA in addition to residual transport (Garny et al., 2014).

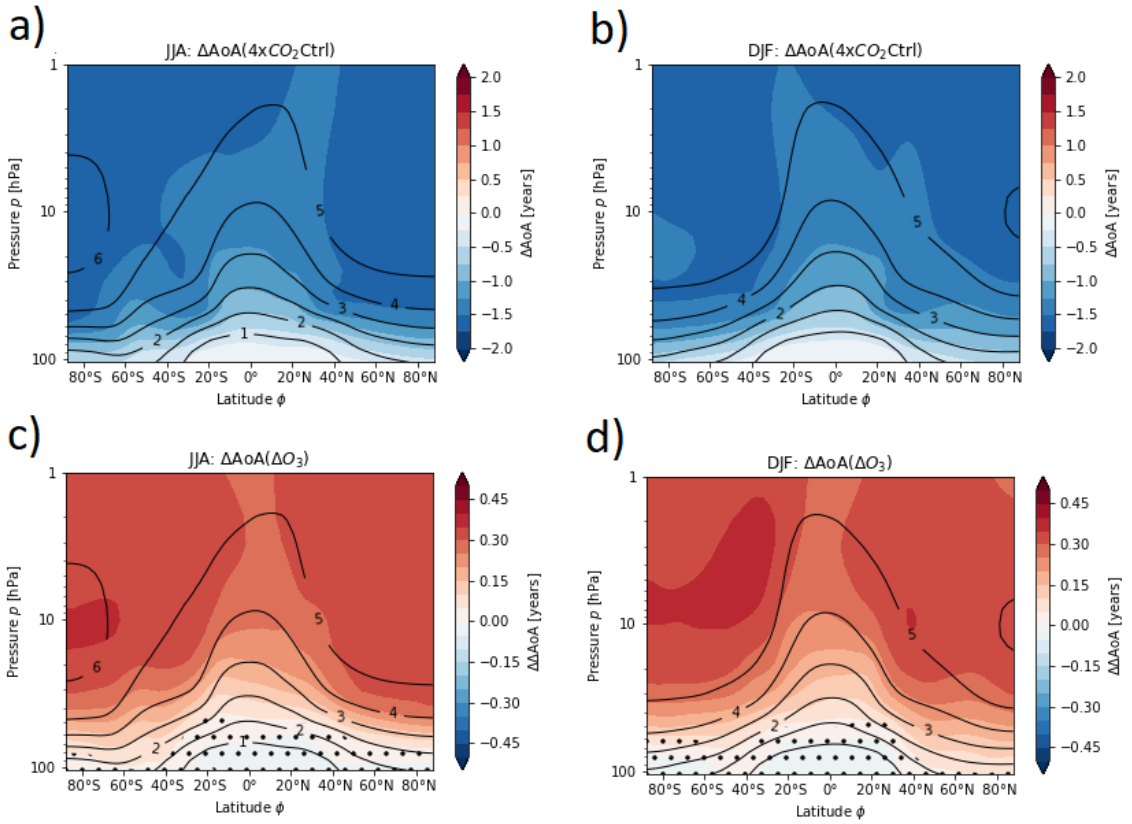

Figure 4.13: Latitude-height cross-sections of the reponse on zonal-mean age of air (AoA, colours) on 4xCO_2Ctrl (**a** and **b**) and on ΔO_3 (**c** and **d**) for the mean over JJA (**left**) and DJF (**right**). Contours depict the AoA for pre-industrial CO_2-conditions in years. Non-significant responses at the 95 % confidence level are stippled.

The CO_2-induced ozone changes lead to an increase of the AoA (Figures 4.13 c and d). Here, a significant aging of the stratospheric air by ozone changes happens in the whole stratosphere in winter and summer. In contrast, Figures 4.12 c and d show the BDC diagnostic with the mass streamfunction. In this diagnostic the response on the mass streamfunction due to CO_2-induced ozone changes was systematic in the entire stratosphere, but significant only in the summer shallow branch. This difference of the significance between the response of the AoA and mass streamfunction on ΔO_3 can be explained as follows:

According to Hall and Plumb (1994, see chapter 3.2.4) the AoA is a spatial and temporal integral over the mass fraction of the air parcel that propagates along the BDC branches. In other words, the AoA is a spatial (vertical) and temporal integration over the stratospheric mass streamfunction. Therefore, an integration over statistically non-significant but systematic values of the mass streamfunction response can result in statistically significant values, which in this case is the AoA response. Moreover, between winter and summer there are no visible differences in the AoA changes, which is also an effect of the integration over time.
A maximum is located at the SH polar region around 10 hPa within the polar vortex barrier (see Figure 4.13 c). The vortex barrier prevents the air from lower latitudes from intrusion into the polar stratosphere. Therefore, the polar air is isolated during the winter that results in a higher AoA in this region.

The response of the BDC which impacts tracer transport and thus the AoA is driven by breaking synoptic-scale and planetary waves but also by gravity wave breaking. To diagnose, which of these waves causes the change in the BDC strength, the impact of breaking of different wave types on the mass streamfunction will be analyzed next using the downward control principle.

Downward Control Analysis

The BDC is driven by breaking planetary and synoptic-scale waves, which is quantified by the EPFD, and by breaking gravity waves that is represented by the gravity wave drag (GWD). The exact theory behind these processes is explained in chapters 2.4.2 and 2.4.4. Therefore, to find the cause of the above described changes in the residual circulation, the fraction of the forcing by planetary, synoptic-scale and gravity waves, the downward control method is quantified. To compare the effect of ΔO_3 with the effect of $4xCO_2$, the impact of $4xCO_2$Ctrl and $4xCO_2$piO_3 was calculated, too. The result of this diagnostic is shown in Figure 4.14. It illustrates the impact of the EPFD (red) and GWD (grey) on the damping of the shallow branch. The GWD is the sum of the orographic gravity wave drag (OGWD, brown) and non-orographic gravity wave drag (NOGWD, yellow), The sum of all wave forcings (Total = EPFD + GWD) is illustrated as blue

line. The streamfunction was calculated by the TEM equation (TEM, black). As a representative level for the shallow branch the 70 hPa pressure level is taken.

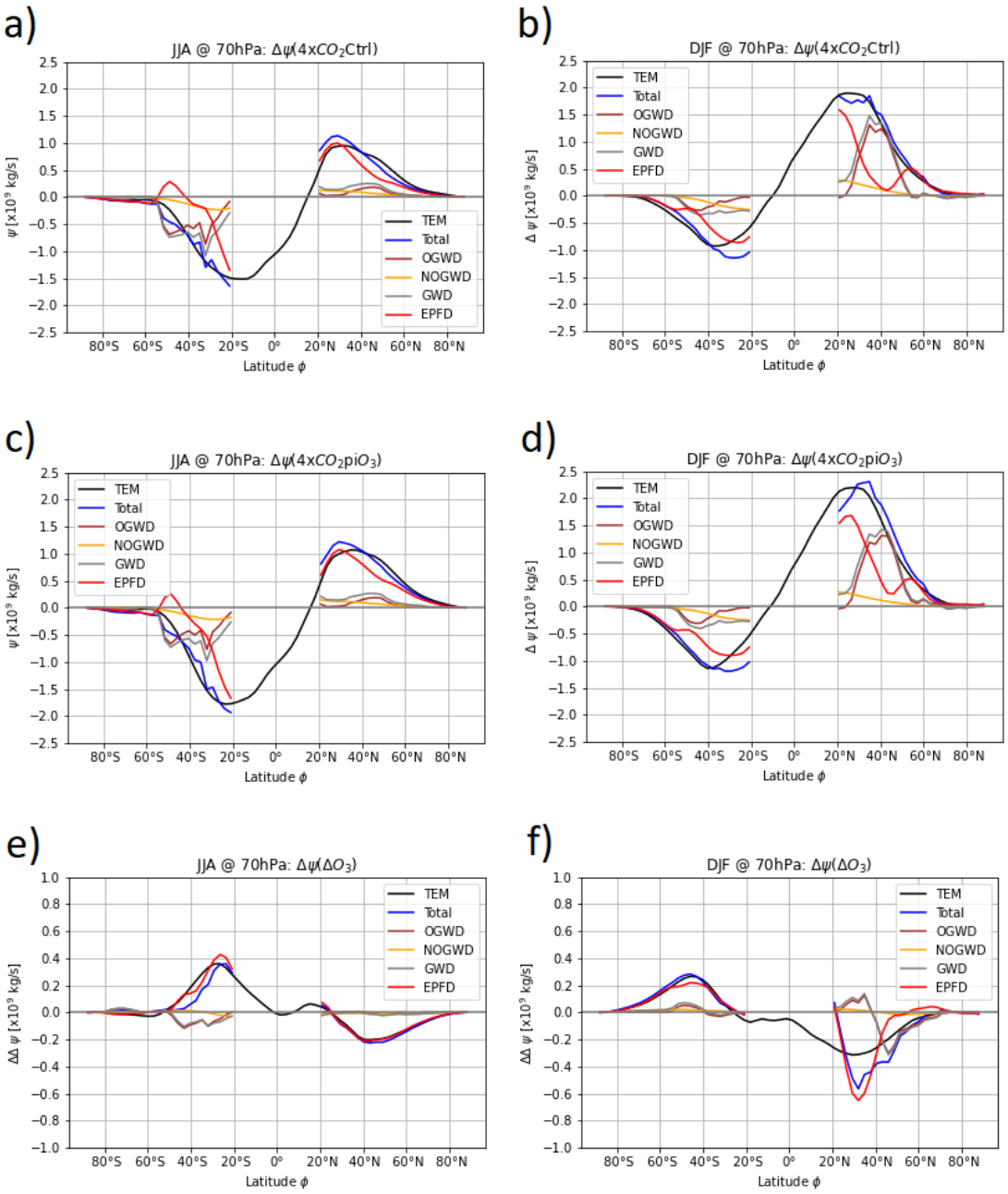

Figure 4.14: Climatology of the change in the mass streamfunction due to 4xCO2Ctrl (**a** and **b)** and due to 4xCO2piO3 **(c** and **d**) as well due ΔO3 (**e** and **f**). This is shown for the JJA mean (**left**) and for the DJF mean (**right**) at 70 hPa as a function of latitude. The streamfunction is calculated via the TEM equations (TEM, black) and with the downward control method for EPFD (red) and GWD (grey), which is the sum of OGWD (brown) and NOGWD (yellow). The sum of all these wave forcings (Total = EPFD + GWD) is represented as a blue line.

Quadrupling of the CO_2 concentration increases the total values of the mass streamfunction in the lower stratosphere independent of the prescribed ozone field (Figures 4. 14 a – d), which is in line

with an acceleration of the shallow BDC branch due to $4xCO_2$ illustrated in Figure 4.11 a) and b). This is forced by EPFD in winter and summer. In addition to that, there is a forcing by GWD in winter. The additional acceleration by GWD is one reason, why there is larger change in the winter hemisphere. Moreover, the total increase of the mass streamfunction in summer is weaker in $4xCO_2$Ctrl than in $4xCO_2piO_3$, showing the mitigation of the shallow BDC branch in summer through ΔO_3. To quantify this weakening of the shallow branch in terms of wave forcing, the difference between $4xCO_2$Ctrl and $4xCO_2piO_3$ was calculated. The result of this (Figures 4.14 e and f) will be discussed next.

In both summer hemispheres, the change of the mass streamfunction is mostly influenced by the EPFD in both seasons. The GWD has only a weaker impact, mostly in the winter hemisphere. In winter the mass streamfunction of the sum of all wave forcings does not fit to the TEM mass streamfunction (Figure 4.14 f). This difference between the total wave forcing and the TEM is similar to the difference of the total wave forcing and the TEM between the $4xCO_2$-simulations above. Moreover, the difference between the total wave forcing and the TEM in ΔO_3 are also much smaller than the CO_2 effects. Moreover, the ozone effect on the mass streamfunction in the winter hemisphere is not statistically significant (see Figure 4.11). In the summer hemisphere, on the other hand, the change of the mass streamfunction due to ΔO_3 is robust in the lower stratosphere, where the shallow branch is located. There, the EPFD is the main driver of the damping in the shallow branch (Figures 4.14 e and f). Physically, the shallow branch is mainly driven by breaking synoptic-scale waves at the STJ (Holton and Hakim, 2013), which is linked to a negative EPFD. In Figure 4.10, a significant positive change of the EPFD is diagnosed at the upper flank of the STJ. This means that the wave breaking is weakened and thus, the shallow branch is damped by the changes in the EPFD, consistent with the diagnostic in Figure 4.14.

Stratospheric Water Vapor

A change in the residual circulation results in a change in transport of tracers like water vapor. Stratospheric water vapor absorbs and emits longwave radiation, which has an effect on the heating rates and changes the temperature and dynamics (Kraus, 2004). Therefore, the impact of ozone on the stratospheric water vapor will be analyzed. Figure 4.15 depicts a of the influence of $4xCO_2$Ctrl (Figure 4.15 a) and ΔO_3 (Figure 4.15 b) on the specific humidity in the lower stratosphere as a function of time. The relative response and not the total response of the specific humidity on ozone changes is illustrated for visual purposes.

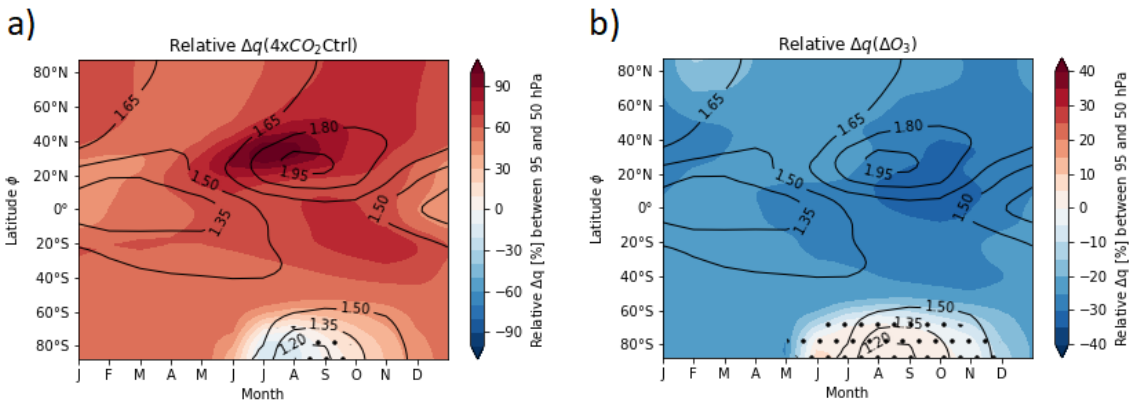

Figure 4.15: Climatology of the relative response of specific humidity (colours) on 4xCO_2Ctrl (**a** and **b**) and on the ozone changes due to 4xCO_2 (**c** and **d**) in the lower stratosphere averaged between 95 and 50 hPa. The black thick line illustrates the specific humidity in µg/kg for pre-industrial CO_2-conditions. Non-significant responses at the 95 % confidence level are stippled.

The major source of stratospheric water vapor is the troposphere. Transport of water vapor from the troposphere to the stratosphere happens through the tropical tropopause. The amount of water vapor entering the stratosphere is higher/lower, if the tropical tropopause temperature is higher/lower (Fueglistaler et al., 2005). Climatologically, the highest amount of stratospheric water vapor can be observed during the NH summer, when the Asian summer monsoon leads to enhanced water vapor trasnport through the tropical tropopause (Fueglistaler et al., 2005). After having entered the tropical lower stratosphere, water vapor is transported upward within the tropical pipe and to the extra-tropics by the shallow BDC branch.

In addition to this, it is worth mentioning that the oxidation of methane is another source of the stratospheric water vapor. According to Stenke and Grewe (2005) the increase of methane over the last decades of the 20th century is responsible for around 30 % of the total water vapor increase. However, this is not important for the simulations used in the present study that are focused on the impact of CO_2 increase and the accompanied ozone changes.

The warming in the tropical upper troposphere in 4xCO_2Ctrl (see Figures 4.3 a and b) increases the specific humidity in the lower stratosphere by mostly 40 to 70 %, which illustrates Figure 4.14 a). From June to August the increase in the northern tropical belt is even 100 %. In contrast, the specific humidity decreases in the Antarctic lower stratosphere, which is linked with the systematically stronger Antarctic polar vortex isolating the polar lower stratospheric air from the rest of the stratosphere like a mixing barrier.

The CO_2-induced change of ozone (ΔO_3) results in a 15 – 25 % drier lower stratosphere, which is due to the O_3-induced cooling of the tropical tropopause region (see Figure 4.3 c and d). These results are consistent with the studies by Nowack et al. (2018) and Dietmüller et al. (2014). The specific humidity does not change in the SH polar region during winter.

However, it has to be mentioned that the ozone effects on water vapor are probably biased to some degree, because the ozone field is not adjusted to the upward tropopause shift in the 4xCO_2piO_3-simulation. This leads to an unphysically high ozone concentration and thus to a too high tropical tropopause temperature. A more detailed discussion to this impact follows in chapter 5.

4.2.4 Downward Influence on the Troposphere

Zonal Wind

Next, the effect of the 4xCO_2 increase and of the ozone changes on the downward impact from the stratosphere to the troposphere will be investigated. For this, a timeseries of the zonal wind response between 50 and 70° S/N for 4xCO_2 and for ΔO3 in the SH and NH are shown in Figures 4.16 a, b and 4.16 c, d, respectively. The black contours illustrate the zonal wind for pre-industrial CO_2 conditions. in m/s.

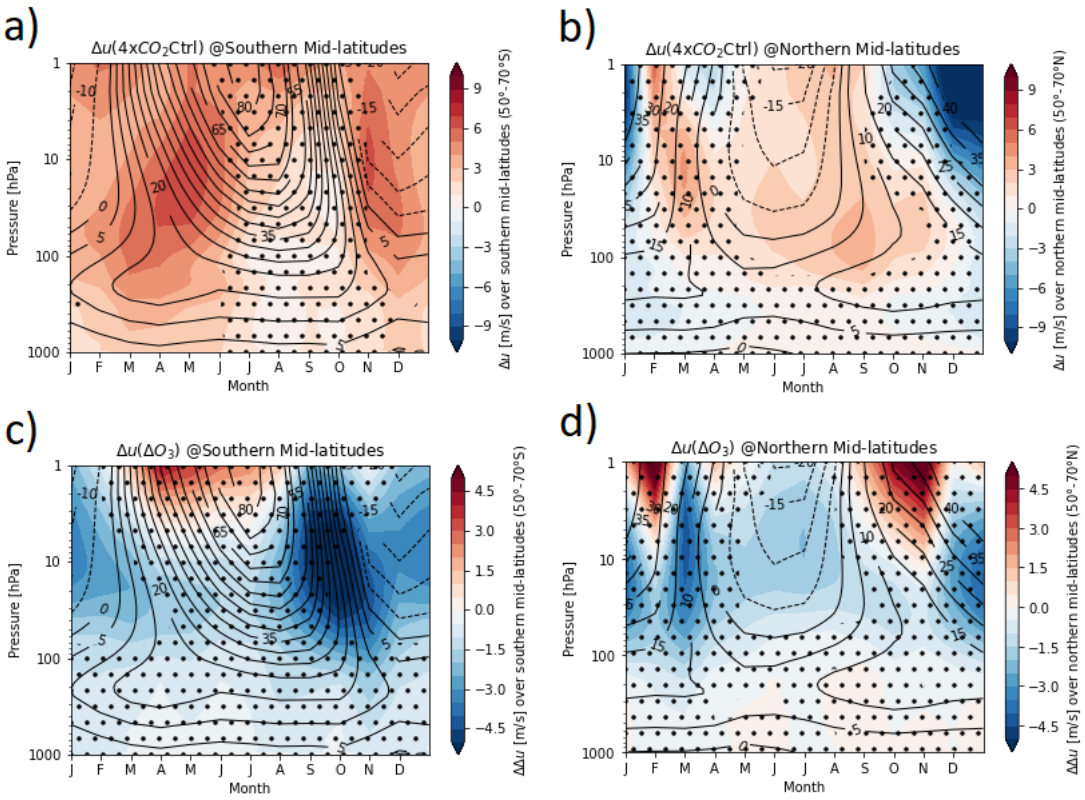

Figure 4.16: Response of the climatology of zonal mean zonal (colours) on 4xCO_2Ctrl (**a** and **b**) and on the ozone changes due to 4xCO_2 (**c** and **d**) in the mid-latitudes averaged between 50 ° and 70 ° S/N. The responses are illustrated for the southern mid-latitudes (**left**) and northern mid-latitudes (**right**) as a function of pressure and month. Black contours depict the zonal mean zonal wind for pre-industrial conditions in meter. Non-significant responses at the 95 % confidence level are stippled.

In summer and spring, $4xCO_2$ significantly weakens the mid-latitude easterly zonal winds. In the SH, this weakening is about 2 times as strong as in the NH. Moreover, in the NH the polar vortex weakens and in the SH strengthens during early winter. The increased zonal wind at the beginning and end of the polar vortex seasons marks that the polar vorticies are longer persistent. due to $4xCO_2$. These effects are consistent with the polar vortex diagnostics in chapter 4.2.2.
Furthermore, the positive changes at the end of the vortex season in the SH reach down to the troposphere and strengthens the EDJ, which is consistent with the study of Byrne and Shepherd (2018). Moreover, this enhancement of the SH EDJ can be seen in Figures 4.4 a and b in chapter 4.2.1. There are also statistically significantly increased zonal winds in the SH troposphere during summer and autumn that propagates upward to the stratosphere in autumn

The results above raise the question in which way CO_2-induced ozone changes influence this effect. Therefore, the zonal wind response on ΔO_3 is shown in Figures 4.16 c and d. In the stratosphere, the easterlies during summer are enhanced and the polar vorticies are systematically weakened, which is also analyzed in the chapters 4.2.1 and 4.2.2. Indication for a later vortex build up and earlier break down (final warming) can be obtained by decreasing zonal wind speeds at the beginning and at the end of the polar vortex season.
The decrease of the zonal wind systematically extends down to the troposphere in the SH in November and in the NH in March. This effect leads to the conclusion that EDJ weakens by the ozone-induced shift of the final warming date. Therefore, the impact of CO_2-induced ozone changes on the EDJ strength will be investigated next.

Eddy-Driven Jets (EDJs)

Figures 4.16 c and d show a downward influence of ΔO_3 on the EDJ strength. Moreover, there were analyzed impacts of changes in the duration of the polar vortex season on the EDJ strength and position in various studies (see e.g. Byrne and Shepherd, 2018 and Cheppi and Shepherd, 2019). Therefore, Figure 4.17 a) and Figure 4.17 b) depicts the climatological mean of the jet strength in the NH and SH for the piCtrl-, $4xCO_2$Ctrl- and $4xCO_2piO_3$-simulations. The blue shading illustrates the standard deviation of the $4xCO_2$Ctrl-simulation.

The EDJ is strongest in spring and in SH also in autumn. $4xCO_2$ strengthens the SH EDJ systematically, which is consistent with the influence of the stronger zonal wind from the stratosphere to the troposphere (see Figure 4.16 a). From spring until autumn the zonal winds of the piCtrl-simulation is even outside the standard deviation of $4xCO_2$Ctrl (Figure 4.17 a). The NH EDJ does not show any robust changes in strength due to $4xCO_2$ (Figure 4.17 b), but there is at least a systematic stronger EDJ in autumn.

An impact of ozone changes on the jet strength can be seen as well. The CO_2-induced strengthening of the EDJ is systematically damped by ozone changes in the SH in spring. This can be explained by the downward effect of the earlier final warming due to ozone changes (see Figure 4.16 c and d).

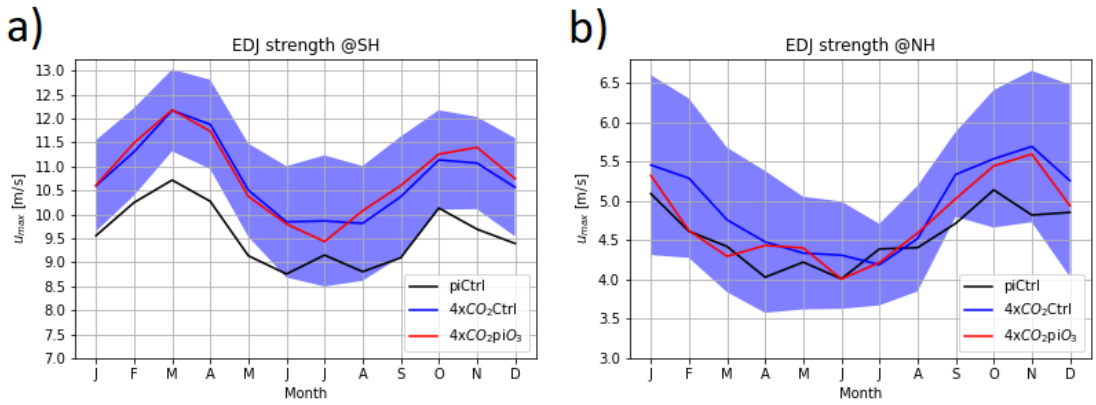

Figure 4.17: Climatological mean of the EDJ strength in the **a)** SH and in the **b)** NH for the piCtrl- (black), 4xCO_2Ctrl- (blue) and 4xCO_2piO_3-simulations (red) in m/s. The standard deviation of the 4xCO_2Ctrl simulation is shown as blue shading.

Figure 4.18 shows in which way ΔO_3 affect the position of the EDJ. This Figure depicts a climatology of all three simulations for the EDJ position as a function of latitude. Climatologically, the EDJ of the SH is closer to the pole in autumn and closer to the equator in winter (Figure 4.18 a). The EDJ of the NH is closer to the pole in summer and closer to the equator in winter (Figure 4.18 b).

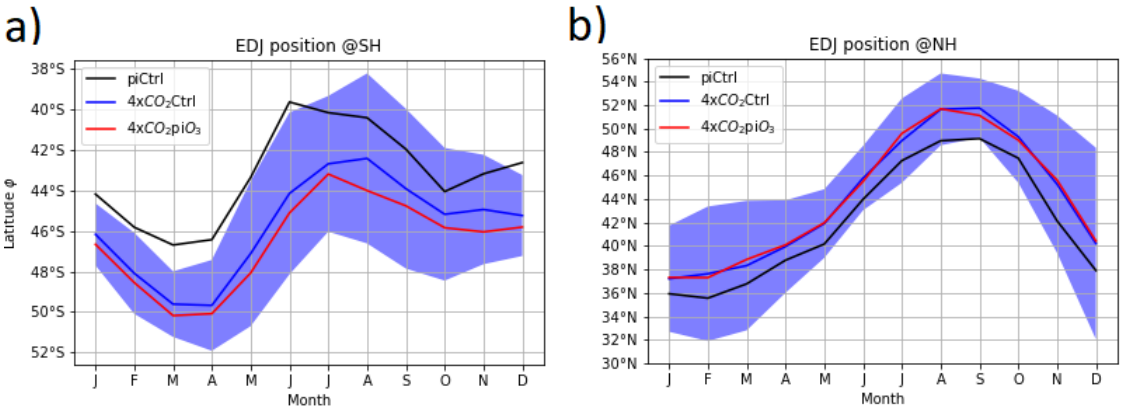

Figure 4.18: Climatological mean of the EDJ position in the **a)** Southern Hemisphere (SH) and **b)** the NH for the piCtrl- (black), 4xCO_2Ctrl- (blue) and 4xCO_2piO_3-simulations (red) in m/s. The standard deviation of the 4xCO_2Ctrl simulation is shown as blue shading.

Through a higher amount by CO_2, the position of the jet is shifted systematically poleward, which is in line with the studies by Byrne et al. (2017), Byrne and Shepherd (2018) and Ceppi and Shepherd (2019). That shift in the SH is even significant from December to April. Moreover, the time when the SH EDJ is nearest to the equator is 2 months reached later if CO_2 increases. This is consistent with the later final warming of the polar vortex due to $4xCO_2$

Now it will be analyzed how the ΔO_3 impact the jet position by comparing the $4xCO_2$-simulations. Strong and significant differences cannot be identified in the NH (Figure 4.18 b). However, in the SH the EDJ position in $4xCO_2$Ctrl is systematically nearer at the equator than the EDJ position in $4xCO_2piO_3$ (Figure 4.18 b). This means, that ΔO_3 systematically damps the CO_2-induced poleward shift of the EDJ, which is in line with the decrease of the zonal wind at the poleward flank of the EDJ in the SH (see Figures 4.4 c and d).
Additionally, the northernmost position is detected one month later, if ozone is changed. That in turn is not in line with the earlier final warming due to ozone changes that is analyzed in chapter 4.2.2.

5 Discussion and Outlook

The previous chapter shows the wide-ranging impact of CO_2-induced ozone changes on the dynamics in the stratosphere and troposphere. Some of the shown results require more explanations or have to be put in a broader context. Therefore, in this chapter these results are discussed in detail.

The CO_2-induced change in the ozone field modifies the shortwave heating rates, which is explained in chapter 4.1.1. The response of shortwave heating in tropics and extra-tropical summer hemisphere is similar to the changes in the ozone field through $4xCO_2$. In the upper stratosphere and in most parts of the extra-tropical stratosphere, where ozone increases more shortwave radiation is absorbed by ozone. That leads to shortwave heating. On the other hand, the decrease of ozone in the lower tropical stratosphere causes that less shortwave radiation is absorbed and this results in shortwave cooling.
The adiabatic heating due to the dynamics is only responsible for a small part of the temperature response (Dietmüller et al., 2014). Therefore, the significant temperature response due to ozone (see Figure 4.3) is proportional to the response of shortwave heating, which is influenced by the ozone-induced absorption of shortwave radiation as described above.
Nevertheless, the question arises, what the relative role of the lower-stratospheric extra-tropical heating and tropical cooling due to ozone changes of the meridional temperature gradient and thus on the dynamics is. This has to be investigated in a specifically dedicated experiment.

Water vapor is the most important greenhouse gas. Modifications in the water vapor concentrations affect the absorption and emission of longwave radiation and thus influences the temperatures and potentially the dynamics.
The changes of ozone lead to a relative decrease of the specific humidity of around 15 – 20 % in the stratosphere (see Figure 4.15). This effect was also found by Dietmüller et al. (2014) and Nowack et al. (2018), who explained it with a lower tropical cold point temperature. Furthermore, Dietmüller et al. (2014) showed that the reduction of the stratospheric water vapor causes a damping of the climate sensitivity, which modifies the temperature change at the surface.
However, it is worth mentioning that the stratospheric water vapor and the tropical upwelling in the $4xCO_2piO_3$-simulation are probably affected by the too high ozone concentration in the upper tropical stratosphere. Quadrupling of the CO_2 concentration lifts up the tropopause, but in the $4xCO_2piO_3$-simulation the ozone distribution does not change. Therefore, the ozone concentrations in the upper troposphere is unphysically high and thus the temperature is also too high in this region (Hardiman et al., 2019). This leads to a too high tropical cold point temperature which causes an increased water vapor intrusion into the stratosphere. Hardiman et al. (2019) suggest to correct this mismatch between tropopause and ozone by a redistribution of ozone. For

this redistribution the ozone tropopause is defined at 1 km below the thermal tropopause. At the ozone tropopause the ozone molar mixing ratio is set to 80 nmol/mol. The ozone of the troposphere is shifted to the stratosphere.
For further investigations to this study, the above described ozone redistribution method according Hardiman et al. (2019) can be applied to get a more realistic cold point temperature.
Using the redistribution method by Hardiman et al. (2019), the stratospheric water vapor concentrations and the cold point temperature will reduce. However, in the recent study the response of the temperature and of the zonal wind in the lower stratosphere is similar to Chiodo et al. (2017 and 2019) and Nowack et al. (2018).

The temperature change in the stratosphere through ozone modifies the meridional temperature gradient in the lower stratosphere. In chapter 4.2.1 it is explained that this change is in line with the strengthening of the stratospheric easterlies in summer and with the non-significant but systematic weakening of the polar vorticies in winter. This negative change of the zonal winds in winter and summer in both hemispheres is mentioned in some studies (e.g. Nowack, 2018 and Chiodo and Polvani, 2019). However, the statistically significant strengthening of the stratospheric easterlies in summer has not yet been mentioned in past studies.

The strengthening of the polar vorticies induced by $4xCO_2$ in the simulations of the present study with prescribed ozone fields is systematically damped by the ozone changes (see chapter 4.2.2). This attenuation of the polar vorticies is probably responsible for the earlier final warming due to ozone changes (see Figure 4.6). However, the method for the final warming detection according Charlton and Polvani (2007) assumes that the polar vorticies are localized at 10 hPa and 60° N/S. In fact, the vorticies exist at different latitudes next to 60° N/S and pressure levels close to 10 hPa. Therefore, a method, which detects the polar vortex by searching the latitude of maximum zonal wind in the mid-latitude will localize the polar voritcies more precisely. However, during a final warming the zonal wind in the stratosphere of the mid-latitudes rapidly and prevalently switched from westerly to easterly. This leads to the conclusion that another diagnostic would not detect different final warming dates. Moreover, the method of Charlton and Polvani (2007) is often applied in recent studies like e.g. Kelleher et al. (2019) and in Rao and Garfinkel (2021) to find final warming dates.

The fact that ozone leads to a damping of the BDC acceleration is one of the key results of this study (see chapter 4.2.3). It has an effect on the transport of trace gases like ozone, CFCs and stratospheric water vapor, which impacts the thermal structure of the stratosphere (see chapter 4.1.3). According to DallaSanta et al. (2021), the damping is caused by the cooling of the tropical lower stratosphere through a decrease of ozone in this region, which results in combination with

a tropical upper tropospheric heating in an enhancement of the tropical upwelling through a CO_2 increase (see Figure 4.12). Nevertheless, it has to note that the temperature in the upper tropical troposphere in the $4xCO_2piO_3$-simulation is overestimated by the too high ozone concentrations. Therefore, the damping of the CO_2-induced enhancement of the tropical upwelling might be slightly affected by the too high ozone concentration in the upper troposphere.
Moreover, the study by Abalos et al. (2019) showed that the ozone depletion in the Antarctic stratosphere with accompanied cooling accelerates the BDC. That is in line with the damping of the BDC in case of an Antarctic stratospheric heating through a higher amount of ozone, which was shown in chapter 4.2.3.
Further, it has already found out that in a simulation with interactive coupled ocean and interactive ozone chemistry the CO_2-induced tropospheric heating is weakened (Dietmüller et al., 2014, Nowack et al., 2015 and Marsh et al., 2016). This in turn damps the acceleration of the BDC and would additionally enhance the ozone effect on the BDC if there are ozone changes due to $4xCO_2$.
In a future study the impact of the Antarctic ozone hole and of an interactive ocean on the BDC in the EMAC simulation can be investigated and compared with the study of Abalos et al. (2019). For this, transient EMAC simulations with interactive chemistry have to be analyzed. Such investigations can be for example done with the Chemistry-Climate Model Initiative (CCMI) Earth System Chemistry integrated Modelling (ESCiMo) simulations (Jöckel et al, 2016).

It was shown that ozone changes caused by $4xCO_2$ damp the CO_2-induced poleward shift of the southern hemispheric EDJ. Ceppi and Shepherd (2019) found out, that a delay in the vortex breakdown (final warming date) is linked to a stronger poleward jet shift. The ozone changes due to $4xCO_2$ leads to an earlier vortex breakdown. Therefore, the damping of the poleward EDJ shift is a result of the earlier final warming date due to ozone changes.
In addition to that, Byrne and Shepherd (2018) determine a relationship between the downward progression of the stratospheric anomalies from e.g. the zonal wind and the polar vortex strength in the SH. They state that a stronger polar vortex is connected to a later downward progression with a poleward EDJ shift and a weaker polar vortex is connected to an earlier downward progression with an equatorward EDJ shift. The ozone change through $4xCO_2$ systematically weakens the polar vortex (see Figures 4.5 c and d). Furthermore, there is a hint that the downward migration of zonal wind changes to the troposphere in the SH happens earlier (see Figure 4.16).

Moreover, Byrne and Shepherd (2018) also analyzed the EDJ strength in the SH, too. They compare the EDJ strength from days with two differently strong polar vorticies. The conclusion of this comparison was, that the EDJ strength differs the most in austral spring and summer. Moreover, in the recent study the difference of the EDJ strength between the two different ozone scenarios is biggest from August to December, which is from austral late winter until early

summer (see Figure 4.17 a). This covers the period in which Byrne and Shepherd (2018) assign the strongest difference of the EDJ strength.

The study from Ivanciu et al. (2021) investigates the effect of the ozone hole on e.g. the EDJ in the SH by applying a simulation with interactive ozone chemistry. They come to the conclusion that the ozone hole leads to an Antarctic lower stratospheric cooling especially in spring and summer, which results in a stronger polar vortex. Like in Byrne and Shepherd (2018), the enhanced polar vortex shifted the EDJ towards the pole. In the present study a prescribed ozone field was taken for the analysis.

Nevertheless, further investigation of the effects of interactive chemistry on the (stratospheric) dynamics as it was applied in Ivanciu et al. (2021) but for the NH can be done in future studies. For this purpose, the CCMI ESCiMo simulations (Jöckel et al., 2016) might be used. The results of such analysis will be helpful for the better understanding how the Arctic ozone depletion influences the tropospheric dynamics.

In summary, most of the dynamical changes in this study triggered by ozone changes are consistent with the results of the above described studies. Moreover, the fact that ozone changes damp the BDC acceleration, strengthen the stratospheric easterlies and lead to an earlier stratospheric final warming are the key results of the present study. These results have not been mentioned so far in other studies.

6 Summary and Conclusion

Figure 6.1 depicts an overview of the thermal and dynamical effects of CO_2-induced ozone changes. The thick arrows show the causal connections between these effects, where the minus/plus signs stand for a weakening/strengthening of the pointed processes. The thin arrows represent possible connections between the processes, which are not investigated further in the present study. Figure 6.1 can be regarded as a schematic summary of the results of this thesis. Additionally, a briefly written summary that answers the science questions from the introduction is provided.

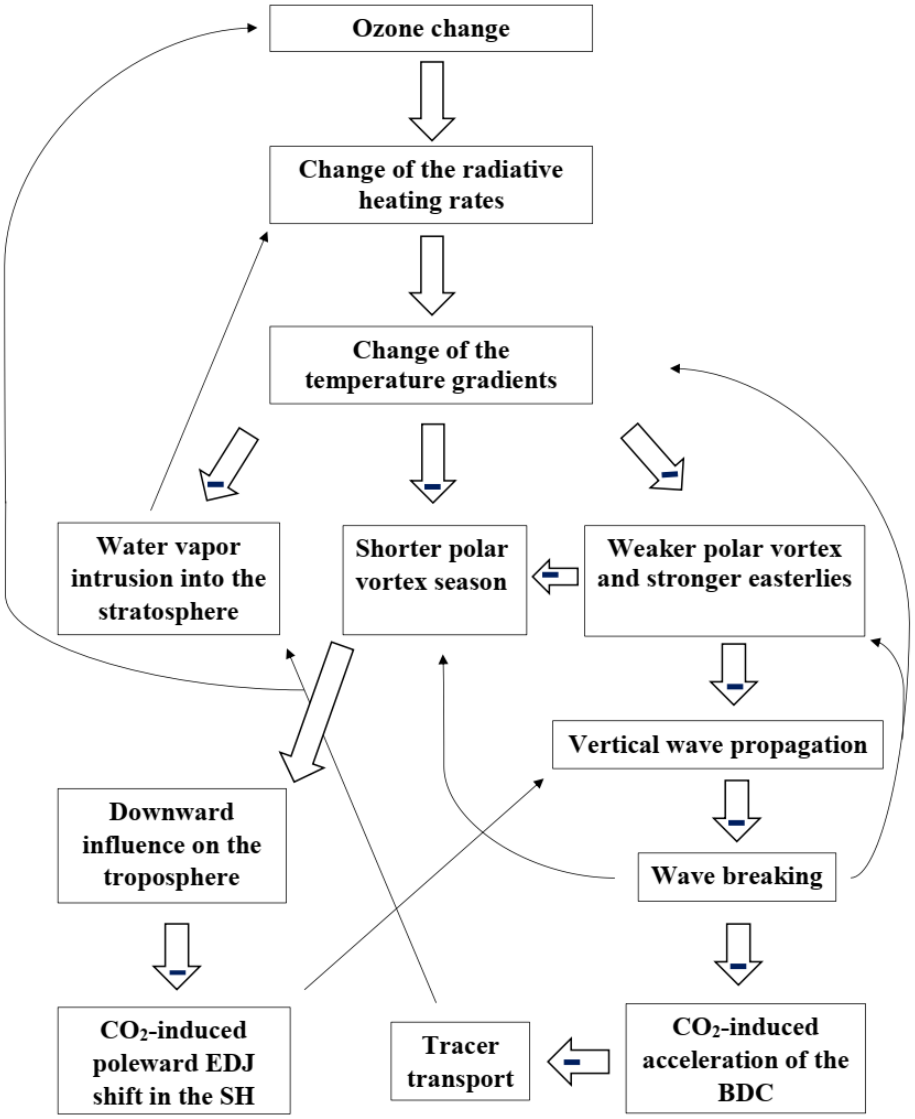

Figure 6.1: Schematic overview of the thermal and dynamical responses on CO_2-induced ozone changes and the links between them. The minus/plus sign stand for a weakening/strengthening of the processes, which are pointed at by the thick arrows. Thin arrows represent possible connections between the processes that are not investigated in this study.

First of all, the direct thermal effects through CO_2-induced ozone changes, which are shown in the present study are addressed by regarding Figure 6.1. These lead to the science questions which are asked and answered.

Changes in the ozone field through $4xCO_2$ modify the absorption/emission of longwave and shortwave radiation. This modification cools the tropical lower stratosphere as well as the tropical tropopause region and warms the other areas of the summer and tropical stratosphere, which leads to two effects. On the one side, less water vapor from the troposphere enters the stratosphere, which results in a drier stratosphere. Less stratospheric water vapor influences the radiative heating through longwave radiation. However, this response is not investigated in detail in this work. On the other side, the enhancement of the meridional temperature gradient in the lower stratosphere is connected with an acceleration of the stratospheric extra-tropical zonal winds by thermal wind balance. The result is a significant enhancement of the stratospheric easterlies and a systematic attenuation of the polar vortices. This leads to the first question:

- *How do the polar vorticies change due to $4xCO_2$-induced ozone changes?*

The changes in the ozone field cause a more abrupt final warming and shorten the period of the polar vortices. This shortening is a result of a later vortex buildup and an earlier vortex breakdown. These ozone effects on the polar vorticies and on the stratospheric easterlies have not been analyzed before in other studies.

Weaker polar vortices or stronger stratospheric easterlies impact the vertical wind shear, which is an important parameter for vertical wave propagation. This fact raises the next question:

- *Which impact do $4xCO_2$-induced ozone changes have on the wave properties?*

The upward Eliassen-Palm (EP) flux decreases in the summer lower stratosphere due to ozone changes which increases the EP flux divergence (EPFD) in the middle stratosphere. This indicates weaker wave breaking at the upper flank of the subtropical jet (STJ) and hence a weakening of the wave-mean-flow interaction, which induces an attenuation of the residual downward flow there. As the residual circulation in the stratosphere is a part of the Brewer-Dobson circulation (BDC), that brings up the following question:

- *How do $4xCO_2$-induced ozone changes affect the BDC and the stratospheric transport?*

The weaker upward EP flux with the increased EPFD in the summer middle stratosphere causes a significant damping of the CO_2-induced acceleration of the residual circulation in this season and region. This change in the residual circulation in turn modifies the tracer transport in the stratosphere (e.g. water vapor intrusion). The damping of the residual circulation due to ozone changes has not been mentioned in past studies. Moreover, the mean age of air (AoA) increases due to CO_2-induced ozone changes which is linked to the weakening of the BDC. Here, the AoA

increase is even significant in the whole stratosphere indicating at least a systematic attenuation of the acceleration of all BDC branches.

Ozone changes through 4xCO_2 mitigate the persistence of the polar vortices, which can be seen by a later vortex buildup and an earlier vortex breakdown (final warming). This leads to the answer of this question:

- *How does the tropospheric dynamics react on the 4xCO_2-induced ozone changes?*

In the troposphere the CO_2-induced poleward shift of the austral Eddy driven jet (EDJ) is systematically weakened by the earlier vortex breakdown. This is in line with the past studies that connected a later/earlier vortex breakdown with a poleward/equatorward shift of the EDJ. Moreover, the analysis of the downward coupling shows conclusive connections between the earlier vortex breakdown and the damping of EDJ poleward shift.

Figure 6.2 depicts a schematic latitude-height cross-section of the resulting thermal and dynamical effects on the troposphere and stratosphere due to ozone changes for northern winter. In this sketch blue/red shading indicates cooling/warming and blue/red arrows or words represent weakening/strengthening of the respective effect.

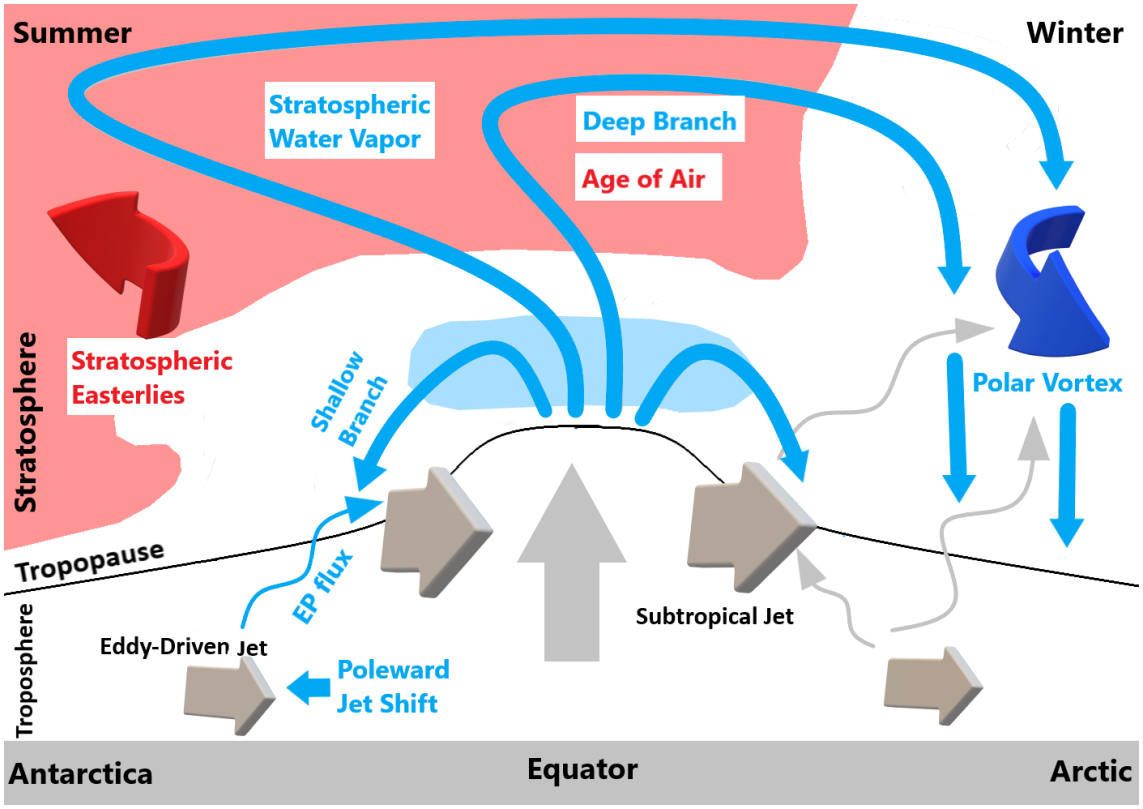

Figure 6.2: Latitude-height cross-section of the resulting thermal and dynamical effects on the troposphere and stratosphere due to ozone changes for northern winter. Blue/red shading indicates cooling/warming. Blue/red arrows represent weakening/strengthening of the respective effect. The grey arrows are streamers whose strength is not directly affected by CO_2-induced ozone changes.

With the help of Figure 6.2 the resulting impact on the temperature and dynamics will be shortly summarized. The CO_2-induced ozone changes on the one side warm the extra-tropical summer stratosphere and the tropical upper stratosphere. On the other side, the ozone changes cool the lower tropical stratosphere. These thermal responses are connected to the dynamics, which can be seen in a statistically significant strengthening of the stratospheric easterlies and a systematic weakening of the polar vortex that is accompanied with a shorter polar vortex period. Moreover, the EP flux as well as the wave forcing are attenuated in summer. This leads to a systematic damping of the CO_2-induced acceleration of the residual flow in the stratosphere which causes the higher AoA. The AoA increase is even significant in the whole stratosphere. Furthermore, the ozone changes weaken the CO_2-induced poleward shift of the EDJ in the SH and decrease the amount of stratospheric water vapor.

These results underline the importance of ozone with respect to dynamics in a world where the CO_2 concentrations increase. Moreover, the recent study even generates new findings in terms of ozone effects in a changing climate. These new findings clarify that it is important to understand the impacts of ozone, otherwise the attribution of effects in climate change simulations may be erroneous. However, it has to note that the impact of the CO_2 increase is not reversed by taking the thermal and dynamical ozone changes into account. Ozone changes lead only to a systematic and partially to even a significant damping of the CO_2 effect itself. Nevertheless, a realistic representation of ozone distribution in climate models would have an essentially quantitative effect on the temperatures and dynamics. This fact can possibly modify the socio-economic dealing with the future challenges in the climate change.

Bibliography

Abalos, M., Polvani, L., Calvo, N., Kinnison, D., Ploeger, F., Randel, W., and Solomon, S.: New insights on the impact of ozone-depleting substances on the Brewer-Dobson circulation. Journal of Geophysical Research: Atmospheres, Vol. 124, 2435–2451. https://doi.org/10.1029/2018JD029301, 2019.

Austin, J., und F. Li, On the relationship between the strength of the Brewer-Dobson circulation and the age of stratospheric air, Geophys. Res. Lett., Vol. 33, L17807. https://doi.org/10.1029/2006GL026867, 2006.

Ayarzagüena, B., Charlton-Perez, A. J.,Butler, A. H., Hitchcock, P., Simpson, I.R., Polvani, L. M., et al.: Uncertainty in the response of sudden stratospheric warmings and stratosphere-troposphere coupling to quadrupled CO_2 concentrations in CMIP6 models. Journal of Geophysical Research: Atmospheres, 125. https://doi.org/10.1029/2019JD032345, 2020.

Baldwin, M. P., Ayarzagüena, B., Birner, T., Butchart, N., Butler, A. H., Charlton-Perez, A. J.: Sudden stratospheric warmings. Reviews of Geophysics, Vol. 59. https://doi.org/10.1029/2020RG000708, 2021.

Birner, T. and H. Bönisch: Residual circulation trajectories and transit times into the extratropical lowermost stratosphere. Atmospheric Chemistry and Physics, Vol. 11(2): 817 – 827. https://doi.org/doi: 10.5194/acp-11-817-2011, 2011.

Bönisch, H., A. Engel, T. Birner, P. Hoor, D. W. Tarascik and E. A. Ray: On the structural changes in the Brewer-Dobson circulation after 2000. Atmospheric Chemistry and Physics, https://doi.org/10.5194/acp-11-3937-2011, 2011.

Brewer, A. W.: Evidence for a world circulation provided by measurements of helium and water vapor distribution in the stratosphere. Q.J.R. Meteorol. Soc. Vol. 11(8), 75-35, https://doi.org/10.1002/qj.49707532603, 1949.

Byrne, N. J., T. G. Shepherd. Seasonal Persistence of Circulation Anomalies in the Southern Hemisphere Stratosphere and Its Implications for the Troposphere. Journal of Climate, Vol. 31, 3467 – 3783, https://doi.org/10.1175/JCLI-D-17-0557.1, 2018.

Ceppi, P., & Shepherd, T. G. The role of the stratospheric polar vortex for the austral jet response to greenhouse gas forcing. Geophysical Research Letters, Vol. 46, 6972–6979, https://doi.org/10.1029/2019GL082883, 2019.

Charlton, A. J., and L. M. Polvani: A new look at stratospheric sudden warmings. Part I: Climatology and modeling benchmarks. J. Climate, Vol. 20**,** 449–469, https://doi.org/10.1175/JCLI3996.1, 2007.

Chiodo, G., and L. M. Polvani (2016): Reduced Southern Hemispheric circulation response to quadrupled CO_2 due to stratospheric ozone feedback, Geophys. Res. Lett., Vol. 43, https://doi.org/10.1002/2016GL071011, 2017.

Chiodo, G., L. M., Polvani: The Response of the Ozon Layer to Quadrupled CO_2 Concentrations: Implications for Climate. American Meteorological Society, Vol. 32(22). https://doi.org/10.1175/JCLI-D-19-0086.1, 2019.

DallaSanta, K., Orbe, C., Rind, D., Nazarenko, L., and Jonas, J.: Dynamical and trace gas responses of the quasi-biennial oscillation to increased CO2. Journal of Geophysical Research: Atmospheres, Vol. 126, e2020JD034151. https://doi.org/10.1029/2020JD034151, 2021.

Dietmüller, S., M. Ponater, and R. Sausen: Interactive ozone induces a negative feedback in CO2-driven climate change simulations, J. Geophys. Res. Atmos., Vol. 119, 1796–1805, https://doi.org/10.1002/2013JD020575, 2014.

Dietmüller, S., Jöckel, P., Tost, H., Kunze, M., Gellhorn, C., Brinkop, S., Frömming, C., Ponater, M., Steil, B., and Hendricks, J.: A new radiation infrastructure for the Modular Earth Submodel System (MESSy, based on version 2.51), Geoscientific Model Development, Vol. 9, 2209–2222, https://doi.org/10.5194/gmd-9-2209-2016, 2016.

Dietmüller, S., Eichinger, R., Garny, H., Birner, T., Boenisch, H., Pitari, G., Mancini, E., Visioni, D., Stenke, A., Revell, L., Rozanov, E., Plummer, D. A., Scinocca, J., Jöckel, P., Oman, L., Deushi, M., Kiyotaka, S., Kinnison, D. E., Garcia, R., Morgenstern, O., Zeng, G., Stone, K. A., and Schofield, R.: Quantifying the effect of mixing on the mean age of air in CCMVal-2 and CCMI-1 models, Atmos. Chem. Phys., Vol. 18, 6699–6720, https://doi.org/10.5194/acp-18-6699-2018, 2018.

Dobson, G. M. B.: Origin and distribution of the polyatomic molecules in the atmosphere. Proc. R. Soc., Vol. 236, 87–193, https://doi.org/10.1098/rspa.1956.0127, 1956.

Edmon JR., H.J., B.J. Hoskins and M. E. McIntyre.: Eliassen-Palm cross chapters for the troposphere. Journal of the Atmospheric Sciences, Vol. 37, 2600 – 2615, 1981.

Eichinger R., S. Dietmüller, H. Garny, P. Šácha, T. Birner, H. Bönisch, G. Pitari, D. Visioni, A. Stenke, E. Rozanov, L. Revell, D. A. Plummer, P. Jöckel, L. Oman, M. Deushi, D. E. Kinnison,

R. Garcia, O. Morgenstern, G. Zeng, K.A. Stone, and R. Schofield: The influence of mixing on the stratospheric age of air changes in the 21st century. Atmos. Chem. Phys., Vol. 17, 11177–11192, https://doi.org/10.5194/acp-17-11177-2017, 2017:

Eichinger, R. and P. Šácha: Overestimated acceleration of the advective Brewer-Dobon circulation due to stratospheric cooling. Quarterly Journal of the Royal Meteorological Society, Vol. 146, Issue 733. 2850 – 3864, https://doi.org/10.1002/qj.3876, 2020.

Eyring V., Arblaster J.M., Cionni I., Perlwitz J., Young P.J., Bekki S., et al.: Long-term ozone changes and associated climate impacts in CMIP5 simulations. J Geophys Res Atmos.; 118:5029–60, https://doi.org/10.1002/jgrd.50316, 2013.

Fritts, D. C. and M. J. Alexander: Gravity Waves Dynamics and their Effects on the Middle. Atmosphere. Rev. Geophys., Vol. 41, 1003, https://doi.org/10.1029/2001RG000106, 2003.

Fueglistaler, S., M. Bonazzola, P.H. Haynes, und T. Peter, Stratospheric water vapor predicted from the Lagrangian temperature history of air entering the stratosphere in the tropics. J. Geophys. Res., Vol. 110, D08107, https://doi.org/10.1029/2004JD005516, 2005.

Fomichev, V.I., A.I. Jonsson, J. de Grandpré, S.R. Beagley, C. McLandress, K. Semeniuk, und T.G. Shepherd, Response of the middle atmosphere to CO_2 doubling: Results from the Canadian Middle Atmosphere Model, J. Clim., Vol. 20, 1121–1144, 2007.

Garcia, R. R., W. J. Randel: Acceleration of the Brewer-Dobson Circulation due to Increases in Greenhouse Gases. Journal of the Atmospheric Sciences, Vol. 65(8), 2731-2739, https://doi.org/10.1175/2008JAS2712.1, 2008.

Garfinkel C., Son S-W, Song K, Aquila V, Oman LD. Stratospheric variability contributed to and sustained the recent hiatus in Eurasian winter warming. Geophys Res Lett.; 44:374–82. https://doi.org/10.1002/2016GL072035, 2017.

Garny, H., T. Birner, H. Bönisch and F. Bunzel: The effects ofmixing on age of air, J. Geophys.Res. Atmos, Vol. 119, 7015–7034, doi: https://doi.org/10.1002/2013JD021417, 2014.

Häckel, H.: Meteorologie; 9. Auflage. Verlag Eugen Ulmer Stuttgart, 2021.

Hall, T. M. and R. A. Plumb. Age as a diagnostic of stratospheric transport. *J*. Geophys. Res., Vol. 99, 1059–1070. doi: https://doi.org/10.1029/93JD03192, 1994.

Hardiman, S. C., M. B. Andrews, T. Andrews, A. C. Bushell, N.J. Dunstone, H. Dyson, et al. The impact of prescribed ozone in climate projections run with HadGEM3-GC3.1. Journal of

Advances in Modeling Earth Systems, Vol. 11, 3443–3453. https://doi.org/10.1029/2019MS001714, 2019.

Haynes, P. H., C. J. Marks, M. E. McIntyre, T. G. Shepherd and K. P. Shine: On the 'Downward Control' of Extratropical Diabatic Circulations by Eddy-Induced Mean Zonal Forces, J. Atmos. Sci., Vol. 48., S. 651, 1991.

Holton, J. R. and G. J. Hakim: An Introduction to Dynamic Meteorology; Fifth Edidtion. Elsevier Academic Press, 2013.

Ivanciu, I., K. Matthes, S. Wahl, J. Harlaß and A. Biastoch: Effects of prescribed CMIP 6 ozone on simulating the Southern Hemisphere atmospheric circulation response to ozone depletion. Atmospheric Chemistry and Physics, Vol. 21, 5777-5806, https://doi.org/10.5194/acp-21-5777-2021, 2021

Jöckel, P., Sander, R., Kerkweg, A., Tost, H., and Lelieveld, J.: Technical Note: The Modular Earth Submodel System (MESSy) - a new approach towards Earth System Modelling, Atmospheric Chemistry and Physics, Vol. 5, 433–444, https://doi.org/10.5194/acp-5-433-2005, 2005.

Jöckel, P., Kerkweg, A., Pozzer, A., Sander, R., Tost, H., Riede, H., Baumgaertner, A., Gromov, S., and Kern, B.: Development cycle 2 of the Modular Earth Submodel System (MESSy2), Geoscientific Model Development, Vol. 3, 717–752, https://doi.org/10.5194/gmd-3-717-2010, 2010.

Jöckel, P., Holger, T. O., Pozzer, A., Kunze, M., Kirner, O., Brenninkmeijer, C., Brinkop, S., Cai, D., Dyroff, C., Eckstein, J., Frank, F., Garny, H., Gottschaldt, K.-D., Graf, P., Grewe, V., Kerkweg, A., Kern, B., Matthes, S., Mertens, M., Meul, S., Neumaier, M., Nützel, M., Oberländer-Hayn, S., Ruhnke, R., Runde, T., Sander, R., Scharffe, D., and Zahn, A.: Earth System Chemistry Integrated Modelling (ESCiMO) with the Modular Earth Submodel System (MESSy, version 2.51), Geoscientific Model Development, Vol. 9, 1153–1200, https://doi.org/10.5194/gmd-9-1153-2016, 2016.

Jonsson, A.I., J. de Grandpré, V.I. Fomichev, J.C. McConnell, und S.R. Beagley: Doubled CO2 -induced cooling in the middle atmosphere: Photochemical analysis of the ozone radiative feedback, J. Geophys. Res., Vol. 109, D24103, doi:10.1029/2004JD005093, 2004

Kelleher, M. E., B. Ayarzagüena and J. A. Screen: Interseasonal Connections between the Timing of the Stratospheric Final Warming and Arctic Sea Ice. Journal of Climate, Vol. 33, 3079 - 3092, https://doi.org/10.1175/JCLI-D-19-0064.1, 2019.

Kida, H.: General circulation of air parcels and transport characteristics derived from a hemispheric gcm. Journal of the Meteorological Society of Japan. Ser. II, Vol. 61(2): 171–187. https://doi.org/doi: 10.2151/jmsj1965.61.2 171, 1983.

Kim B.-M., Son S.-W., Min S.-K., Jeong J.-H., Kim S.-J., Zhang X., et al.: Weakening of the stratospheric polar vortex by Arctic Sea-ice loss. Nat Commun.; 5:4646. https://doi.org/10.1038/ncomms5646, 2014.

Kraus, H.: Die Atmosphäre der Erde: Eine Einführung in die Meteorologie; 3. Erweiterte Auflage, Springer Verlag, 42, 2004.

Kretschmer M., Coumou D, Agel L, Barlow M, Tziperman E, Cohen J.: More-persistent weak stratospheric polar vortex states linked to cold extremes. Bull Am Meteorol Soc.; 99:49–60. https://doi.org/10.1175/BAMS-D-16-0259.1, 2018.

Labitzke, K. G.: Die Stratosphäre: Phänomene, Geschichte, Relevanz. Springer-Verlag, Berlin, 1998.

Li, F., J. Austin and J. Wilson: The Strength of the Brewer–Dobson Circulation in a Changing Climate: Coupled Chemistry–Climate Model Simulations. Journal of Climate, Vol. 21, 40 – 57, https://doi.org/10.1175/2007JCLI1663.1, 2007.

Matthewman, N. J., J. G. Esler, A. J. Charlton-Perez, and L. M. Polvani, A new look at stratospheric sudden warmings. Part III: Polar vortex evolution and vertical structure, J. Climate, Vol. 22, 1566–1585, https://doi.org/10.1175/2008JCLI2365.1, 2009.

Marsh, D. R., J.-F. Lamarque, A. J. Conley, and L. M. Polvani, Stratospheric ozone chemistry feedbacks are not critical for the determination of climate sensitivity in CESM1(WACCM), Geophys. Res. Lett., 43, 3928–3934, https://doi.org/10.1002/2016GL068344, 2016.

Marshall G.J.: Trends in the southern annular mode from observations and reanalyses. J Clim.;16:4134–43. https://doi.org/10.1175/1520-0442(2003)016<4134:TITSAM>2.0.CO;2, 2003.

Marshall, J., and K. Speer: Closure of the Meridional Overturning Circulation through Southern Ocean upwelling, Nat. Geosci., Vol. 5(3), 171–180, 2012.

McLandress, C and T. G. Shepherd: Simulated Anthropogenic Changes in the Brewer–Dobson Circulation, Including Its Extension to High Latitudes; Journal of Climate; American Meteorological Society, Vol. 22(6). https://doi.org/10.1175/2008JCLI2679.1, 2009.

Nissen, K. M., Matthes, K., Langematz, U., and Mayer, B.: Towards a better representation of the solar cycle in general circulation models, 20 Atmospheric Chemistry and Physics, Vol. 7, 5391–5400. https://doi.org/10.5194/acp-7-5391-2007, 2007.

Nowack, P., N. Luke Abraham, A. C. Maycock, P. Braesicke, J. M. Gregory, M. M. Joshi, A. Osprey and J. A. Pyle,. A large ozone-circulation feedback and its implications for global warming assessments. Nature Clim Change, Vol. 5, 41–45, https://doi.org/10.1038/nclimate2451, 2015.

Nowack, P. J., N. Abraham, P. Braesicke and J. A. Pyle: The impact of stratospheric ozone feedbacks on climate sensitivity estimates. Journal of Geophysical Research: Atmospheres, Vol. 123,4630–4641, https://doi.org/ 10.1002/2017JD027943, 2018.

Okamoto, K., K. Sato and H. Akiyoshi: A study on the formation and trend of the Brewer-Dobson circulation. J. Geophys. Res. Vol. 116 S. D10117, https://doi.org/.1029/2010JD014953, 2011.

Plumb, R. A.: Stratospheric Transport. Journal of the Meteorological Society of Japan, Vol. 80, No. 4B, pp. 793-809, 2002.

Roa, J. and C. I. Garfinkel: Projected changes of stratospheric fnal warmings in the Northern and Southern Hemispheres by CMIP5/6 models. Climate Dynamics, Vol. 56, 3353 – 3371, https://doi.org/10.1007/s00382-021-05647-6, 2021.

Sander, R., Jöckel, P., Kirner, O., Kunert, A. T., Landgraf, J., and Pozzer, A.: The photolysis module JVAL-14, compatible with the MESSy standard, and the JVal PreProcessor (JVPP), Geoscientific Model Development, Vol. 7, 2653–2662, https://doi.org/10.5194/gmd-7-2653-2014, 2014.

Screen, J.A., T.J. Bracegirdle and I. Simmonds: Polar Climate as Manifest in Atmospheric Circulation, Climate Change and Atmospheric Circulation, Current Climate Change Report, 4: 383-395. https://doi.org/10.1007/s40641-018-0111-4, 2018.

Seinfeld, J.H. and S.N. Pandis: Atmospheric Chemistry and Physics: From Air Pollution to Climate Change, Vol. 2., John Wiley and Sons, 2006.

Seviour, W. J. M., D. M. Mitchel and G. J. Gray: A practical method to identify displaced and split stratospheric polar vortex events, Geophysical Research Letters, Vol. 40, 5268–5273, https://doi.org/10.1002/grl.50927, 2013.

Seviour W.J.M.: Weakening and shift of the Arctic stratospheric polar vortex: internal variability or forced response? Geophys Res Lett. ;44:3365–73. https://doi.org/10.1002/2017GL073071, 2017.

Shaw, T. A.: Mechanisms of Future Predicted Changes in the Zonal Mean Mid-Latitude Circulation. Current Climate Change Reports, Vol. 5, 345-357, https://doi.org/10.1007/s40641-019-00145-8, 2019.

Shepherd, G. S. and C. McLandress: A Robust Mechanism for Strengthening of the Brewer–Dobson Circulation in Response to Climate Change: Critical-Layer Control of Subtropical Wave Breaking, Vol. 68(4), 784 – 797, https://doi.org/10.1175/2010JAS3608.1, 2011.

Sigmond, M., P.C. Siegmund, E. Manzini, und H. Kelder, A simulation of the separate climate effects of middle-atmospheric and tropospheric CO_2 doubling, J. Clim., Vol. 17(12), 2352-2367, 2004.

Son S.-W., Han B.-R., Garfinkel C.I., Kim S.-Y., Park R., Abraham N.L., et al.: Tropospheric jet response to Antarctic ozone depletion: an update with chemistry-climate model initiative (CCMI) models. Environ Res Lett.; 13:5. https://doi.org/10.1088/1748-9326/aabf21, 2018.

Stenke, A., and V. Grewe: Simulation of stratospheric water vapor trends: impact on stratospheric ozone chemistry. Atmos. Chem. Phys., Vol. 5, 1257–1272, https://doi.org/10.5194/acp-5-1257-2005, 2005.

Stiller, G. P., F. Fierli,, F. Ploeger, C. Cagnazzo, B. Funke, F.J Haenel, T. Reddmann, M. Riese, and T. von Clarmann: Shift of subtropical transport barriers explains observed hemispheric asymmetry of decadal trends of age of air, Atmos. Chem. Phys., Vol. 17, 11177–11192, https://doi.org/10.5194/acp-17-11177-2017, 2017.

Thompson DWJ, Solomon S. Interpretation of recent southern hemisphere climate change. Science; 296:895–9. https://doi.org/10.1126/science.1069270, 2002.

Vallis, G. K.: Atmospheric and Oceanic Fluid Dynamics. Fundamentals and Larrge-scale Circulation. Second Edition. Cambridge University Press, 2017.

Waugh, D. and T. Hall. Age of stratospheric air: Theory, observations, and models. Reviews of Geophysics, Vol. 40(4), 1–26. https://doi.org/doi: 10.1029/2000RG000101, 2002.

Wu, H.W., A. Emadi, G. de Graaf, J. Leijtens and R.F. Wolffenbuttel: Design and fabrication of an albedo insensitive analog sun sensor. Elsevier Academic Press, Vol. 25, 527 – 530. https://doi.org/doi:10.1016/j.proeng.2011.12.131, 2011.

Wu, Y., Simpson, I. R., & Seager, R.: Intermodel spread in the Northern Hemisphere stratospheric polar vortex response to climate change in the CMIP5 models. Geophysical Research Letters,46,13,290–13,298. https://doi.org/10.1029/2019GL085545, 2019.

Acknowledgement

Very special thanks go to my supervisors Dr. Roland Eichinger and Prof. Dr. Hella Garny, who offered me this topic, always gave me tips and suggestions for my analyses and also helped me with the evaluation of the results. I would especially like to thank Dr. Roland Eichinger for reading the individual chapters of the master's thesis and for providing the model data.

A far-reaching thank you also go to Prof. Dr. Thomas Birner and his working group, who often gave me important suggestions for improving and evaluating my analyses.

Thanks also go to Roland Walz and Dr. Ales Kuchar who helped to solve some programming problems and with the evaluation of the results.

I would also like to thank the Institute of Atmospheric Physics of the DLR in Oberpfaffenhofen, especially the Earth System Modeling Department, for making it possible to do this work in this particular pandemic situation, as well as for the collegial support and the entertaining coffee rounds.

Special thanks go also to the "EMAC-Round" and the "Python-Round" where I got important help to technical problems and where interesting applications for programming were shown.

An immeasurable thanks go to my parents, who motivated me at all to complete the master and supported me mentally.

I would also like to thank my friends, who showed me that there is also a life outside of the scientific world.

The biggest thanks go to my girlfriend Sophia.

Erklärung zur Abschlussarbeit

Hiermit erkläre ich, die vorliegende Arbeit selbständig verfasst zu haben und keine anderen als die in der Arbeit angegebenen Quellen und Hilfsmittel benutzt zu haben.

München, den 03.03.2022

…….

(Leonhard Hufnagl)